UNIVERSITY
OF TURKU

TESTING OF MANUFACTURABILITY AND CHARACTERIZATION OF BIMETALLIC MATERIAL OF INCONEL 718 AND CUCRZR FABRICATED BY LASER-BASED POWDER BED FUSION

Materials Engineering/Faculty of Technology
Master's thesis
Department of Mechanical and Materials Engineering

Author:
Janne Hirvonen

28.10.2025
Turku

Master's thesis

Subject: Materials engineering
Author: Janne Hirvonen
Title: Testing of manufacturability and characterization of bimetallic material of Inconel 718 and CuCrZr fabricated by laser-based powder bed fusion
Supervisor: Professor Antti Salminen, D.Sc.(Tech.); Associate professor Ashish Ganvir, PhD
Advisor: Senior researcher Heidi Piili, D.Sc.(Tech.); Postdoctoral researcher Nikhil Kamboj, D.Sc.(Tech.); Assistant professor Mohsen Amraei, PhD
Number of pages: 112 pages
Date: 28.10.2025

Laser-based powder bed fusion of metals (PBF-LB/M) is an additive manufacturing technique in which metal powder is fused layer-by-layer to form three-dimensional components. PBF-LB/M has been established as a manufacturing method for producing complex components otherwise non-viable or impossible to manufacture. The interest in multi-material PBF-LB/M, which allows for combining desired properties of two or more metal materials in one component, has increased as the technology has developed.

This thesis explores the manufacturing of a bimetallic material combination of Inconel 718 (IN718) and copper-chromium-zirconium alloy (CuCrZr) using PBF-LB/M to find optimised process parameters supported by different material characterisation and testing methods. In addition, the effects of heat treatment on the properties of the manufactured material are studied. The process of manufacturing the bimetallic material combination of IN718 and CuCrZr lacks research, and this thesis aims to successfully manufacture a defect free bimetallic material.

The results obtained in this thesis showed promise for manufacturing of defect-free bimetallic material of IN718 and CuCrZr. Bimetallic material was successfully manufactured, and the quality of the material was tested and analysed. The compatibility of IN718 and CuCrZr was proven as the materials exhibited mixing at the interface zone allowing for bonding between the two materials. However, some defects were observed in the materials which require further studies and optimisation of the manufacturing process and post-processing steps. The effects of additional optimisation of the manufacturing process parameters on the number of defects found in the material should be studied. In addition, the heat-treatment process should be further developed to match the requirements of the bimetallic material combination.

Key words: additive manufacturing, laser-based powder bed fusion of metals, Inconel 718, CuCrZr, bimetallic, manufacturability, material properties

Table of contents

Nomenclature

Abbreviation	Explanation
AM	additive manufacturing
AMed	additively manufactured
CAD	computer-aided design
COF	coefficient of friction
CuCrZr	copper-chromium-zirconium alloy
EDS	energy-dispersive X-ray spectroscopy
IN718	nickel-based superalloy Inconel 718
LED	linear energy density
OCP	open circuit potential
PBF	powder bed fusion
PBF-LB	laser-based powder bed fusion
PBF-LB/M	laser-based powder bed fusion of metals
PBF-LB/Med	manufactured via laser-based powder bed fusion of metals
SEM	scanning electron microscope
VED	volumetric energy density

Symbol	Unit	Explanation
A	mm^2	cross-sectional area
d	mm	depth
D	mm	distance

E_{corr}	mV	corrosion potential
h	mm	hatch distance
I_{corr}	μA/cm^3	corrosion current density
l	mm	length
L	Ω·WK^{-2}	Lorenz number
P	W	laser power
R	Ω	electrical resistance
t	mm	layer thickness
T	K	temperature
v	mm/s	scanning speed of laser beam
w	mm	width
γ	-	gamma phase
γ'	-	gamma prime phase
γ''	-	gamma double prime phase
δ	-	delta phase
λ	W·mK	thermal conductivity
ρ	Ω·m	electrical resistivity
σ	S/m	electrical conductivity

1 Introduction

Powder bed fusion (PBF) is an additive manufacturing (AM) technique in which a thermal energy source is used to melt and fuse layers of feedstock material powder, layer-by-layer, to form a three-dimensional component. PBF can be further categorized by the used thermal energy source, e.g. laser or electron beam, and used feedstock material, e.g. metals or polymers. (Pei et al., 2023) In this thesis, only laser-based powder bed fusion of metals (PBF-LB/M) will be considered.

Laser-based powder bed fusion (PBF-LB) was originally developed in the 1980s. Introduction for commercial use took place in the 1990s and the technology has developed into a viable method for producing additively manufactured (AMed) components. (Yadroitsev et al., 2021) Nevertheless, laser-based powder bed fusion is to this day a rapidly developing field of technology. PBF-LB/M is one of the most used metal AM technologies and can produce high quality components with higher dimensional accuracy and surface quality compared to other AM techniques. In addition, AM allows for complex designs to be realized, that are non-viable or impossible to manufacture by traditional means. (Zhang et al., 2024) Component design is made with computer aided design (CAD) software. (Pei et al., 2023)

In multi-material additive manufacturing, two or more feedstock materials are used to manufacture a component with alternating material regions. The used materials in multi-material metal AM can be both pure metals and alloys. This allows for fine tuning of the properties in the finished components with desired properties including thermal conductivity, toughness, hardness, and resistance to wear and corrosion etc. at specific regions in the component structures. (Mao et al., 2023)

One challenge in multi-material additive manufacturing is the compatibility of the combined materials and the properties of the materials must be taken into consideration. (Nazir et al., 2023) Inconel 718 (IN718) and copper-chromium-zirconium (CuCrZr) share a face-centred-cubic crystal structure which aids with compatibility of the materials in multi-material AM. The crystal structure of the materials allows the materials to mix and form a transitioning interface zone between the distinct material regions. (Zhang et al., 2024)

IN718 (Volpato et al., 2022) and CuCrZr (Cortis et al., 2023) are known materials in PBF-LB/M, but the bimetallic material combination of the two lacks research. IN718 is known for mechanical properties including high fatigue and wear resistances. (Zhang et al., 2024) CuCrZr is known for properties including high electrical and thermal conductivities. (Salvan et al., 2021) This combination makes the bimetallic material a viable candidate for applications where both durability and specific thermal properties are required, for example in heat exchangers.

However, the PBF-LB/M processes for both materials are different due to the dissimilarities in material properties. The low thermal conductivity of IN718 leads to a lower thermal energy requirement to melt and fuse the powder feedstock layers during the PBF-LB/M process compared to CuCrZr. (Hakeem et al., 2021; Zhang et al., 2024) This leads to challenges especially in the manufacturing of the interface zone between the two materials. (Meyer et al., 2025) In addition, the post processing, such as heat treatment steps, of the two materials are different and a compromise between the two must be made. (Naskar et al., 2024a; Wallis & Buchmayr, 2019)

The aim of this thesis is to manufacture a bimetallic material consisting of IN718 and CuCrZr, and to study the manufacturing process and effects of heat treatment on the properties of the manufactured material. Optimised parameters for manufacturing the bimetallic material and the effects of heat treatment on the individual materials and the interface zone are studied. The manufactured material combination is analysed for material quality and different characteristics are determined.

Based on the results, challenges and requirements for future studies will be identified.

2 Materials

The materials covered in this thesis are nickel-based superalloy Inconel 718 and copper-based alloy CuCrZr.

2.1 Inconel 718

Inconel 718 (IN718) is a widely used nickel-based superalloy with properties to endure use even in high-temperature applications. These properties include e.g. high yield and tensile strengths, resistance to creep and fatigue, and resistance to oxidation. (Zhang et al., 2024) IN718 has a wide range of applications in different fields, including power production and aerospace components. (Zhang et al., 2024; Zhong et al., 2023)

Alloying elements used IN718 can have variations. The most common alloying elements in IN718 are nickel (Ni), chromium (Cr), iron (Fe), niobium (Nb), molybdenum (Mo), titanium (Ti), cobalt (Co), and aluminium (Al). (Hosseini & Popovich, 2019) Other alloying elements may include for example carbon (C), magnesium (Mg), silicon (Si). Different elements have an effect on the properties of the alloy. (Deng, 2018) Weight percentages of the main alloying elements are shown in Table 1.

Table 1 Main alloying element composition of IN718.
[1](Deng, 2018), [2](Hosseini & Popovich, 2019)

Element	Wt.%
Ni	50.00 – 55.00[1, 2]
Cr	17.00 – 21.00[1, 2]
Fe	Balance[1, 2]
Nb	4.75 – 5.50[1], 4.80 – 5.50[2]
Mo	2.80 – 3.30[1], 2.80 – 3.00[2]
Ti	0.65 – 1.15[1, 2]
Al	0.20 – 0.80[1, 2]
Co	max. 1.00[1], 1.00[2]

As Table 1 shows, IN718 consists mainly of nickel, chromium and iron, with additions of other elements. The alloy is balanced with iron.

IN718 components are traditionally manufactured mostly with forging and casting methods. These traditional manufacturing methods have their limitations and cannot necessarily provide adequate component design for modern applications. In addition, complex forged component designs can exhibit degraded material properties caused by changes on the microstructural level caused by the forging process. Casting processes can create components with material properties which have to be treated with post-processing. (Pavithran et al., 2023) The low thermal conductivity and high hardness of the alloy can negatively affect the traditional manufacturing methods creating a need for subsequent steps in the manufacturing process. These subsequent steps can include for example machining, which can face problems such as low material removal and high tool wear rates. (Hosseini & Popovich, 2019)

The common phases in IN718 manufactured via laser-based powder bed fusion of metals (PBF-LB/Med) are shown in Table 2 with respective chemical formulations.

Table 2 Common phases in PBF-LB/Med IN718. (Volpato et al., 2022)

Phase	Chemical formulation
γ	Ni
γ′	Ni_3(Al, Ti)
γ″	Ni_3Nb
δ	Ni_3(Nb, Ti)
M_xC_y	Different formulations
Laves	(Ni, Fe, Cr)$_2$(Nb, Mo, Ti)

As Table 2 shows, the gamma (γ), gamma prime (γ′), gamma double prime (γ″), and delta (δ) phases are nickel-based. Where the γ consists entirely of nickel, the γ′ includes aluminium and titanium, and the γ″ niobium. The δ phase consists of nickel, niobium, and titanium. PBF-LB/Med IN718 includes different M_xC_y carbides with different formulations. The Laves phase consists of nickel, iron, chromium, niobium, molybdenum, and titanium. (Volpato et al., 2022)

The phases and their respective crystal structures and morphologies found in PBF-LB/Med IN718 are shown in Figure 1. These phases play a key role in the performance of the alloy. (Volpato et al., 2022)

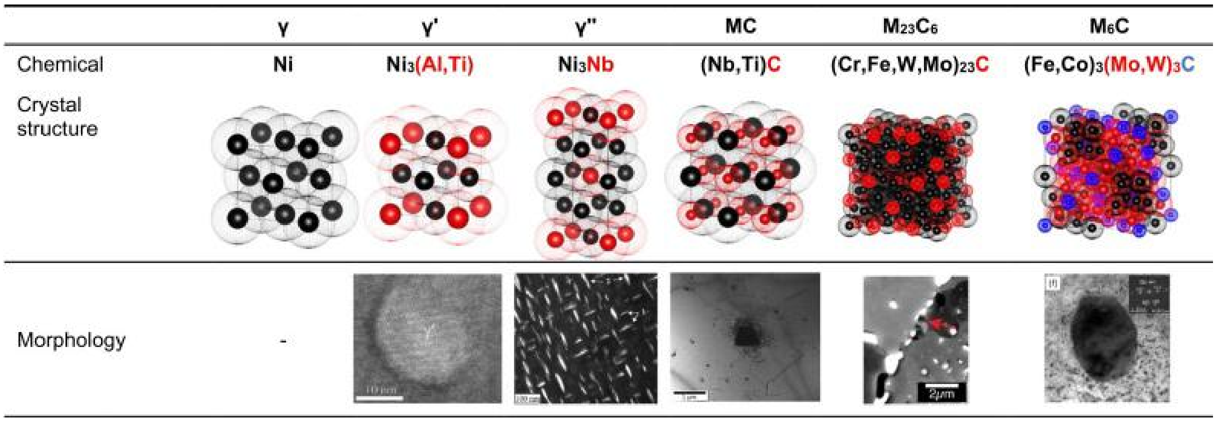

Figure 1 Phases present in PBF-LB/Med IN718. Reproduced and modified from Volpato et al., 2022 which is under an open access Creative Common CC BY license.

As Figure 1 shows, the matrix phase of the alloy is the nickel-based γ phase. This γ matrix is reinforced by precipitates, carbides, and solid solution elements. The primary precipitates are γ′ and γ″ phases. These strengthening precipitates account for a substantial part of the high strength and hardness of PBF-LB/Med IN718 at elevated temperatures. In addition, M_xC_y carbides add to the high strength of the alloy. The M in M_xC_y can stand for different metal elements such as chromium, molybdenum, and titanium. The C stands for carbon. Solid solution elements include e.g. molybdenum. The larger Mo atoms cause distortion in the Ni atoms in the γ phase adding to the strength of the alloy. (Volpato et al., 2022)

The microstructure of PBF-LB/Med IN718 can include undesired phases disadvantageous for the properties of the alloy, shown in Figure 2 with respective crystal structures and morphologies. (Volpato et al., 2022)

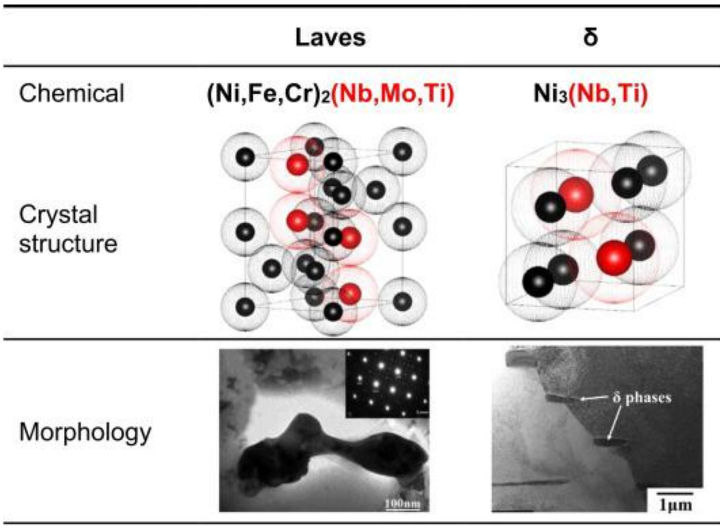

Figure 2 Undesired phases present in PBF-LB/Med IN718. Reproduced and modified from Volpato et al., 2022 which is under an open access Creative Common CC BY license.

As Figure 2 shows, these undesired phases include the δ and Laves phases. The δ phase located in intergranular areas can cause degradation in corrosion and fatigue resistances, fracture toughness, and ductility at elevated temperatures. The Laves phase serves as a starting point for void and crack nucleation. (Volpato et al., 2022)

2.2 Copper-chromium-zirconium CuCrZr

Copper-chromium-zirconium (CuCrZr) is a copper-based precipitation-hardening alloy consisting mainly of chromium (Cr) and zirconium (Zr) in addition to copper (Cu) with high thermal and electrical conductivities. (Salvan et al., 2021; Zhang et al., 2024) In addition, the material is resistant to mechanical wear (Diao et al., 2023) and is resistant to corrosion. (Tang, Chen, Sun, Liu, et al., 2022) These properties have made CuCrZr a commonly used material in heat dissipation and cooling applications in various fields, for example aerospace. The high electrical conductivity makes CuCrZr a viable candidate for use in electronic applications. (Zhang et al., 2024)

CuCrZr alloys consist of around 99 % of copper per weight, including relatively small amounts of chromium and zirconium. (Hu et al., 2022) Cr acts as a reinforcement in the Cu matrix and increases the overall strength at elevated temperatures. Similar to Cr, the addition of Zr increases the strength and additionally improves the ductility of the material at elevated temperatures. (Sarkeeva et al., 2018) Other elements such as iron and silicon may be present in addition to these main alloying elements. (Jeyaprakash et al., 2024) The weight percentages of elements can have variations. (Salvan et al., 2021) The weight percentages of the alloying elements found in CuCrZr are represented in Table 3.

Table 3 Alloying element composition of CuCrZr.
[1](Jeyaprakash et al., 2024), [2] (Salvan et al., 2021)

Element	Wt. %
Cu	Balance[1, 2]
Cr	1.6[1], 0.5 – 1.2[2]
Zr	0.3[1], 0.03 – 0.3[2]
Fe	0.4[1, 2]
Si	0.7[1, 2]

As Table 3 shows, CuCrZr consists mainly of copper, with additions of other elements.

Traditionally, CuCrZr components are manufactured mostly by forging and casting methods. Some components must go through different machining processes that contribute to feedstock material waste. A multi-phased manufacturing process contributes to an increased manufacturing time. Traditional manufacturing methods have their limitations regarding geometrical complexities. In addition, as-cast material can show reduced mechanical properties. (Jeyaprakash et al., 2024)

PBF-LB/Med CuCrZr mostly exhibit coarse grain formation, but fine grains are present in smaller amounts shown in scanning electron microscopy (SEM) micrographs in Figure 3.

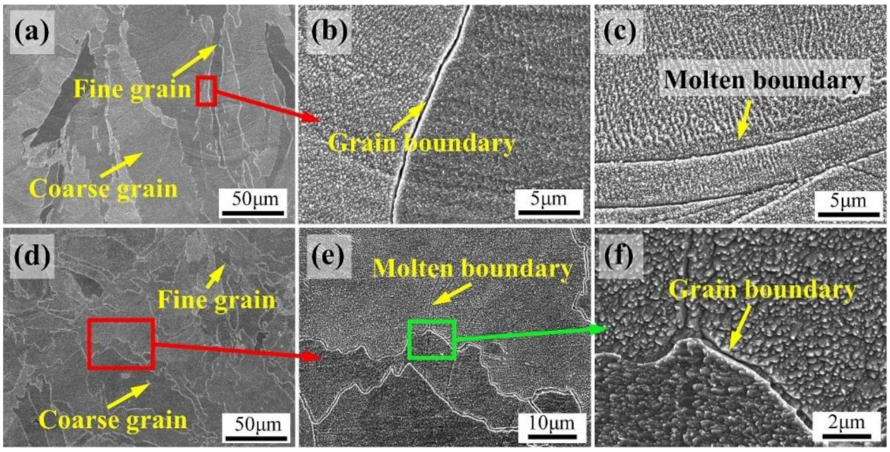

Figure 3 SEM micrographs of the microstructure of CuCrZr. Reproduced from Z. Li, Chen, et al., 2023 which is under an open access Creative Common CC BY license.

As Figure 3 shows, the grain formation and orientation are highly dependent on the melt pool temperature gradient and laser beam scanning direction. Figure 3a-c show the microstructure parallel to the building direction. Figure 3d-f show the microstructure vertical to the building direction. Fine grains are formed near the bottom region of the melt pool, vertical to the building direction. The temperature gradient is the largest at the bottom region of the melt pool. Curved coarse grains are formed at the melt pool boundaries. Formed grains show epitaxial growth along the melt pool in vertical and horizontal directions. This is due to the nature of the PBF-LB/M process, where in addition to the fresh powder layer being melted, also the previous layer(s) undergo remelting. (Z. Li, Chen, et al., 2023) The vertical and horizontal directions exhibit anisotropy in PBF-LB/Med CuCrZr,. (Hu et al., 2022)

3 Laser-based powder bed fusion of IN718 and CuCrZr

This chapter will cover the PBF-LB/M processes of the studied materials in this thesis, IN718 and CuCrZr, and the bimetallic material combination of IN718 and CuCrZr. The basic principles of PBF-LB and multi-material AM are explained in Appendix 1 .

3.1 PBF-LB/M of IN718

The need for complex IN718 components has led to the increase in interest of AMed components. (Zhong et al., 2023) IN718 is difficult to manufacture with traditional methods due to the low thermal conductivity and high hardness of the material. In traditional manufacturing methods, the composition of IN718 can cause difficulties with workability, machining processes, and elemental segregation. IN718 is a viable candidate for PBF-LB/M due to the weldability properties of the material (Deng, 2018) and IN718 has become a widely used material in PBF-LB/M. (Hosseini & Popovich, 2019) Relative densities of over 99 % have been reported for as-manufactured materials before undergoing any subsequent steps such as heat-treatment. (Balbaa et al., 2020)

The thermal conductivity of IN718 is low and depends on the manufacturing method. The thermal conductivity values are around 10 W/m·K for PBF-LB/Med IN718. (Hakeem et al., 2021) A study by Zhang et al., 2024 reported the value to be 12.3 W/m·K for as-manufactured material based on experiments.

Figure 4 shows different types of porosity defects observed in PBF-LB/Med IN718.

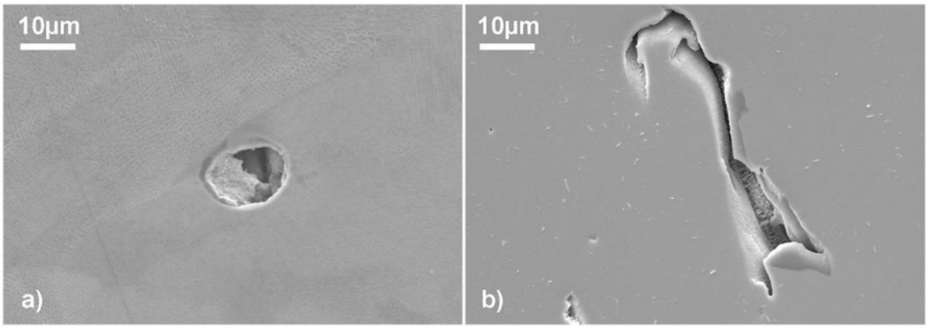

Figure 4 Porosity defects observed in PBF-LB/Med IN718. Reproduced from Hosseini & Popovich, 2019 which is under an open access Creative Common CC BY license.

Common defects in PBF-LB/Med IN718 include pores and cracks which can be caused by different factors. Porosity can be caused by, for example, entrapped gas during the manufacturing process, shown in Figure 4a. Porosity caused by lack of fusion between powder particles due to suboptimal process parameters or defects within the feedstock powder material is shown in Figure 4b. Pores caused by entrapped gas are usually circular in shape, as shown in Figure 4a. The shape of pores caused by lack of fusion can vary, as shown in Figure 4b. (Hosseini & Popovich, 2019) Cracks are often caused by residual stresses left in the material which is a common problem for PBF-LB/M. These residual stresses can be minimized with factors such as optimised process parameters. (Volpato et al., 2022) These prementioned defects in the as-manufactured material can be treated to a certain extent by different post-processing methods, although defects such as pores and cracks can be difficult or impossible to remove by post-processing. (Hosseini & Popovich, 2019)

Process parameters and machine models for PBF-LB/Med IN718 from literature are shown in Table 4.

Table 4 PBF-LB/M process parameters for IN718 found in literature.

Parameter	Laser power *P*	Scanning speed *v*	Hatch distance *h*	Layer thickness *t*	VED	Machine model
Reference	[W]	[mm/s]	[mm]	[mm]	[J/mm^3]	
Ostergaard et al., 2025	285	960	0.11	0.04	67.5	EOS M290
Guo et al., 2025	230	1500	0.13	0.04	29.5	EOS M290
Naskar et al., 2024a	275	950	0.11	0.04	65.8	EOS M280
Zhao et al., 2025	130	1200	0.08	0.03	45.1	Aconity MIDI
Chechik & Todd, 2023	95	1000	0.05	0.03	70.4	Aconity MINI

As Table 4 shows, the process parameters such as laser power *P*, scanning speed of laser beam *v*, hatch distance *h*, and layer thickness *t* differ between different machines and processes. As a result of different process parameters, the volumetric energy density (VED) values for each process differ.

3.2 PBF-LB/M of CuCrZr

CuCrZr, and other similar copper alloys, present material specific problems when manufactured with PBF-LB/M mainly due to their high copper content. (Salvan et al., 2021) The high reflectivity of the material causes poor absorption of energy, when using a laser beam as a thermal energy source. The high reflectivity decreases the amount of energy utilized for melting and fusing the feedstock material layers. This leads to a decrease in the process efficiency and can in addition cause harm to the equipment hardware. (Tang, Chen, Sun, Liu, et al., 2022) The reflectivity is dependent on the wavelength of the laser beam. For a laser beam with a wavelength of 1064 nm, the reflectivity value is close to 90 %. (Sun et al., 2020)

The high thermal conductivity of CuCrZr, the property which makes it a viable candidate for many applications as a finished product, is a weak point for PBF-LB/M. The high thermal conductivity causes fast heat dissipation and high thermal gradients within relatively small distances during the manufacturing process. The high thermal conductivity can cause curling, a form of warping, within the fused layers and lead to delamination between the layers. (Tang, Chen, Sun, Liu, et al., 2022) The thermal conductivity of CuCrZr is around 330 W/m·K. (Zhang et al., 2024) However, as-manufactured material can have lower thermal conductivity values, as reported in a study by Zhang et al., 2024. This value was reported to be 104 W/m·K. This can be caused by the high cooling rate during the PBF-LB/M process which can result in high residual stresses and other defects, including un-melted powder particles, cracks, and pores. (Zhang et al., 2024) However, high relative densities can be obtained with optimised process parameters. A study by Wang et al., 2023 reported a relative density of over 98 % for as-manufactured material.

Figure 5 shows the changes in relative material densities based on changes in linear energy density (LED) values in PBF-LB/M processes observed by Wang et al., 2023.

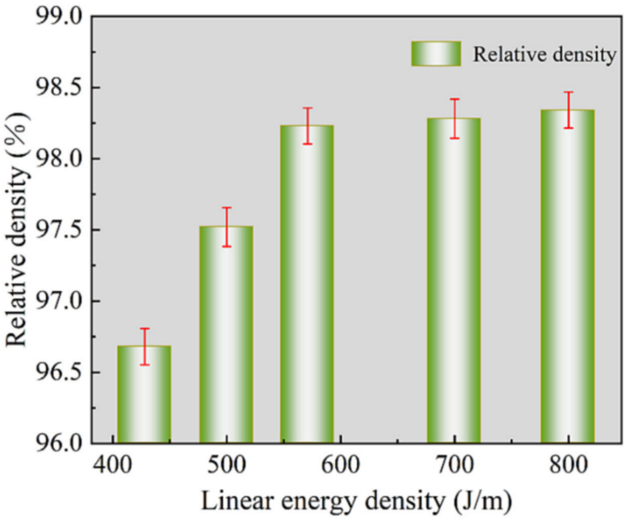

Figure 5 Relative material densities and LED values of different PBF-LB/M processes. Reproduced and modified from Wang et al., 2023 which is under an open access Creative Common CC BY license.

As Figure 5 shows, a PBF-LB/M process with an LED value of 570 J/m resulted in a relative density of 98.2 ± 1.4 %. The relative density values are observed to rise to a certain level as the LED value increases. A process with an LED value of 800 J/m resulted in a relative density of 98.3 ± 1.4 %. Processes with an LED value lower than 571 J/m resulted in lower relative densities. (Wang et al., 2023)

The PBF-LB/M process of CuCrZr can be enhanced with a remelting phase in which the previously fused layers are scanned with the laser beam for a second time to account for the high reflectivity and thermal conductivity. (Meyer et al., 2025; Xu et al., 2024) By doing this, the energy density of the first scan can be lowered to avoid problems such as keyholing. A low energy density value can lead to defects such as improperly bonded layers and pores. These defects can be managed by the remelting phase allowing for a smoother surface quality and an increased relative density. (Xu et al., 2024) A study by Xu et al., 2024 reported a relative density value of 99.8 % after using the remelting process. A downside for the remelting process is the added time to the manufacturing process. Although, this extended manufacturing time can yield higher material quality and should be considered with that in mind. (Xu et al., 2024) The PBF-LB/M process parameters used in a study by Meyer et al., 2025 for the melting and remelting phases are shown in Table 5. The machine used by Meyer et al., 2025 was an Aconity MIDI+ machine equipped with a 1000 W laser with a laser beam wavelength of 1070 nm.

Table 5 Process parameters for melting and remelting phases used by Meyer et al., 2025 for CuCrZr.

Parameter	Laser power *P*	Scanning speed *v*	Hatch distance *h*	Layer thickness *t*	VED
Phase	[W]	[mm/s]	[mm]	[mm]	[J/mm^3]
Melting	500	550	0.12	0.04	189
Remelting	500	600	0.12	0.04	174

As Table 5 shows, both phases used a laser power P of 500 W, hatch distance h of 0.12 mm, and layer thickness t of 0.04 mm. The scanning speed of the laser beam v was increased from 550 to 600 mm/s between the melting and remelting phases. The increase in the scanning speed decreased the VED value from 189 to 174 J/mm^3 between the melting and remelting phases. (Meyer et al., 2025)

A study by Xu et al., 2024 shows that the properties of PBF-LB/Med CuCrZr can improve with the use of the additional remelting phase. Remelting results in reduced grain and precipitate sizes within the material and improves the general performance, including e.g. mechanical performance and electrical conductivity, of the material. (Xu et al., 2024)

Figure 6 shows CuCrZr melt pool simulation results presented in a study by Wang et al., 2023. The process parameters in the simulation are 350 W for the laser power and 600 mm/s for the scanning speed.

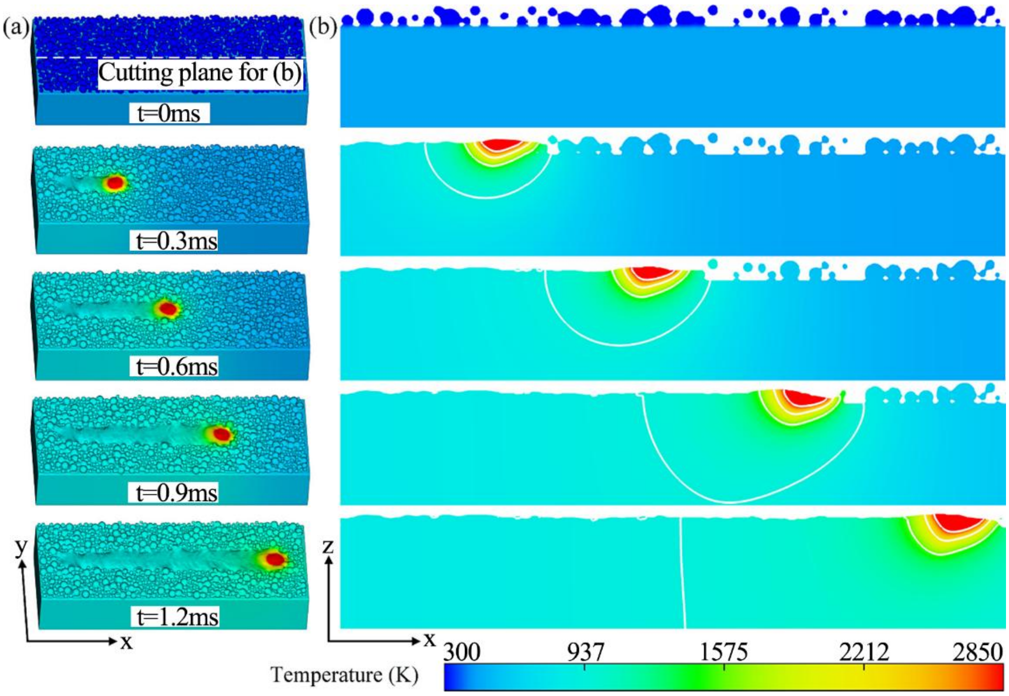

Figure 6 Visualisation from melt pool simulation of CuCrZr in a PBF-LB/M process. Reproduced and modified from Wang et al., 2023 which is under an open access Creative Common CC BY license.

Melt pool simulation results by Wang et al., 2023 show that the CuCrZr melt pool is near to circular in shape, as shown in Figure 6a. Materials with lower thermal conductivities usually exhibit a comet shaped melt pool, in which the circular melt pool area is followed by a more gradually cooling “tail” section. (Wang et al., 2023) Figure 6b shows the longitudinal section along the centre axis shown in Figure 6a.

3.3 PBF-LB/M of bimetallic material of IN718 and CuCrZr

IN718 (Volpato et al., 2022) and CuCrZr (Cortis et al., 2023) are both known materials in additive manufacturing. However, multi-material AM of this bimetallic combination lacks research and results are scarce.

The matrix materials in both alloys have a face-centred-cubic crystal structure which helps with forming a bond between the two materials when manufactured with PBF-LB/M. In addition, the difference in atom sizes between nickel and copper is small. (Z. Li, Kuai, et al., 2023) Marangoni convection plays a key role in the formation of the interface zone between IN718 and CuCrZr. (Zhang et al., 2024) The definition of Marangoni convection is the movement of fluid induced by unequal surface tensions. (Sheikholeslami & Ganji, 2018) The different surface tensions between the two materials produce nickel and copper rich areas during the PBF-LB/M process. Detached IN718 areas tend to form surrounded by CuCrZr whereas CuCrZr is found to form at the boundaries of the melt pool. The high thermal energy required by CuCrZr combined with the low thermal conductivity of IN718 leads to the formation of a deep melt pool which increases the area of the diffusion between the two materials. (Z. Li, Kuai, et al., 2023; Zhang et al., 2024)

A study by Zhang et al., 2024 on the PBF-LB/M process of manufacturing bimetallic material of IN718 and CuCrZr showed promising results. The machine used to manufacture bimetallic samples by Zhang et al., 2024 was an EOS M280 machine equipped with a 400 W IPG Photonics laser with a wavelength of 1064 nm. The process parameters for IN718 are shown in Table 6.

Table 6 Process parameters used by Zhang et al., 2024 for IN718.

Parameter	Laser power *P*	Scanning speed *v*	Hatch distance *h*	VED
Sample	[W]	[mm/s]	[mm]	[J/mm^3]
All	285	960	0.11	90.0

Zhang et al., 2024 used the same process parameters for nine bimetallic samples, as Table 6 shows. The laser power *P* was 285 W, scanning speed *v* 960 mm/s, hatch distance *h* 0.11 mm. The reported VED value of the process was 90.0 J/mm^3.

Zhang et al., 2024 varied the process parameters for CuCrZr in the manufacturing of the nine bimetallic samples. The parameters for each sample are shown in Table 7.

Table 7 Process parameters used by Zhang et al., 2024 for CuCrZr

Parameter	Laser power *P*	Scanning speed *v*	Hatch distance *h*	VED
Sample	[W]	[mm/s]	[mm]	[J/mm^3]
1	310	350	0.08	Not reported
2	310	400	0.10	Not reported

3	310	450	0.12	Not reported
4	340	350	0.10	Not reported
5	340	400	0.12	236
6	340	450	0.08	Not reported
7	370	350	0.12	Not reported
8	370	400	0.08	Not reported
9	370	450	0.10	Not reported

As Table 7 shows, the laser power *P* was varied from 310 to 370 W. The scanning speed *v* was varied between 350 and 450 mm/s. Hatch distance *h* ranged from 0.08 to 0.12 mm. A VED value of 236 J/mm^3 was only reported for the number 5 sample.

The main defect according to Zhang et al., 2024 was porosity in the interface zone of the bimetallic material. The effects of laser power, scanning speed, and hatch distance on the material defect ratio are shown in Figure 7.

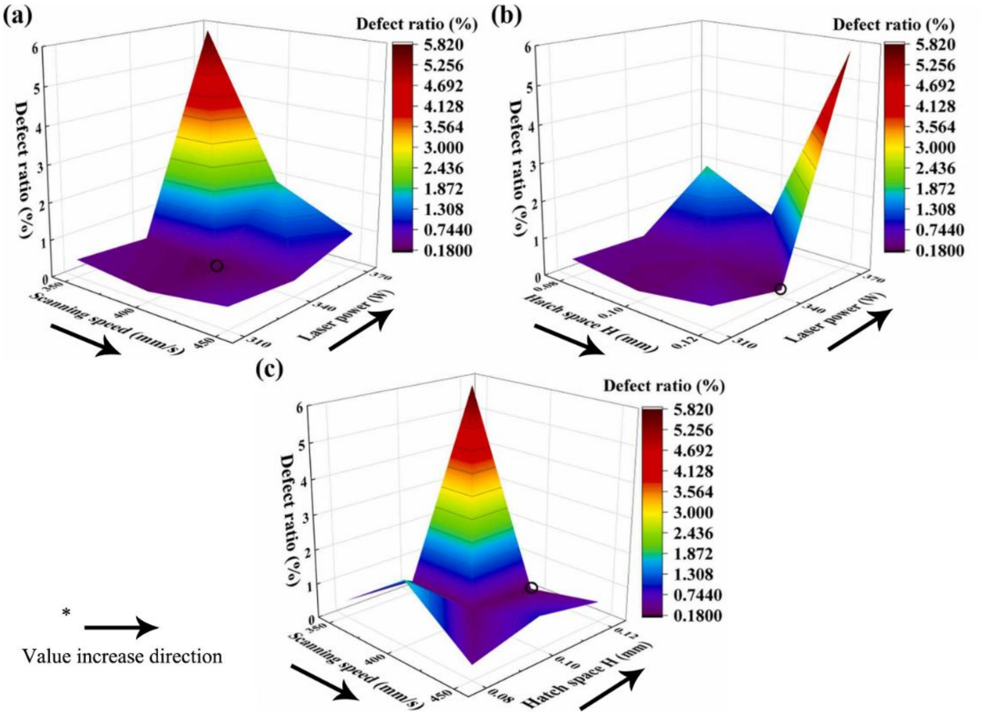

Figure 7 Effects of process parameters on the defect ratio of the bimetallic material. Reproduced and modified from Zhang et al., 2024 which is under an open access Creative Common CC BY license.

Figure 7a shows the relation between scanning speed and laser power. The highest defect ratio was observed when the scanning speed was low, and laser power was high. The defect ratio was observed to stay low throughout the different scanning speeds with a low laser power. The defect ratio was observed to rise as the laser power was increased while using a high scanning speed. (Zhang et al., 2024)

Figure 7b shows the relation between hatch distance and laser power. The highest defect ratio was observed when the laser power was high, and hatch distance was narrow. The defect ratio was observed to stay low throughout the different hatch distance values with a low laser power. The defect ratio was observed to rise as the laser power was increased while using a narrow hatch distance. (Zhang et al., 2024)

Figure 7c shows the relation between scanning speed and hatch distance. The highest defect ration was observed when the scanning speed was low, and the hatch distance was wide. The defect ratio was observed to stay low with scanning speeds of 350 mm/s and 450 mm/s with a narrow hatch distance. An increase in the defect ratio was observed with a scanning speed of 400 mm/s. The defect ratio was observed to stay low throughout the range of hatch distance values. (Zhang et al., 2024)

Zhang et al., 2024 observed that using low values of energy input, following a low value of laser power and high value of scanning speed, increased the porosity levels and resulted in insufficient powder melting. A high energy input, following a high laser power and low scanning speed, led to uneven melt pool behaviour and splashing of molten material. A narrow hatch distance in combination with a large overlap of laser scans was observed to be beneficial for the melt pool behaviour. The higher value of energy input required by CuCrZr increases the risk of keyhole formation in IN718 close to the transition zone, as the thermal conductivity of CuCrZr is higher than of IN718. (Zhang et al., 2024)

4 Heat treatment

In this thesis only heat treatment as a post-processing step will be covered as it is relevant to the study and fits within the timetable.

4.1 Heat treatment of IN718

The microstructure of as-manufactured IN718 can be altered by heat treatment leading to enhanced mechanical properties.

A study by Naskar et al., 2024a investigated the effects of three different heat treatment processes on PBF-LB/Med IN718. The heat treatment processes are named as “HT1”, “HT2”, and “HT3”.

The first heat treatment process (HT1) by Naskar et al., 2024a consisted of a 2-hour solution treatment at 1040 °C followed by air cooling to room temperature. A two-step aging process started with an 8-hour aging at 720 °C and cooling to 620 °C with a 55 °C/h cooling rate. The second aging step consisted of an 8-hour aging at 620 °C followed by air cooling to room temperature.

The second heat treatment process (HT2) featured a solution treatment at 1080 °C for 2 hours. The same aging procedure as in HT1 was used.

The third heat treatment process (HT3) featured a 2-hour homogenization treatment at 1093 °C followed by air cooling to room temperature. Following this, a solution treatment was conducted at 980 °C for 1 hour. HT3 featured the same aging procedure as HT1 and HT2.

The advantages and disadvantages of each three heat treatment process according to test results by Naskar et al., 2024a are shown in Table 8.

Table 8 Advantages and disadvantages of different heat treatment processes. (Naskar et al., 2024a)

HT1	HT2	HT3
+ Highest hardness	+ Homogenous + Lowest wear rate + Lowest friction coefficient + Lowest peak-to-valley roughness	+ Homogenous
− Laves phase present − Highest wear rate − Highest friction coefficient		− Lowest hardness

− Highest peak-to-valley roughness		

As Table 8 shows, HT1 resulted in the highest hardness of all three heat treatment processes. On the other hand, it had the most disadvantages of all three processes. HT2 had the highest number of advantages and had no disadvantages when compared to the other two processes. HT3 resulted in homogeneity, as did HT2, but HT3 showed the lowest hardness of the three processes.

Naskar et al., 2024a observed multiple changes in material properties after the heat treatment processes, shown in Figure 8.

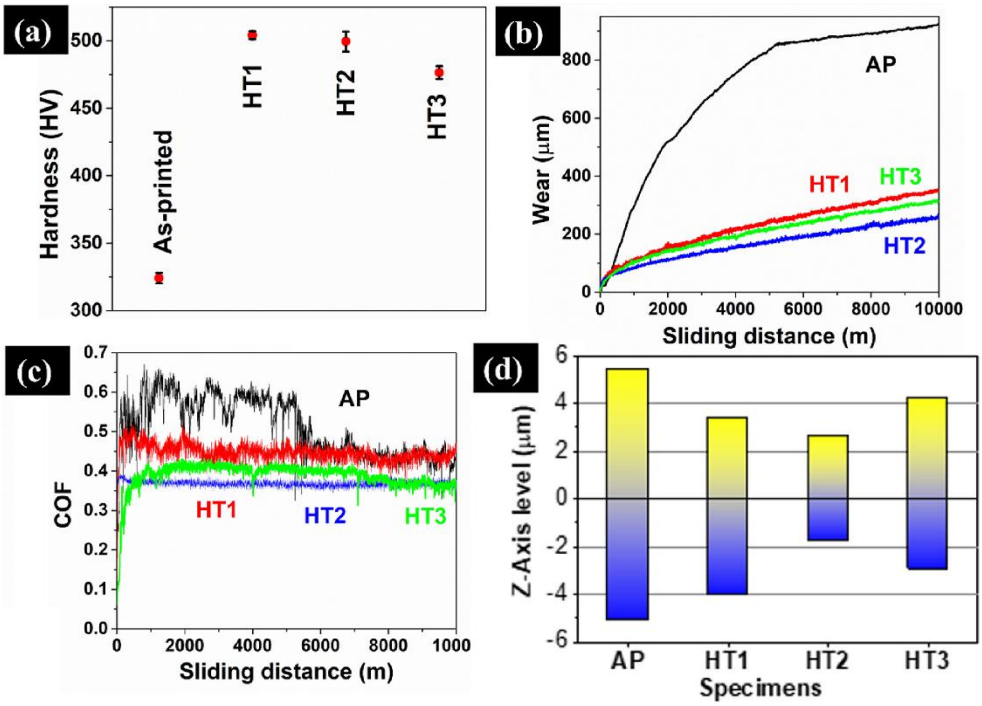

Figure 8 Hardness, wear rate, coefficient of friction, and peak-to-valley surface roughness values. Reproduced and modified from Naskar et al., 2024a which is under an open access Creative Common CC BY license.

As shown in Figure 8a, Naskar et al., 2024a observed an increase in hardness with all three heat treatment processes. The wear rates, in Figure 8b, and coefficients of friction (COF), in Figure 8c, were observed to decrease in wear resistance tests after the heat treatments. In addition, the peak-to-valley surface roughness was observed to decrease in heat-treated materials after wear resistance tests, as shown in Figure 8d. The numerical values of the results are shown in Table 9.

Table 9 Numerical values for hardness, wear rate, COF, and peak-to-valley roughness reported by Naskar et al., 2024a.

Material property Sample	Hardness [$HV_{0.5}$]	Wear rate [µm]	COF	Surface roughness [µm]
As-manufactured	324 ± 4	922 ± 13	0.51 ± 0.07	-5.10 – 5.40
HT1	504 ± 3	345 ± 4	0.45 ± 0.02	-4.00 – 3.38
HT2	499 ± 7	262 ± 5	0.37 ± 0.01	-1.76 – 2.60
HT3	476 ± 4	329 ± 15	0.39 ± 0.03	-2.95 – 4.19

As Table 9 shows, the hardness value increased from 324 ± 4 $HV_{0.5}$ in as-manufactured condition to 504 ± 3 $HV_{0.5}$ after heat treatment HT1. Wear rates decreased with all heat treatments from 922 ± 13 µm, the lowest value being 262 ± 5 µm in HT2. All heat treatments lowered the COF values from the as-manufactured condition value of 0.51 ± 0.07, lowest value being 0.37 ± 0.01 in HT2. The lowest peak-to-valley roughness after wear resistance tests was observed to be in the range of -1.76 – 2.60 µm, in HT2. The highest peak-to-valley roughness value was observed in the as-manufactured material with a range of -5.10 – 5.40 µm.

As-manufactured IN718 shows formation of columnar dendrites on melt pool boundaries, and formation of the Laves phase. In addition, the as-manufactured material lacks in γ' and γ'' phases causing reduced material properties. Both undesired dendritic microstructure and Laves phase can be reduced or removed with heat treatments. Heat treatment can result in the desired precipitation of the γ' and γ'' phases, in addition to minimizing and removing undesired phases and microstructure. However, some heat treatment processes were noticed to cause formation of the δ phase reducing the formation of γ''. (Naskar et al., 2024b)

Figure 9 shows SEM micrographs of as-manufactured and heat-treated materials.

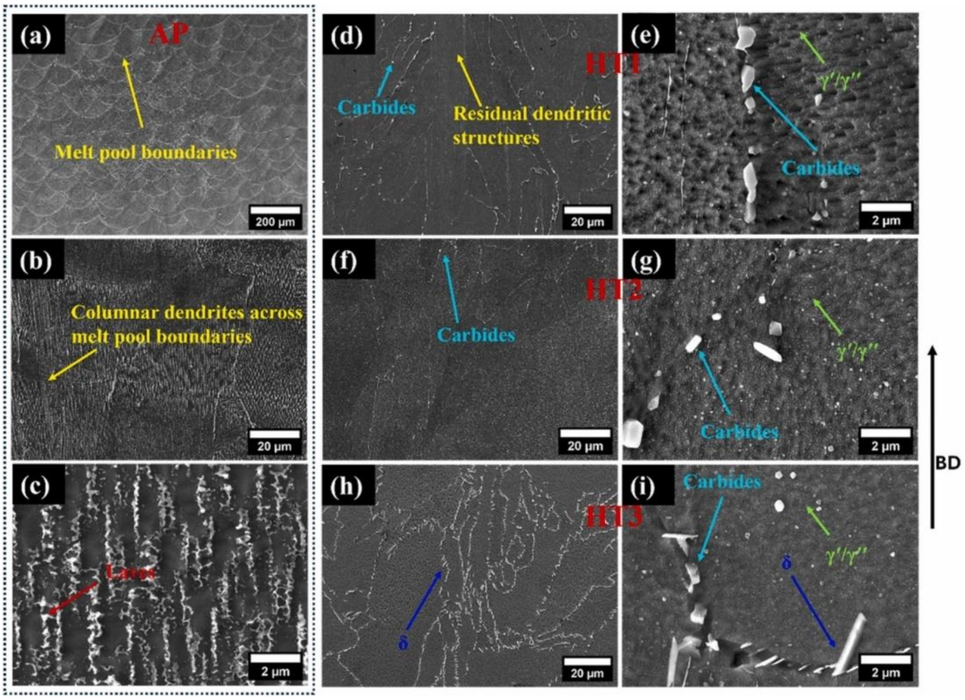

Figure 9 SEM micrographs of as-manufactured and heat-treated IN718. Reproduced from Naskar et al., 2024b which is under an open access Creative Common CC BY license.

The building direction is shown by “BD” marked with the black arrow in Figure 9. Figure 9a-c show SEM micrographs of the as-manufactured material. A scale pattern is observed left by melt pool boundaries from the PBF-LB/M process in Figure 9a. Figure 9b shows columnar dendrites at melt pool boundaries. The red arrow shows a formed Laves phase in Figure 9c.

Figure 9d-e display the material after the heat treatment process HT1. Residual dendritic structures and carbides are visible in Figure 9d. Figure 9e shows carbides on grain boundaries and γ' and γ'' phases. Figure 9f-g display the material after the HT2 process. A fully solutionised microstructure with carbides is visible in Figure 9f. Figure 9g shows carbides on grain boundaries, and γ' and γ'' phases. Figure 9h-i display the material after the HT3 process. Large precipitation of δ phase is visible in Figure 9h. Figure 9i shows carbides on grain boundaries, and γ' and γ'' phases, with addition of δ phase.

Naskar et al. 2025 studied the effects of the same heat treatment processes, HT1, HT2, and HT3, on the tensile properties of PBF-LB/Med IN718. The reported results are shown in Table 10.

Table 10 Numerical results for yield strength, ultimate tensile strength, elongation, and elastic modulus reported by Naskar et al., 2025.

Tensile property	Yield strength	Ultimate tensile strength	Elongation	Elastic modulus
Sample	[MPa]	[MPa]	[%]	[GPa]
As-manufactured	736 ± 15	1090 ± 16	24.8 ± 1.	191 ± 1
HT1	1210 ± 21	1530 ± 8	13.1 ± 0.3	204 ± 3
HT2	1280 ± 16	1570 ± 5	13.9 ± 0.1	210 ± 0.9
HT3	1250 ± 16	1540 ± 7	13.1 ± 0.1	201 ± 4

As Table 10 shows, all heat treatment processes increase the yield and ultimate tensile strengths of the material compared to the as-manufactured material. The yield strength increased from the as-manufactured condition of 736 ± 15 MPa to 1280 ± 6 MPa with HT2. The ultimate tensile strength increased from the as-manufactured condition of 1090 ± 6 MPa to 1570 ± 5 MPa with HT2. The elastic modulus increased with all heat treatments. The lowest value was 191±1 GPa in the as-manufactured material and the highest in HT2 with a value of 210 ± 0 GPa. The elongation decreased from 24.8 ± 1 % after all heat treatment processes compared to the as-manufactured material. The lowest elongation value of 13.1 ± 0.3 % was observed after HT1.

4.2 Heat treatment of CuCrZr

The high cooling rate in PBF-LB/M does not allow for the chromium and zirconium elements to precipitate from the copper matrix leading to the formation of solid solutions that are supersaturated. This eliminates the need to perform solid solution treatments. (Z. Li, Chen, et al., 2023)

In a study by Li et al., 2023 the effects of direct age hardening heat treatments on PBF-LB/Med CuCrZr were analysed. Samples underwent different direct age hardening heat treatment cycles and the results were compared to as-manufactured material. Li et al., 2023 used four different heat treatment temperatures with four different time periods. The heat treatment temperatures and respective time periods are shown in Table 11.

Table 11 Direct age hardening heat treatments used by Z. Li, Chen, et al., 2023.

Temperature [°C]	Time [min]	Cooling method
420	30, 60, 90, 120	Air cooling
460	30, 60, 90, 120	Air cooling
500	30, 60, 90, 120	Air cooling

540	30, 60, 90, 120	Air cooling

As Table 11 shows, the heat treatment temperatures varied between 420 and 540 °C. The heat treatment times varied between 30 and 120 minutes. All heat treatments were followed by air cooling.

Figure 10 shows optical micrographs of as-manufactured and heat-treated materials parallel to the building direction.

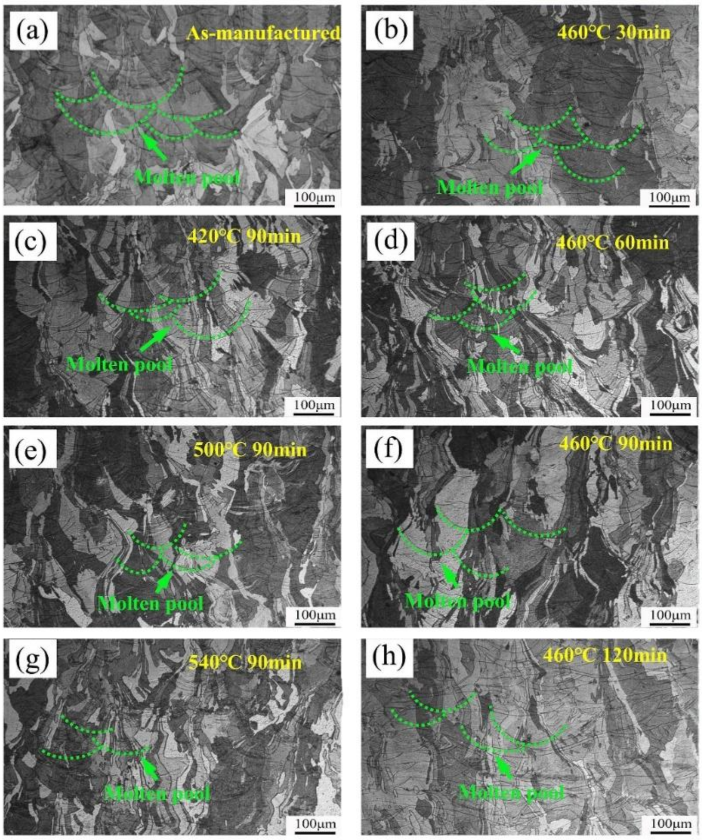

Figure 10 Microstructure of as-manufactured and heat-treated CuCrZr parallel to the building direction. Reproduced and modified from (Z. Li, Chen, et al., 2023)) which is under an open access Creative Common CC BY license.

Z. Li, Chen, et al., 2023 reported no significant changes in morphologies and grain sizes after the aging heat treatment processes. Coarse columnar grains and localized fine grains are still observed, as Figure 10 shows. This is due to the relatively low temperatures of direct age hardening heat treatments, compared to solution treatments. (Z. Li, Chen, et al., 2023)

Figure 11 shows optical micrographs of the as-manufactured and heat-treated materials vertical to the building direction.

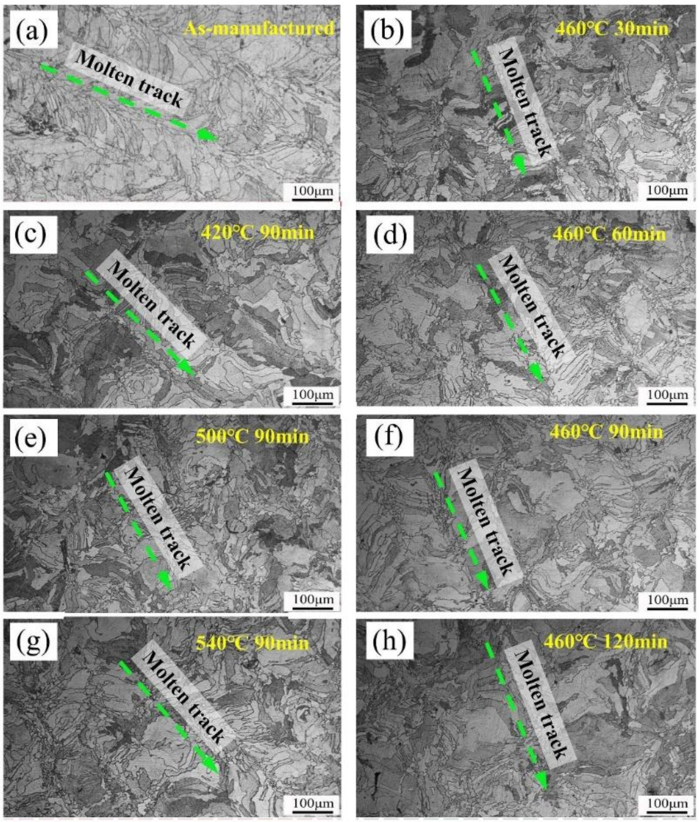

Figure 11 Microstructure of as-manufactured and heat-treated CuCrZr vertical to the building direction. Reproduced and modified from (Z. Li, Chen, et al., 2023)) which is under an open access Creative Common CC BY license.

As Figure 11 shows, there are no significant changes in the morphologies and grain sizes after the heat treatment processes. In addition, the laser beam scanning tracks remain visible. (Z. Li, Chen, et al., 2023) Figure 11 shows the nature of the PBF-LB/M process with CuCrZr, where the centre area of the scanning track consists of small grains, and the edges of larger grains. (Z. Li, Chen, et al., 2023)

In a study by Wallis & Buchmayr, 2019 the effects of solution annealing, age hardening, and direct age hardening on the thermal conductivity and hardness of CuCrZr were studied. The different treatment cycles are shown in Table 12.

Table 12 Heat treatments used by Wallis & Buchmayr, 2019.

Heat treatment	Temperature [°C]	Time [min]	Cooling method

Solution annealing	950	15	Water quenching
Solution annealing + Age hardening	950 + 450	15 + 120	Water quenching + air cooling
Direct age hardening	400, 420, 450, 480, 500, 550, 580	10, 30, 60, 120, 180, 300	Air cooling

As Table 12 shows, the solution annealing temperature was 950 °C. Age hardening temperatures varied from 400 to 580 °C. Heat treatment times varied from 15 to 300 minutes. Cooling was conducted by water quenching and air cooling depending on the heat treatment.

The thermal conductivity and hardness values acquired by Wallis & Buchmayr, 2019 from the as-manufactured, solution annealed, and age hardened material samples are shown in Table 13.

Table 13 Thermal conductivity and hardness values reported by Wallis & Buchmayr, 2019.

Sample	Thermal conductivity [W/m·K]	Hardness [$HV_{1.0}$]
As-manufactured	100 ± 2	80.0 ± 2
Solution annealing	192 ± 4	77.0 ± 2
Solution annealing + age hardening	297 ± 6	126 ± 2

As Table 13 shows, the thermal conductivity of CuCrZr rises from 100 ± 2 to 297 ± 2 W/m·K with all heat treatment types. The hardness value decreases with solution annealing from 80.0 ± 2 to 77.0 ± 2 $HV_{1.0}$ and then again increases to 126 ± 2 $HV_{1.0}$ with the addition of age hardening, compared to the as-manufactured material.

The effects of the different direct age hardening treatments on hardness and thermal conductivity are shown in Figure 12.

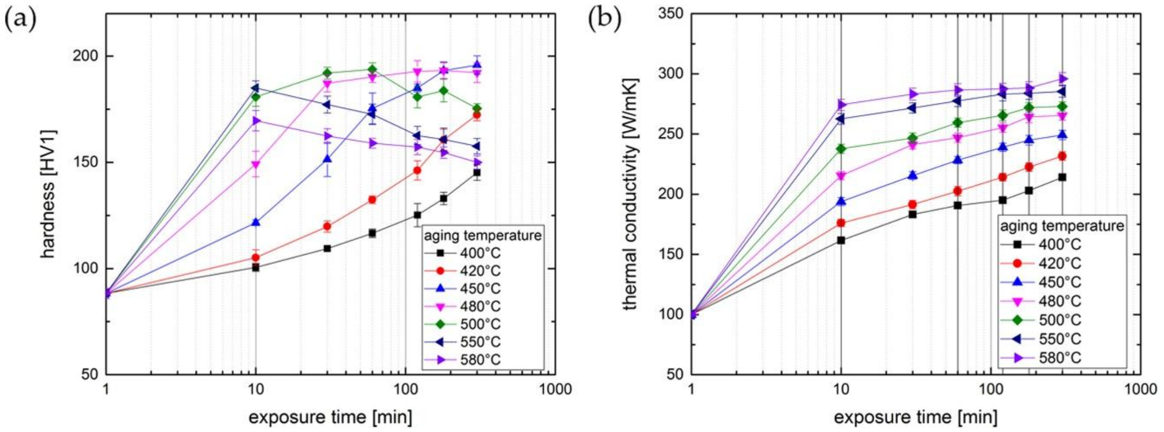

Figure 12 Hardness and thermal conductivity value visualisation after direct age hardening. Reproduced from Wallis & Buchmayr, 2019 which is under an open access Creative Common CC BY license.

As Figure 12a shows, all the direct age hardening temperatures result in an initial increase in reported hardness values. However, the hardness values begin to decrease after individual exposure times, in the direct age hardening temperatures ranging from 480 °C to 580 °C. The hardness value is increasing throughout the exposure time range in temperatures ranging from 400 °C to 450 °C. This is explained by over-aging. (Wallis & Buchmayr, 2019)

Figure 12b shows the effect of the direct age hardening temperatures to the thermal conductivity values. Here, the values increased depending on the exposure time and a higher aging temperature led to higher thermal conductivity values.

4.3 Heat treatment of bimetallic material of IN718 and CuCrZr

A compromise between the two heat treatments must be selected for the bimetallic material, as the heat treatment procedures for both IN718 and CuCrZr are different,. Zhang et al., 2024 used a three-phased heat treatment procedure for the manufactured bimetallic material samples. At first, the samples were heated to 720 °C with a heating rate of 55 °C/h. The temperature of 720 °C was held for 8 hours. After the first phase, the heat treatment temperature was lowered to 620 °C and held for 8 hours. As the last step, the samples were air cooled to room temperature.

The thermal conductivity of the bimetallic samples improved from 31.9 to 75.0 W/m·K with heat treatment which is mainly due to reductions in dislocation density and of thermal stresses, and dissolution of precipitation atoms. (Zhang et al., 2024) SEM micrographs and energy-dispersive X-ray spectroscopy (EDS) mappings are shown in Figure 13.

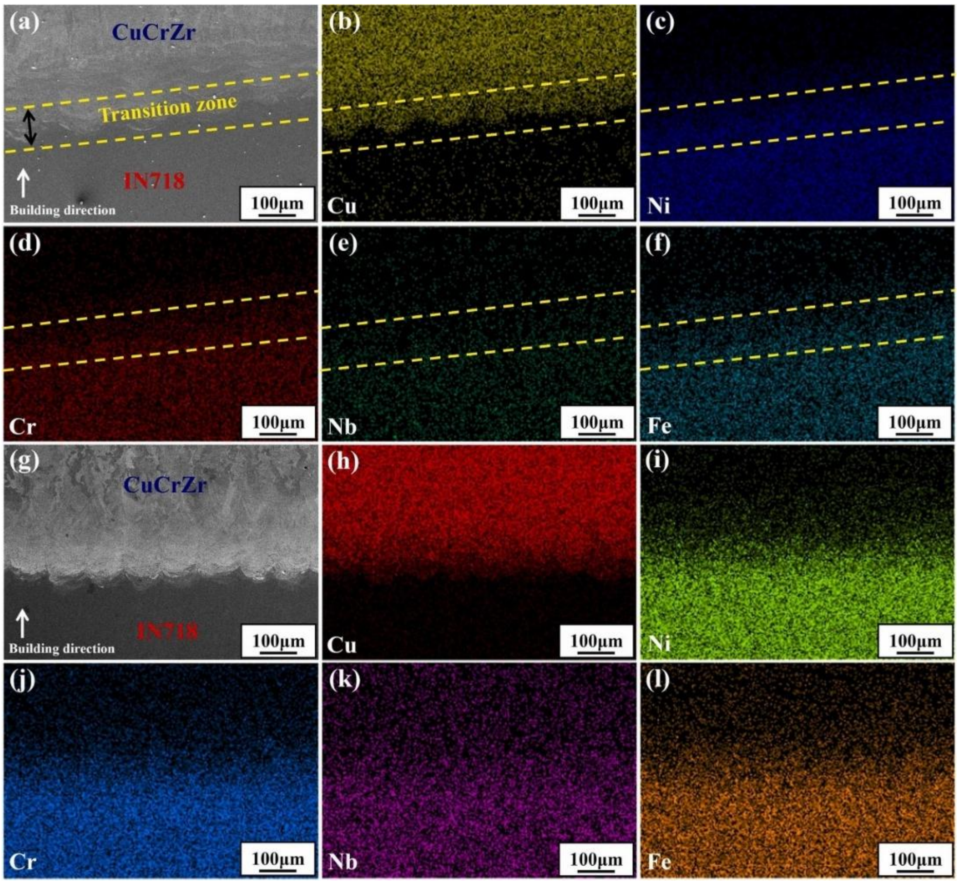

Figure 13 SEM micrographs and EDS mappings of bimetallic material of IN718 and CuCrZr. Reproduced from Zhang et al., 2024 which is under an open access Creative Common CC BY license.

Figure 13a shows an SEM micrograph of the bimetallic material before heat treatment. Figure 13g shows an SEM micrograph after heat treatment. The distinction between the IN718 and CuCrZr zones is more visible after heat treatment between Figure 13a and Figure 13g. Figure 13b-f show the EDS mapping of each element, Cu, Ni, Cr, Nb, and Fe, before heat treatment. As a comparison, Figure 13h-l show the EDS mapping of the same elements after heat treatment. The alloying element diffusion became more visible after heat treatment in the EDS mapping as the contrast differences between colours shows. In addition, the diffusion distance has increased and precipitates are not observed. (Zhang et al., 2024)

5 Properties of bimetallic material of IN718 and CuCrZr

The bimetallic material of IN718 and CuCrZr combines the high temperature strength of IN718 with the high thermal conductivity of CuCrZr.

In a study by Zhang et al., 2024, the PBF-LB/M process of manufacturing the bimetallic material was studied and the results analysed. Samples manufactured with different process parameters were analysed for elemental distribution, crystallization properties, distribution of elements, phase composition, and microstructure of the interface zone. Optimised parameters were chosen from the different tested process parameters. The optimised parameters are shown in Table 14.

Table 14 Optimised parameters used by Zhang et al., 2024 for manufacturing bimetallic material of IN718 and CuCrZr.

Parameter	Laser power *P*	Scanning speed *v*	Hatch distance *h*	VED
Material	[W]	[mm/s]	[mm]	[J/mm^3]
IN718	285	960	0.11	90.0
CuCrZr	340	400	0.12	236

As Table 14 shows, the process parameters were 285 W for laser power, 960 mm/s for scanning speed, 0.11 mm for hatch distance, and the reported VED value was 90.0 J/mm^3 for IN718. The parameters were 340 W for laser power, 400 mm/s for scanning speed, 0.12 mm for hatch distance, and the reported VED value was 236 J/mm^3 for CuCrZr. The process parameters were kept constant for all CuCrZr layers. (Zhang et al., 2024) A separate remelting phase was not mentioned to have been used with CuCrZr. The machine used by Zhang et al., 2024 was an EOS M280 machine equipped with a 400 W IPG Photonics laser with a laser beam wavelength of 1064 nm.

Zhang et al., 2024 studied the mechanical properties, hardness, and thermal conductivity of the samples to test the interfacial bonding of the bimetallic material and conducted a series of longitudinal and transverse tensile tests.

Zhang et al., 2024 were able to manufacture samples without porosity or cracking in the interface zone with optimised process parameters, shown in Table 14. The samples showed distinct material zones with a transition zone in between. The IN718 zone consisted of columnar and fine dendrites, and columnar cellular crystals. The CuCrZr zone was observed to have a large grain size with columnar crystals and signs of a semi-circular, shallow melt pool. Nickel and copper elements showed diffusion leading to a metallurgical bond at the interface zone. Fracturing happened in the CuCrZr zone in tensile tests, showing that the two materials in the interface have bonded.

The equipment used for testing and analysing the samples used by Zhang et al., 2024 are shown in Table 15.

Table 15 Testing and analysis equipment used by Zhang et al., 2024.

Make and model	Type	Tested/analysed property
Nikon Epiphot 300	Optical microscope	Microstructure analysis
Hitachi SU3500	Scanning electron microscope	Microstructure analysis
Bruker D8 Advance	X-ray diffractometer	Phase composition analysis
FEI Quanta 650	Field emission scanning electron microscope	Microstructure analysis
Taiming HXD 1000TM/LCD	Hardness tester	Hardness testing
Shimadzu AGS-X	Tensile testing machine	Tensile testing
Netzsch LFA 457	Laser thermal conductivity analyser	Thermal conductivity testing

As Table 15 shows, a Nikon Epiphot 300 optical microscope and Hitachi SU3500 SEM were used for microstructure analysis. A Bruker D8 Advance X-ray diffractometer was used to material phase composition analysis. In addition, the microstructure was analysed with a FEI Quanta 650 field emission scanning electron microscope. A Taiming HXD 1000TM/LCD hardness tester was used for hardness testing. Tensile tests were performed with a Shimadzu AGS-X tensile testing machine. Thermal conductivity was analysed with a Netzsch LFA 357 laser thermal conductivity analyser.

The reported material property results obtained by Zhang et al., 2024 are shown in Table 16.

Table 16 Material property test result values reported by Zhang et al., 2024.

Material property	Reported values
Hardness	330 ± 5 $HV_{0.5}$ (IN718), 169 ± 4 $HV_{0.5}$ (interface), 86.0 ± 4 $HV_{0.5}$ (CuCrZr)
Maximum ultimate tensile strength	1040 ± 12 MPa (IN718) 190 ± 12 MPa (interface, transverse) 537 ± 20 MPa (interface, longitudinal) 243 ± 7 MPa (CuCrZr)
Maximum elongation	25.3 ± 3 % (IN718) 8.83 ± 0.6 % (interface, transverse)

	23.3 ± 0.9 % (interface, longitudinal) 18.1 ± 0.7 % (CuCrZr)
Thermal conductivity	12.3 W/m·K (IN718), 31.9 W/m·K (bimetallic), 75.0 W/m·K (bimetallic, heat treated) 104 W/m·K (CuCrZr)

As Table 16 shows, the reported material properties were hardness, ultimate tensile strength of the interface zone, maximum elongation, and thermal conductivity. Hardness was measured from both IN718 and CuCrZr zones, and from the interface zone. Vickers hardness testing method was used with a 0.5-kilogram force. The maximum ultimate tensile strength and maximum elongation were measured from the individual materials and the bimetallic material. The measurements were taken parallel (longitudinal) and perpendicular (transverse) to the interface zone in the bimetallic material. Thermal conductivity was measured from both individual materials. In addition, the thermal conductivity was measured from the bimetallic material before and after heat treatment.

As Table 16 shows, the hardness values were 330 ± 5 $HV_{0.5}$ in IN718, 169 ± 4 $HV_{0.5}$ in the interface region, and 86.0 ± 4 $HV_{0.5}$ in CuCrZr. Maximum ultimate tensile strengths were 1040 ± 12 MPa for IN718, and 243 ± 7 MPa for CuCrZr. The maximum ultimate tensile strength was 190 ± 12 MPa perpendicular, and 537 ± 20 MPa parallel to the interface zone in the bimetallic material. The maximum elongation was 25.3 ± 3 % for IN718, and 18.1 ± 0.7 % for CuCrZr. The maximum elongation for the bimetallic material was 8.83 ± 0.6 % perpendicular to the interface, and 23.3 ± 0.9 % parallel to the interface. Thermal conductivity for IN718 was 12.3 W/m·K and 104 W/m·K for CuCrZr. Thermal conductivity for the bimetallic material was 31.9 W/m·K in the as-manufactured material. Heat treatment increased the value to 75.0 W/m·K.

Vickers hardness tests were conducted individually to the IN718, bimetallic interface, and CuCrZr zones. A visual presentation of the measured values is shown in Figure 14.

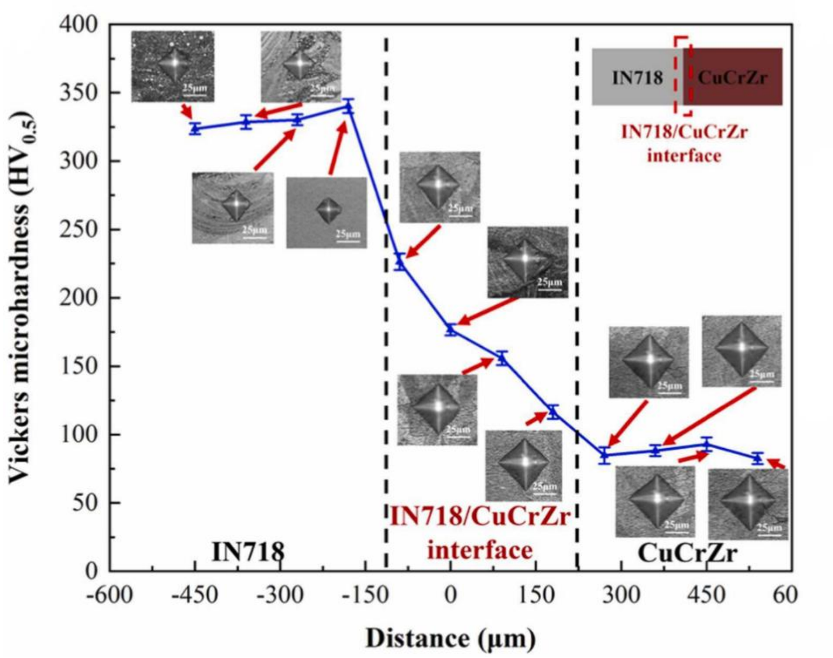

Figure 14 Hardness test result visualisation. Reproduced and modified from Zhang et al., 2024 which is under an open access Creative Common CC BY license.

As Figure 14 shows, the hardness values in the IN718 and CuCrZr zones are consistent regardless of the distance from the interface zone. On the other hand, the values in the interface zone decrease when the measuring points get further from the IN718 and approach the CuCrZr zone. The interface zone measurement taken closest to the IN718 zone, was around 225 $HV_{0.5}$, whereas the measurement taken closest to the CuCrZr zone was around 120 $HV_{0.5}$.

Tensile tests were performed with rods shown in Figure 15. The specimens were manufactured according to the GB/T 228–2002 standard.

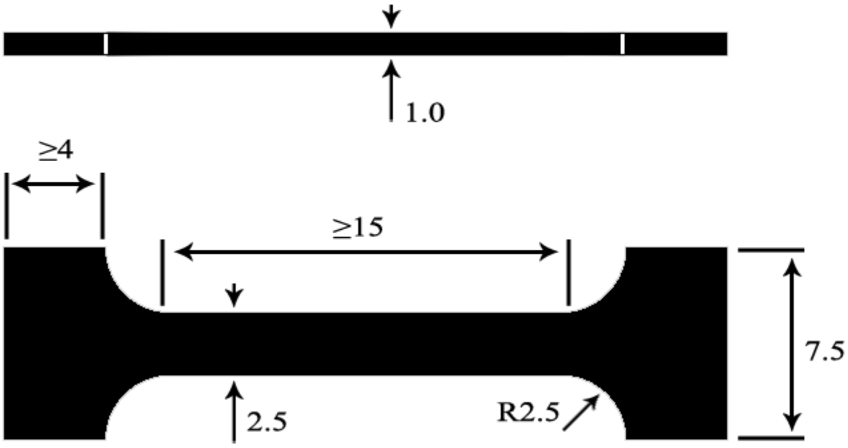

Figure 15 Tensile test sample rod geometry used by Zhang et al., 2024.

As Figure 15 shows, the tensile testing rods have a ≥15 mm long, 2.5 mm thick centre part and 7.5 mm wide ends. The length of the end parts is ≥4 mm. The connection between the centre and ends has a 2.5 mm round radius. The thickness of the rods is 1.0 mm.

Figure 16 shows the ultimate tensile strength test and maximum elongation results by Zhang et al., 2024.

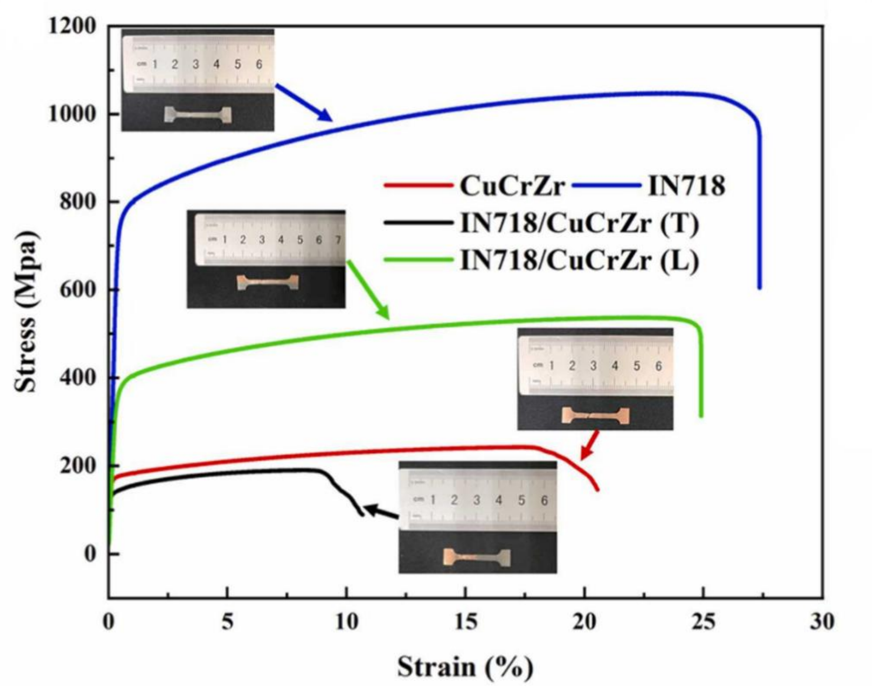

Figure 16 Tensile test results by Zhang et al., 2024.

As Figure 16 shows, the IN718 tensile rod had the highest ultimate tensile strength of 1040 ± 12 MPa, and elongation of 25.3 ± 3 %. The longitudinal interface sample had the second highest ultimate tensile strength of 526 ± 7 MPa, and elongation of 23.3 ± 0.9 %. The CuCrZr rod was found to have the third highest ultimate tensile strength of 243 ± 7 MPa, and elongation of 18.1 ± 7 %. The transverse interface sample was reported to have the lowest ultimate tensile strength of 190 ± 12 MPa, and elongation of 8.83 ± 0.6 %. The transverse interface sample was found to break at the CuCrZr side, and not at the interface zone. Zhang et al., 2024 reported that the difference in results between the transverse and CuCrZr samples can be explained by suboptimal process parameters used in the CuCrZr zone in the transverse interface sample.

6 Aim and purpose of experimental part

The purpose of the experimental part of this thesis is to explore the manufacturing of a bimetallic material of IN718 and CuCrZr using PBF-LB/M, and to study the properties of the manufactured bimetallic material. These properties include porosity, microstructure, thermal conductivity, hardness, and corrosion parameters of the material, as well as the geometrical accuracy of the manufactured samples.

The experimental part of this thesis consists of:

1. Manufacturing a batch of bimetallic samples, referred to as “optimization batch”, to find optimised process parameters for CuCrZr and the bimetallic interface zone.
2. Analysing the manufactured bimetallic samples for porosity and other defects.
3. Manufacturing a batch of bimetallic samples, referred to as “testing batch”, using the optimised process parameters for material characterisation and testing (porosity, microstructure, geometrical accuracy, thermal conductivity, corrosion parameters, and hardness).
4. Performing material characterisation and tests and analysing the results.

The manufacturing phase of this thesis focuses on finding optimised PBF-LB/M process parameters for CuCrZr and the bimetallic interface zone, as the functionality of the process for IN718 has already been proven with the equipment used in this study. Different process parameters for CuCrZr will be used to manufacture a batch of bimetallic material samples. The samples will be analysed for defects and the optimal process parameters will be selected to manufacture a second batch of bimetallic material samples for material characterisation and testing. Porosity and microstructure are analysed with optical microscopy. Geometrical accuracy, corrosion parameters, and hardness are tested and analysed with dedicated equipment. The thermal conductivity is determined through electrical resistance measurements. In addition, the effects of heat treatment on the material properties will be analysed and compared to as-manufactured material.

7 Experimental setup

7.1 Equipment

Equipment used in this thesis are shown in Table 17.

Table 17 Equipment used in the experimental part of this thesis.

Make and model, type	Use	Information
Aconity MIDI+, PBF-LB/M machine	Sample manufacturing	400 W, 1070 nm laser; 316L ø250 mm build plate
Optimum Opti S 290 G, metal band saw	Removal of samples from build plate	With bimetallic saw blade
Struers LaboForce-100, grinding and polishing machine	Grinding and polishing of samples	With sample holder for six samples simultaneously
Motic AE200MET, optical microscope	Optical microscopy of samples	With Rising Tech E3CMOS camera, Rising View 4.12. software
Naber N7, heat treatment oven	Heat treatment of samples	With Naber C8 program controller
Innovatest Falcon 600, hardness tester	Hardness testing of samples	With Innovatest Impressions 3 software
Bruker Alicona InfiniteFocus G6, optical 3D measuring instrument	Geometrical accuracy analysis of samples	With MetMax 3.0. software
Ivium Technologies Vertex, potentiostat	Corrosion parameter testing of samples	With IviumSoft 2.0 software, Gamry counter and reference electrodes
Hioki RM3545, resistance meter	Electrical resistance measurement of samples	With thermometer probe
Dremel Model 300, multi-tool	Cutting samples for electrical resistance testing	With Dremel 420 cutting wheel
Struers Labotom-5, cutting machine	Cutting samples for corrosion parameter testing	With Struers 60A25 cutting wheel

Figure 17 shows the PBF-LB/M machine used in the experimental part of this thesis.

Figure 17 Aconity MIDI+ PBF-LB/M machine.

As Figure 17 shows, the PBF-LB/M machine used to manufacture the samples was an Aconity MIDI+ equipped with a 400 W laser unit. The wavelength of the laser beam was 1070 nm. AconityStudio 3.3.1 software was used for controlling the PBF-LB/M process. The build plate used in the machine was a circular plate made from 316L stainless steel. The diameter and thickness of the build plate were 250 mm and 16.3 mm, respectively. The atmosphere of the build chamber was controlled with argon gas.

Figure 18 shows the metal band saw used in the experimental part of this thesis.

Figure 18 Optimum Opti S 290 G metal band saw.

An Optimum Opti S 290 G metal band saw shown in Figure 18 was used to cut and remove the samples from the build plate using a slow cutting speed. The saw used a bimetallic saw blade suitable for hard materials such as IN718. A custom jig made to hold the Aconity build plate was used to mount the build plate to the bench vice attached to the saw. A cooling liquid was used in the sawing process to cool the blade and samples.

Figure 19 shows the grinding and polishing machine used in the experimental part of this thesis.

Figure 19 Struers LaboForce-100 grinding and polishing machine.

A Struers LaboForce-100 grinding and polishing machine shown in Figure 19 was used to grind and polish the samples for different tests. The machine offered different grinding and polishing methods.

Figure 20 shows the optical microscope used in the experimental part of this thesis.

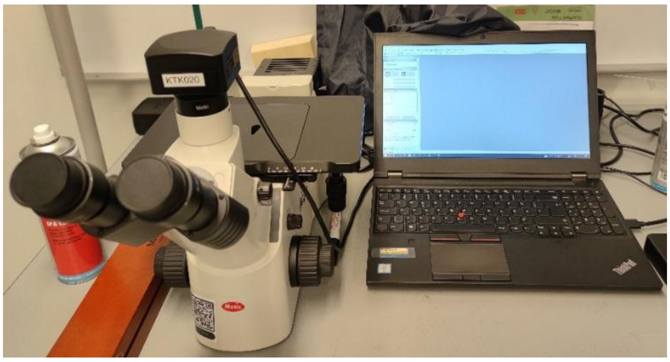

Figure 20 Motic AE200MET optical microscope.

A Motic AE200MET optical microscope shown in Figure 20 was used to analyse the material quality and microstructure of the samples. The microscope was equipped with A Rising Tech E3CMOS camera which allowed direct digital imaging using the Rising View computer software.

Figure 21 shows the heat treatment oven used in the experimental part of this thesis.

Figure 21 Naber N7 heat treatment oven.

A Naber N7 heat treatment oven shown in Figure 21 was used for the heat treatment of the samples. The oven was equipped with a Naber C8 program controller for controlling the heat treatment sequence.

Figure 22 shows the optical 3D measurement instrument used in the experimental part of this thesis.

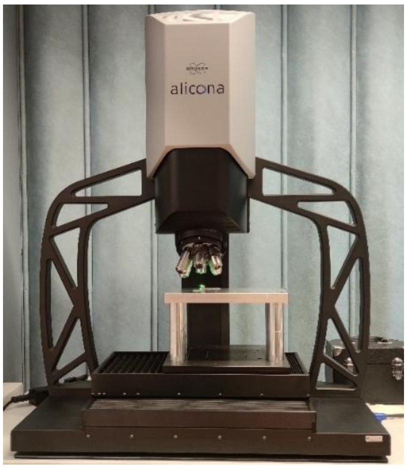

Figure 22 Bruker Alicona InfiniteFocus G6 optical 3D measurement instrument.

A Bruker Alicona InfiniteFocus G6 optical 3D measurement instrument shown in Figure 22 was used for geometrical accuracy measurements. The instrument was equipped with MetMax 3.0. software for measurement analysis.

Figure 23 shows the potentiostat used in the experimental part of this thesis.

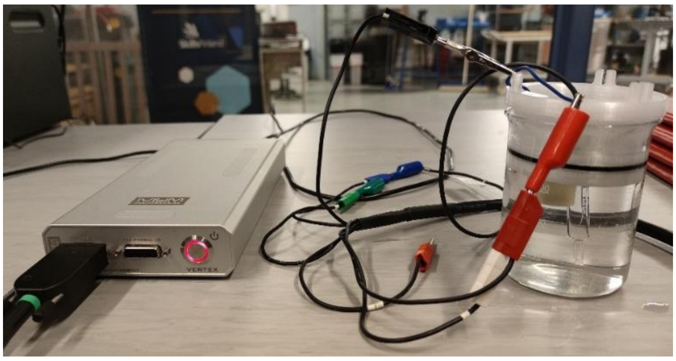

Figure 23 Ivium Technologies Vertex potentiostat.

An Ivium Technologies Vertex potentiostat shown in Figure 23 was used for corrosion parameter tests. The potentiostat was equipped with A Gamry 935-00014 graphite rod counter electrode and a Gamry 1004G Ag/AgCl reference electrode. The electrodes and sample pieces were placed in a glass beaker filled with a 3.5 % NaCl solution. IviumSoft software 2.0 was used for data procurement and analysis.

Figure 24 shows the resistance meter used in the experimental part of this thesis.

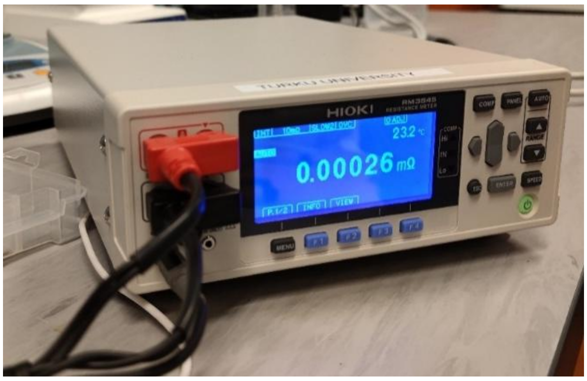

Figure 24 Hioki RM3545 resistance meter.

A Hioki RM3545 resistance meter shown in Figure 24 was used for electrical resistance measurements. The resistance meter was equipped with twin wire leads and connections to sample pieces were made with alligator clamps.

Figure 25 shows the multi-tool used in the experimental part of this thesis.

Figure 25 Dremel model 300 multi-tool.

A Dremel model 300 multi-tool shown in Figure 25 was used for cutting sample pieces for electrical resistance measurements. The multi-tool was equipped with a Dremel 420 cutting wheel.

Figure 26 shows the cutting machine used in the experimental part of this thesis.

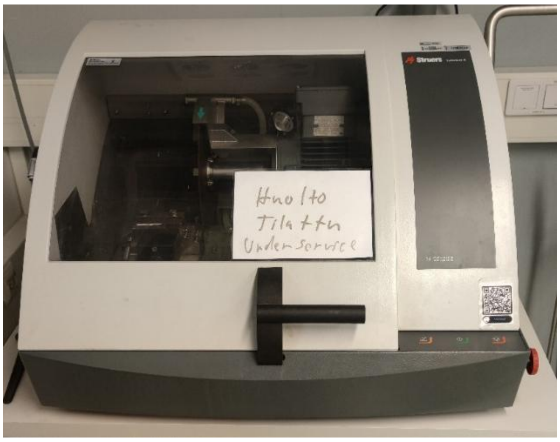

Figure 26 Struers Labotom-5 cutting machine.

A Struers Labotom-5 cutting machine shown in Figure 26 was used for cutting sample pieces for corrosion parameter tests. The cutting machine was equipped with a Struers 60A25 cutting wheel designed for cutting hard materials.

7.2 Software

Other software used in this thesis are shown in Table 18.

Table 18 Other software used in the experimental part of this thesis.

Software	Use
PTC Creo 9.0.1.0	3D modelling of samples
Autodesk Netfabb Premium 2025	Preparing 3D model files for PBF-LB/M

As Table 18 shows, PTC Creo 9.0.1.0 was used for the 3D modelling of all sample geometries. Autodesk Netfabb Premium 2025 was used for the preparation of the 3D models for the PBF-LB/M process. This included the build plate arrangement of the geometries, slicing of geometries into layers, and hatch settings.

7.3 Feedstock powders

The two metal feedstock powders used in this thesis were Nikon SLM Solutions IN718 and EOS Copper Alloy CuCrZr. No additional powder characterization tests were conducted within this study, due to time limitations. Both powders used in the PBF-LB/M process were “virgin”, or previously unused and unhandled powders.

7.3.1 Nikon SLM Solutions IN718

Figure 27 shows an SEM micrograph of the used IN718 metal powder provided in the material data sheet by the manufacturer.

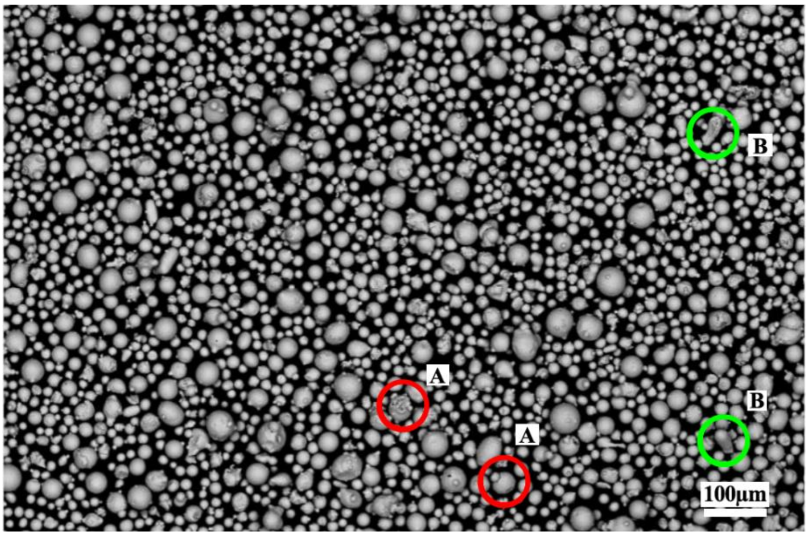

Figure 27 SEM micrograph of Nikon SLM Solutions IN718 powder. (Nikon SLM Solutions Nickel-Based Alloys, n.d.)

As Figure 27 shows, the powder particle shape is spherical with variations in size. The reported particle sizes are between 10 and 45 µm. The SEM micrograph shows satellite particles. Satellite particles are small particles that are attached to larger particles, displayed by circles marked with "A". In addition, some irregular particles are shown by circles marked with "B".

The chemical composition information supplied in the material datasheet of the used IN718 powder by the manufacturer is shown in Table 19.

Table 19 Chemical composition of Nikon SLM Solutions IN718 powder. (Nikon SLM Solutions Nickel-Based Alloys, n.d.)

Element	Fe	Ni	Cr	Ta+Nb	Mo	Ti	Co
Min. wt%	Balance	50.00	17.00	4.75	2.80	0.65	0.00
Max. wt%		55.00	21.00	5.50	3.30	1.15	1.00
Al	Si	Mn	Cu	C	P	S	B
0.20	0.00	0.00	0.00	0.00	0.000	0.000	0.000
0.80	0.35	0.35	0.30	0.08	0.015	0.015	0.006

As Table 19 shows, the main components in the IN718 powder are nickel and chromium. The composition is balanced with iron. Additional elements are present in smaller amounts compared to the main components. The material composition meets the requirements of standards AMS5664, ASTM F3055 and B637. The mass density of the material is around 8.2 g/cm^3. (Nikon SLM Solutions Nickel-Based Alloys, n.d.)

7.3.2 EOS Copper Alloy CuCrZr

Figure 28 shows the SEM micrograph of the used CuCrZr metal powder provided in the material data sheet by the manufacturer.

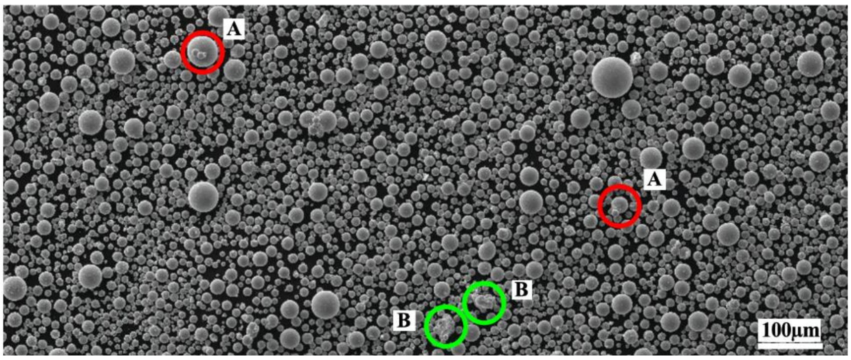

Figure 28 SEM micrograph of EOS CopperAlloy CuCrZr. (*EOS CopperAlloy CuCrZr*, n.d.)

As Figure 28 shows, the powder particle shape is spherical with variations in size. The reported particle sizes are between 15 and 45 µm. The SEM micrograph shows some satellite particles which are displayed by circles marked with “A”. In addition, some irregular particles shown by circles marked with “B”.

The chemical composition information supplied in the material datasheet of the used CuCrZr powder by the manufacturer is shown in Table 20.

Table 20 Chemical composition of EOS Copper Alloy CuCrZr powder. (EOS CopperAlloy CuCrZr, n.d.)

Element	Cu	Cr	Zr	Fe	Si
Min. wt%	Balance	0.45	0.05	0.00	0.00
Max. wt%		1.15	0.25	0.08	0.01

As Table 20 shows, the main component in the CuCrZr powder is copper with additions of other elements. The material composition meets the material composition requirements of designations C18150 and CW106C. (EOS CopperAlloy CuCrZr, n.d.) The mass density of the material was not supplied.

8 Experimental procedure

PBF-LB/M conducted in this thesis consisted of two different phases:

1. The first phase consisted of finding optimal process parameters for CuCrZr and the interface zone to manufacture the bimetallic material of IN718 and CuCrZr.
2. The second phase consisted of manufacturing bimetallic samples for material characterisation and testing based on the process parameters for CuCrZr found in the first phase.

3D models of the samples are shown in Figure 29.

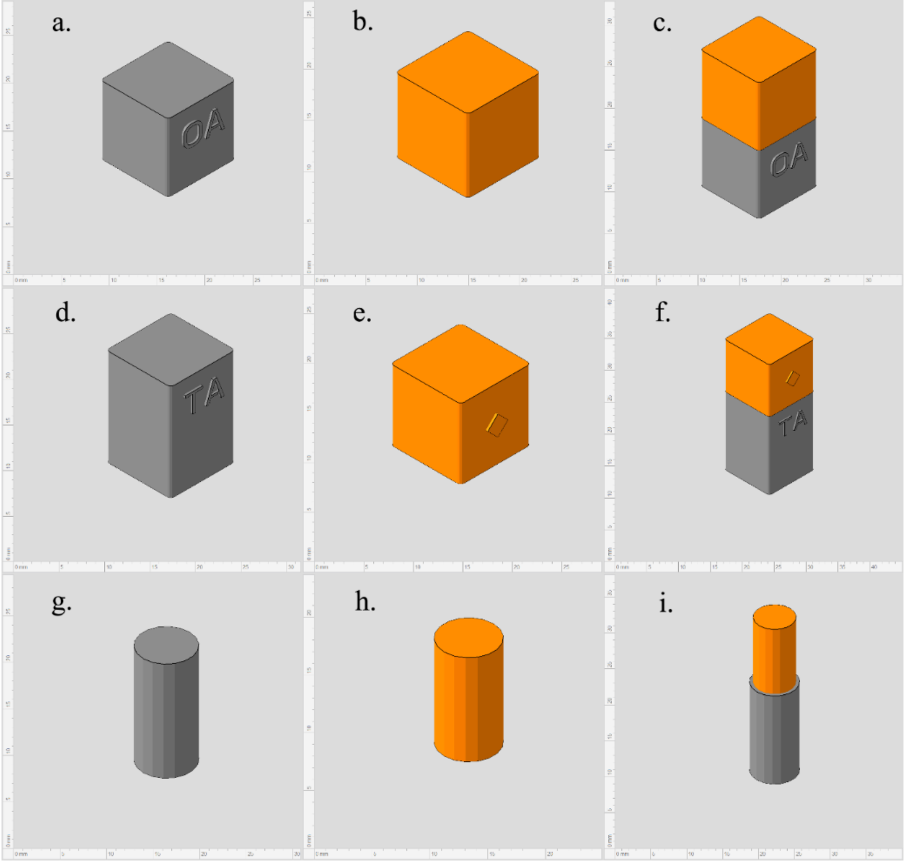

Figure 29 3D models used to manufacture the samples.

As Figure 29 shows, the first batch of samples consisted of twelve 10 x 10 x 20 mm^3 cuboids, presented in Figure 29 c. These cuboids were manufactured using two 10 x 10 x 10 mm^3 cubes built on top of each other from each of the studied materials, IN718 as the bottom material (Figure 29 a) and CuCrZr as the top material (Figure 29 b). The front faces of the bottom parts were marked with a 0.3 mm extruded, sample specific, two-character text code for sample tracking. For the first batch of samples, the letter “O” was used as the first character, shown in Figure 29a. The letter “O” stands for “optimisation batch”. Furthermore, a second character ranging from “A” to “L” in each sample for individual sample identification. The optimisation batch samples were used for exploring different process parameters for CuCrZr manufactured on top of IN718. The process parameters for IN718 were kept constants for all samples on both batches.

The second batch of samples consisted of ten 10 x 10 x 25 mm^3 cuboids (Figure 29 f) and two cylindrical samples (Figure 29 i). The size of the cuboid samples was changed from the first batch as cylindrical samples with a height of 20 mm were required for samples manufactured for dilatometry testing not covered in this thesis. The total height for all cuboid samples was raised from 20 to 25 mm to account for dimensional losses during sample removal from the build plate. The dimensions for the bottom IN718 cuboids were 10 x 10 x 15 mm^3 (Figure 29 d). For the top CuCrZr cubes, the dimensions were kept as 10 x 10 x 10 mm^3 (Figure 29 e). For sample tracking, the first character in the sample specific code was “T”, for “testing batch” and the second characters ranged from “A” to “L”. For the top cubes in the testing batch, a 2 x 2 mm extruded square was added to the centre of the front face of the cube, shown in Figure 29e. This extrusion eliminated any misalignment between the bottom cuboids and top cubes, caused by the text extrusion on the bottom cuboids. The vertical edges of the cube and cuboid samples were rounded with a 0.5 mm radius, shown in Figure 29a-f. The dimensions of the bottom parts of the cylindrical samples were 7 mm x 15 mm (Figure 29 g), and for the top part 6 mm x 11 mm (Figure 29 h). The diameter of the top cylinder was 1 mm less than of the bottom cylinder to avoid overhangs caused by possible misalignment of the build plate in case the build plate had to be removed during the changing of the feedstock powder. In addition, the height of the top cylinder was set as 11 mm to allow for machining of the top face of the manufactured sample.

During the PBF-LB/M process the atmosphere inside the build chamber was controlled and air was replaced with argon gas. The oxygen content of the build chamber was kept at around 100 ppm. The build chamber did not go through any preheating as it was not an option on this specific machine. The sample placement on the build plate, recoater moving direction, and gas flow direction are shown in Figure 30 .

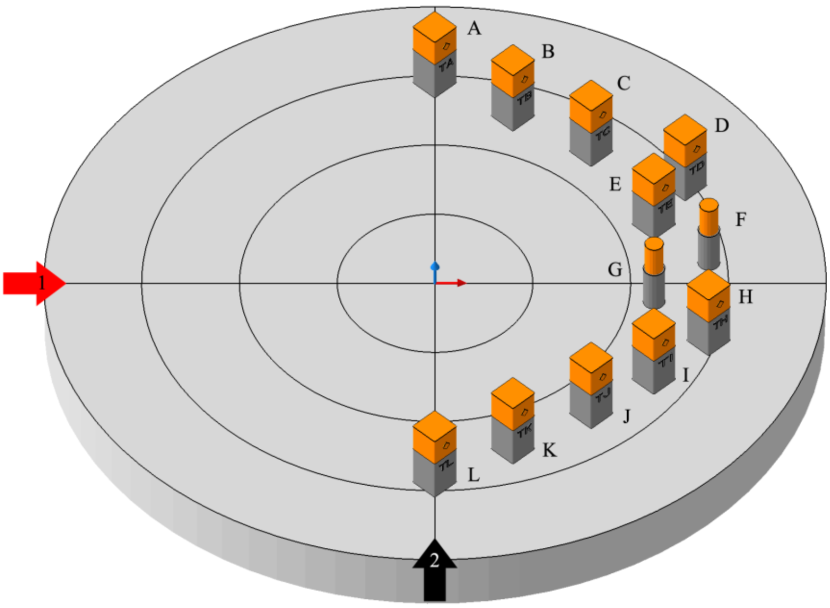

Figure 30 Build plate visualization with locations of testing batch samples.

As Figure 30 shows, all cuboid samples were rotated to a 45-degree angle in relation to the recoater direction to minimize the risk of crashing on any straight sample edges during the recoating phases. The rounding of the vertical edges of the cube and cuboid samples was done for the same reason. Each sample is represented by the individual sample specific lettering ranging from "A" to "L" in Figure 30. The recoater moving direction shown in Figure 30 is from left to right and is marked with the red arrow marked with "1" on the left side of the figure. The recoater returns to the left side of the build plate after each recoating pass. The samples were placed on the build plate in a way that no samples were behind one another during the recoating phases to avoid any inconsistencies in powder delivery. The samples were placed with adequate distance between one another and the build plate edges and securing bolts were avoided. The inert argon gas flow source and direction in Figure 30 is marked with the black arrow marked with "2" at the bottom of the figure.

8.1 PBF-LB/M of IN718 parts

The IN718 parts of the samples were manufactured using the process parameters shown in Table 21.

Table 21 Process parameters used for IN718.

Parameter	Value
Laser power *P*	150 W hatch, 130 W contour
Scanning speed of laser beam *v*	800 mm/s hatch, 1200 mm/s contour
Spot diameter of laser beam	0.08 mm
VED	78.1 J/mm^3
Hatch pattern	Stripe hatch
Hatch distance *h*	0.08 mm
Hatch width	5.00 mm
Hatch rotation increment	67 °
Layer thickness *t*	0.03 mm
Powder supply factor	1.8

As Table 21 shows, the laser power *P* and scanning speeds *v* for IN718 were 150 W and 800 mm/s, respectively. A laser power of 130 W and scanning speed of 800 mm/s was used for the contours of the geometries. The spot diameter of the laser beam was 0.08 mm. The calculated VED value of these process parameters was 78.1 J/mm^3. A stripe hatch was used for the scanning pattern of the laser beam with a 0.08 mm hatch distance. The hatch width was 5.00 mm. With each layer, the hatch pattern was rotated 67 °. Layer thickness was 0.03 mm, and the powder supply factor was 1.8.

These values were kept constant as the functionality of the parameters as well as the quality of results had been proven by earlier use of the Aconity MIDI+ machine with this material. The values were the recommended default values for IN718 from the Aconity process parameter library provided by the machine manufacturer. To enhance and ensure proper material layer adhesion to the build plate, the plate was preheated with three manual laser beam scanning passes according to the sample locations and geometries by using the same process parameters. These process parameters were used for both optimisation, and testing batches.

8.2 PBF-LB/M of CuCrZr parts

Different process parameters were tested for CuCrZr as this exact material had not been used with the Aconity MIDI+ machine before. Compared to the manufacturing of the IN718 parts, an additional remelting phase was added to the PBF-LB/M process in which the previously manufactured layer is remelted with the same process parameters before the addition of a new layer. The top surfaces of the previously built IN718 samples were preheated to enhance the layer adhesion of the first CuCrZr layers with five manual laser scanning passes according to the sample locations and geometries by using the sample specific process parameters.

8.2.1 Optimisation batch

The process parameters were selected based on the recommended default values from the Aconity process parameter library supplied by the machine manufacturer with changes in laser power and scanning speed for different samples. The default values for the laser power and scanning speed were 400 W and 800 mm/s, respectively. A remelting phase, where the previously melted layer is scanned with the laser beam and melted for a second time, was conducted manually to the first five CuCrZr layers on top of the IN718 parts. The process parameters for remelting were the same as the sample specific process parameters. The sample specific process parameters for CuCrZr in the optimisation batch samples are shown in Table 22.

Table 22 Sample specific process parameters used for CuCrZr in the optimisation batch.

Parameter Sample ID	Laser power *P* [W]	Scanning speed *v* [mm/s]	VED [J/mm^3]
A	390	800	135
B	390	750	144
C	390	700	155
D	390	850	127
E	380	800	133
F	380	750	141
G	380	700	151
H	380	850	124
I	370	800	128
J	370	750	137
K	370	700	147
L	370	850	121

As Table 22 shows, the laser power varied between 370 and 390 W, and the scanning speed varied between 700 and 850 mm/s. The calculated sample specific VED values vary between 121 and 155 J/mm^3. The VED value of the Aconity default parameters was 139 J/mm^3.

The process parameters kept constant for CuCrZr in all optimisation batch samples are shown in Table 23.

Table 23 Constant process parameters used for CuCrZr in the optimisation batch.

Parameter	Value
Remelting laser power *P*, scanning speed *v*	Same as sample specific melting parameters
Number of remelted layers	5
Contour laser power *P*, scanning speed *v*	300 W, 1200 mm/s
Spot diameter of laser beam	0.08 mm
Hatch pattern	Stripe hatch
Hatch distance *h*	0.12 mm
Hatch width	6.00 mm
Hatch rotation increment	67 °
Layer thickness *t*	0.03 mm
Powder supply factor	2.0

As Table 23 shows, the remelting laser power and scanning speed were the same as the sample specific melting parameters shown in Table 22. The remelting phase was conducted to the first five CuCrZr layers. A laser power of 300 W and scanning speed of 1200 mm/s was used for the contours of the geometries. The spot diameter was 0.08 mm. A stripe hatch was used for the laser beam scanning pattern with a 0.12 mm hatch distance. The hatch width was 6.00 mm. With each layer, the pattern was rotated 67 °. Layer thickness was 0.03 mm, and the powder supply factor was 2.0.

8.2.2 Testing batch

The process parameters were the same for all twelve samples in the testing batch and were chosen based on material defect analysis of the previously manufactured optimisation batch samples manufactured using parameters shown in Table 22 and Table 23. The parameters selected for manufacturing the testing batch samples for different material characterization tests and analysis are shown in Table 24.

Table 24 Process parameters used for CuCrZr in the testing batch.

Parameter	Value
Melting laser power *P*, scanning speed *v*	390 W, 800 mm/s
Remelting laser power *P*, scanning speed *v*	390 W, 800 mm/s
Number of remelted layers	5
Contour laser power *P*, scanning speed *v*	300 W, 1200 mm/s
Spot diameter of laser beam	0.08 mm

VED	135 J/mm^3
Hatch pattern	Stripe hatch
Hatch distance *h*	0.12 mm
Hatch width	6.00 mm
Hatch rotation increment	67 °
Layer thickness *t*	0.03 mm
Powder supply factor	2.0

As Table 24 shows, the laser power and scanning speeds for CuCrZr were 390 W and 800 mm/s, respectively. The laser power and scanning speeds for the remelting phases were kept the same. The remelting phase was conducted to the first five CuCrZr layers. A laser power of 300 W and scanning speed of 1200 mm/s was used for the contours of the geometries. The spot diameter was 0.08 mm. The calculated VED value of these process parameters was 135 J/mm^3. A stripe hatch was used for the scanning pattern with a 0.12 mm hatch distance. The hatch width was 6.00 mm. With each layer, the pattern was rotated 67 °. Layer thickness was 0.03 mm, and the powder supply factor was 2.0.

8.3 Heat treatment of samples

The heat treatment process was conducted similarly to the process used by Zhang et al., 2024 for the bimetallic material of IN718 and CuCrZr. The three-phased heat treatment plan by Zhang et al., 2024 consisted of the samples being heated to 720 °C with a heating rate of 55 °C/h. The temperature was held at this level for 8 hours. This step was followed by lowering the oven temperature to 620 °C and the samples were held at this temperature for 8 hours. The samples were cooled to room temperature following the heat treatment.

Due to limited features on the used heat treatment oven in this thesis, some changes to the heat treatment process used by Zhang et al., 2024 were made. As the heat treatment oven could only be operated during working hours at the facility, and could not be left unattended at night, the gradual heating by 55 °C/h to 720 °C was not possible. In addition, the target temperatures were changed to 718 °C and 621 °C, according to the AMS 2774 standard. (Gruber et al., 2022)

In addition, the first step by Zhang et al., 2024 was altered by placing the samples in a room temperature oven and heated to 718 °C at the rate the oven heated. The room temperature was 25 °C according to the oven thermometer. The heating sequence took 1 hour and 34 minutes.

The calculated heating rate was 440 °C/h. The samples were held at 718 °C for 8 hours and then air cooled overnight to room temperature.

The second step was similarly altered. The samples were placed in the oven the following morning. The oven temperature at this time was 164 °C. The samples were heated to 621 °C at the rate the oven heated. The heating sequence took 57 minutes. The calculated heating rate was 480 °C/h. The samples were held at 621 °C for 8 hours and air cooled to room temperature.

A variation of ± 2 °C in the temperature was observed as the oven had reached the set temperatures. The oven did not allow for special atmosphere controlling. Figure 31 shows the samples placed on a sample holder used during the heat treatment process.

Figure 31 Samples on heat treatment sample holder.

As Figure 31 shows, the samples were placed on a self-made steel sample holder during the heat treatment process.

8.4 Grinding and polishing of samples

Samples for microstructural and porosity analysis, and hardness tests were grinded and polished. The grinding and polishing sequence steps were based on methods supplied by the equipment manufacturer for low carbon steel and copper as there were no suggested methods for either of the used materials, nor the bimetallic material combination. The grinding and polishing machine is shown in Figure 32.

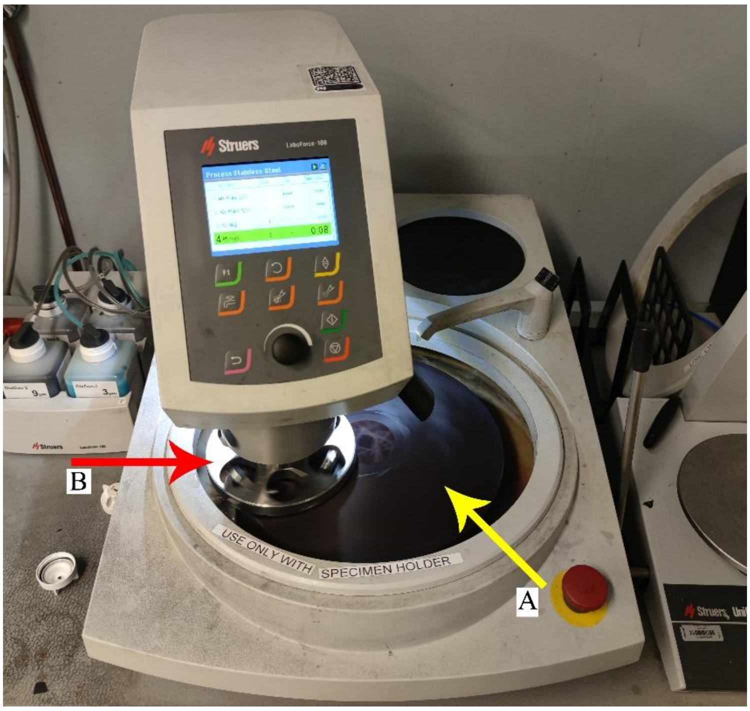

Figure 32 Struers LaboForce-100 grinding and polishing machine.

As Figure 32 shows, the used grinding and polishing machine offers different types of grinding and polishing methods and surfaces. The machine offers the possibility to vary the rotation speed of the work surface and the sample holder separately. The work surface is shown by the arrow marked with “A” and the sample holder by the arrow marked with “B” in Figure 32. The rotation direction of the sample holder can be set to the same or opposite direction as the work surface. The time for each step and the applied force per sample can be varied. The sequence was tested with the optimisation batch samples and adjusted to obtain the best possible mirror finish for the testing batch samples. The grinding and polishing sequence is shown in Table 25.

Table 25 Grinding and polishing sequence for the testing batch samples.

Grinding/polishing consumable type	Grit or solution particle size	Surface rotation speed [rpm]	Sample rotation speed [rpm]	Direction of sample rotation	Step time [min]	Applied force per sample [N]
Struers MD Piano	220#	300	70	Against	4	30
Struers MD Piano	600#	300	70	Same	6	20
Struers MD Piano	1200#	250	50	Against	4	10
Struers MD-Nap	9 µm	100	50	Same	3	10
Struers MD-Nap	3 µm	100	50	Against	3	10
Struers MD-Nap	1 µm	100	50	Same	3	15

As Table 25 shows, Struers MD Piano diamond grinding surfaces were used for the grinding phases from grit 220# to 1200#. Tap water with an even flow was used for lubrication with the grinding surfaces. The surface rotation speed varied between 250 and 300 rpm. The sample holder rotation speed varied between 50 and 70 rpm. The sample holder rotation direction was changed with each step. The time of the grinding steps varied between 4 and 6 minutes. The applied force per sample varied between 10 and 30 N. Struers MD-Nap polishing cloths were used for the polishing phases. Struers DiaDuo-2 diamond polishing solutions were used with particle sizes ranging from 9 to 1 µm. The rotation speed was 100 rpm for the surface and 50 rpm for the sample holder in all polishing steps. The sample holder rotation direction was changed with each step. The time for each step was set as 3 minutes. The applied force per sample varied between 10 and 15 N. Samples were set in Struers VersoCit-2 acrylic compound before the grinding and polishing sequence.

Figure 33 shows a sample set in the acrylic compound.

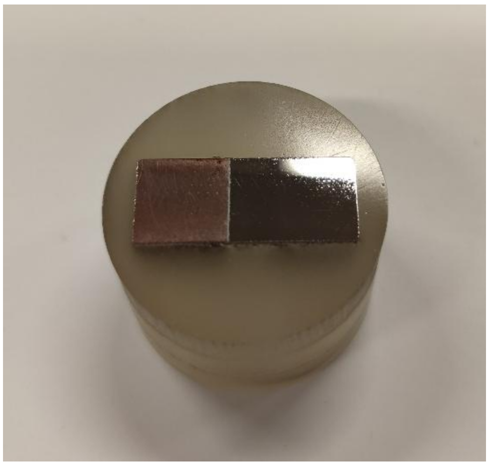

Figure 33 Sample set in acrylic compound.

As Figure 33 shows, the samples were set in ø 30 mm molds using Struers VersoCit-2 acrylic compound. The exposed surface of the molded part was used for different material characterization tests.

8.5 Etching of samples

Samples for microstructural analysis were etched with a self-mixed etching solution. The etching solution consisted of 3 g of iron(III) chloride ($FeCl_3$), 2 ml of hydrochloric acid (HCl), and 98 ml of purified water (H_2O). The $FeCl_3$ was supplied by Thermo Scientific in powder form. The concentration of the powder was 98 %. The HCl was supplied by VWR Chemicals in liquid form. The concentration of the liquid was 30 %. The used purified water was battery water supplied by Würth. Samples were etched for 3 seconds, followed by rinsing with tap water. Figure 34 shows the samples after the etching process.

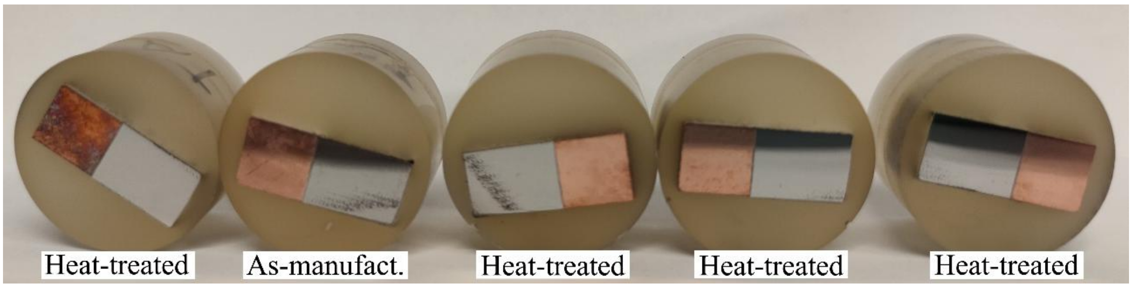

Figure 34 Samples after the etching process.

As Figure 34 shows, the CuCrZr parts appear dull after the etching process. The IN718 parts show no visible change with this etching process time as IN718 requires a longer etching time than CuCrZr.

8.6 Metallographic analysis

Metallographic analysis was conducted using an optical microscope. The microscope was equipped with a digital camera connected to a computer allowing for real-time image analysis and micrograph saving. The equipment was used to analyse porosity and microstructure in the individual materials and the bimetallic interface zone.

Porosity analysis of the micrographs was conducted with a self-made code for detecting porosity levels in addition to a visual inspection. The code allowed for the adjustment of the porosity detecting threshold. Any scratches left from the un-optimised grinding and polishing sequence were ignored in the porosity analysis.

8.7 Geometrical accuracy analysis

Geometrical accuracy measurements were taken from an as-manufactured sample and a heat-treated sample. Seven different measurements were taken from each sample. The measurement scanning tracks are shown in Figure 35.

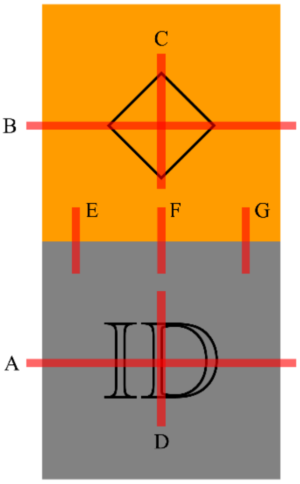

Figure 35 Geometrical accuracy measurement scan tracks and locations.

As Figure 35 shows, scan tracks “A” and “B” were used to measure the width of the samples at the IN718 and CuCrZr parts. Scan tracks “C” and “D” were used to measure the square and sample ID extrusions. Scan tracks “E”, “F”, and “G” were used to measure the offset between the IN718 and CuCrZr parts on the interface zone.

8.8 Thermal conductivity tests

The thermal conductivity of as-manufactured and heat-treated IN718, CuCrZr, and the bimetallic material combination was determined by the measured electrical resistance values for each material.

Figure 36 shows the sample pieces cut for electrical resistance measurements.

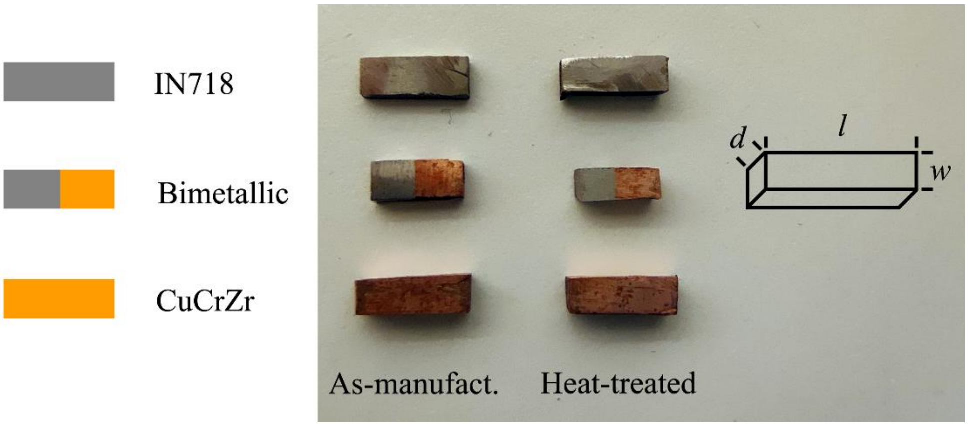

Figure 36 Sample pieces cut for electrical resistance measurements.

As Figure 36 shows, an as-manufactured sample and a heat-treated sample were cut into three pieces consisting of IN718, the bimetallic material, and CuCrZr. As indicated in Figure 36, the sample piece length is represented by *l*, depth by *d*, and width by *w*.

The measured electrical resistance R [Ω] can be used to calculate the electrical resistivity ρ [Ω·m] and thermal conductivity λ [W·mK] of each sample piece. Figure 37 shows the setup used for electrical resistance measurements.

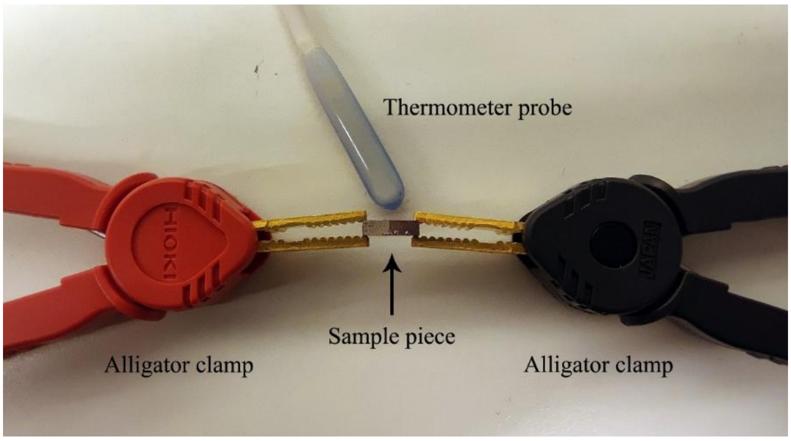

Figure 37 Electrical resistance measurement setup.

As Figure 37 shows, each sample piece was tested separately. Test leads were connected to each end of the sample piece using alligator clamps. The ambient temperature while performing the tests was 23.0 °C. The sample pieces were handled with pliers to avoid changes in the temperature of the pieces. The four point measurement test leads were connected to the resistance meter with two wires each. Each sample piece underwent measurements five times with the test leads replaced in different locations each time. The distance *D* between the contact points of the alligator clamps was measured with each measurement.

Electrical resistivity ρ can be calculated using the measured electrical resistance R for each sample piece. The formula for calculating the electrical resistivity ρ is shown in Equation (1) below. (Lowrie & Fichtner, 2020)

$$\rho = R\frac{A}{l} \tag{1}$$

In Equation (1), ρ is electrical resistivity, R is resistance, A is the cross-sectional area of the sample piece, and l is the length of the sample piece.

The Wiedemann-Franz law was used to calculate the thermal conductivities of the sample pieces. The formula is shown in Equation (2) below. (Tang, Chen, Sun, Li, et al., 2022)

$$\lambda = LT\sigma \tag{2}$$

In Equation (2), λ is thermal conductivity, L is the Lorenz number, σ [S/m] is the electrical conductivity, and T [K] is temperature. The Lorenz number is a constant value of $2.41 \cdot 10^{-8}$ $\Omega \cdot \mathrm{WK}^{-2}$. (Tang, Chen, Sun, Li, et al., 2022)

Electrical conductivity σ is the reciprocal of electrical resistivity ρ. The formula for electrical conductivity σ is shown in Equation (3) below. (Tang, Chen, Sun, Li, et al., 2022)

$$\sigma = \frac{1}{\rho} \tag{3}$$

In Equation (3), σ is electrical conductivity and ρ is electrical resistivity.

Equation (2) can be modified by substituting electrical conductivity σ with electrical resistivity ρ. The modified formula is shown in Equation (4) below.

$$\lambda = \frac{LT}{\rho} \tag{4}$$

In Equation (4), λ is thermal conductivity, L is the Lorenz number, T is temperature, and ρ is electrical resistivity.

8.9 Corrosion parameter tests

An as-manufactured sample and a heat-treated sample were prepared for corrosion parameter tests by cutting a piece of IN718, CuCrZr, and the bimetallic material from both samples. Figure 38 shows the sample pieces prepared for corrosion parameter tests.

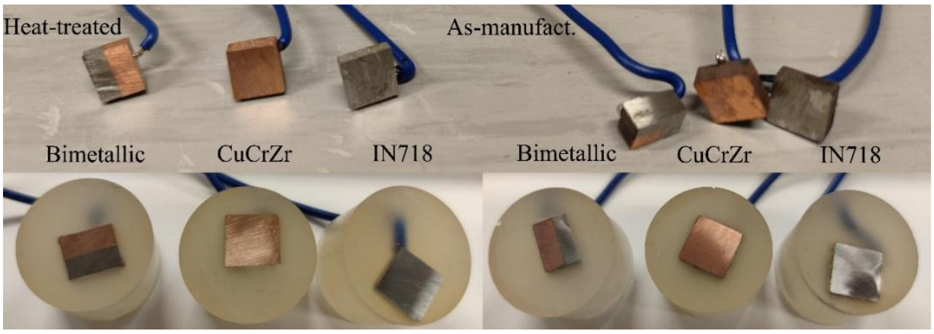

Figure 38 Prepared sample pieces for corrosion parameter tests.

As Figure 38 shows, copper wires were soldered to the backsides of the sample pieces, and the pieces were set in Struers VersoCit-2 acrylic compound. A single surface was exposed from the acrylic compound. The exposed surface was grinded with Struers SiC foil sanding paper with a grit of 1200#.

The sample piece specifications are shown in Table 26.

Table 26 Specifications for sample pieces used for corrosion parameter tests.

Sample	Material	Exposed surface area of piece	Thickness of piece
As-manufact.	IN718	88.8 mm^2	3.15 mm
As-manufact.	CuCrZr	86.0 mm^2	4.15 mm
As-manufact.	IN718/CuCrZr	85.0 mm^2 (46.0/39.0 mm^2)	4.35 mm
Heat-treated	IN718	100 mm^2	3.90 mm
Heat-treated	CuCrZr	100 mm^2	4.40 mm
Heat-treated	IN718/CuCrZr	70.0 mm^2 (40.0/30.0 mm$^{2)}$	5.30 mm

As Table 26 shows, corrosion parameter tests were conducted to an as-manufactured sample and a heat-treated sample. The exposed surface area of the as-manufactured IN718 sample piece was 88.8 mm^2. The thickness was 3.15 mm. The exposed surface area of the as-manufactured CuCrZr sample piece was 86.0 mm^2. The thickness was 4.15 mm. The exposed area for the as-manufactured bimetallic sample piece was 85.0 mm^2, of which 46.0 mm^2 was IN718 and 39.0 mm^2 was CuCrZr. The thickness of the sample piece was 4.35 mm.

The exposed surface area for the heat-treated IN718 and CuCrZr sample pieces were 100 mm^2 each. The thickness of the IN718 and CuCrZr sample pieces were 3.90 mm and 4.40 mm, respectively. The exposed surface area for the heat-treated bimetallic sample piece was 70.0 mm^2, of which 40.0 mm^2 was IN718 and 30.0 mm^2 CuCrZr. The thickness of the sample piece was 5.30 mm. The variations in the sample piece dimensions were caused by the manual cutting of the samples.

The measurements were taken with a vernier calliper.

Two different corrosion parameter test types were performed. The sample pieces were tested with open circuit potential (OCP) and Tafel extrapolation methods. The test setups are shown in Figure 39.

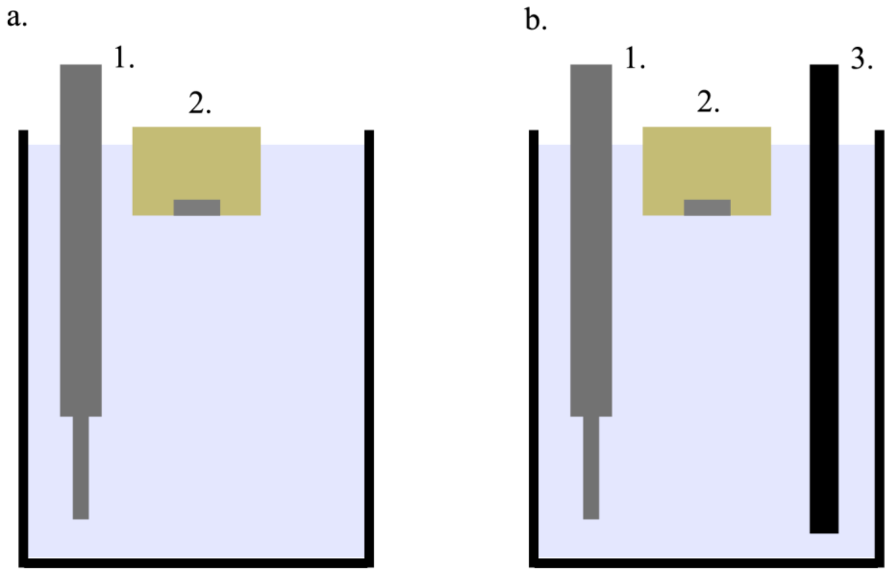

Figure 39 Corrosion parameter test setups used in this thesis.

As Figure 39 shows, the two different tests require different setups. Figure 39a shows the setup for the OCP method and Figure 39b the setup for the Tafel extrapolation method. In Figure 39 the used Ag/AgCl reference electrode is marked with “1”. The sample piece set in acrylic compound is marked with “2”. “3” represents the graphite counter electrode in Figure 39b.

In both setups, the sample pieces, reference electrode, and the counter electrode were placed in a glass beaker filled with 3.5 % NaCl solution. The sample pieces, reference electrode, and counter electrode were connected to a potentiostat using electrical wires. The test time used in the OCP method was 60 minutes. A 10-minute OCP method test preceded the Tafel extrapolation method tests.

Figure 40 shows a Tafel extrapolation curve schematic.

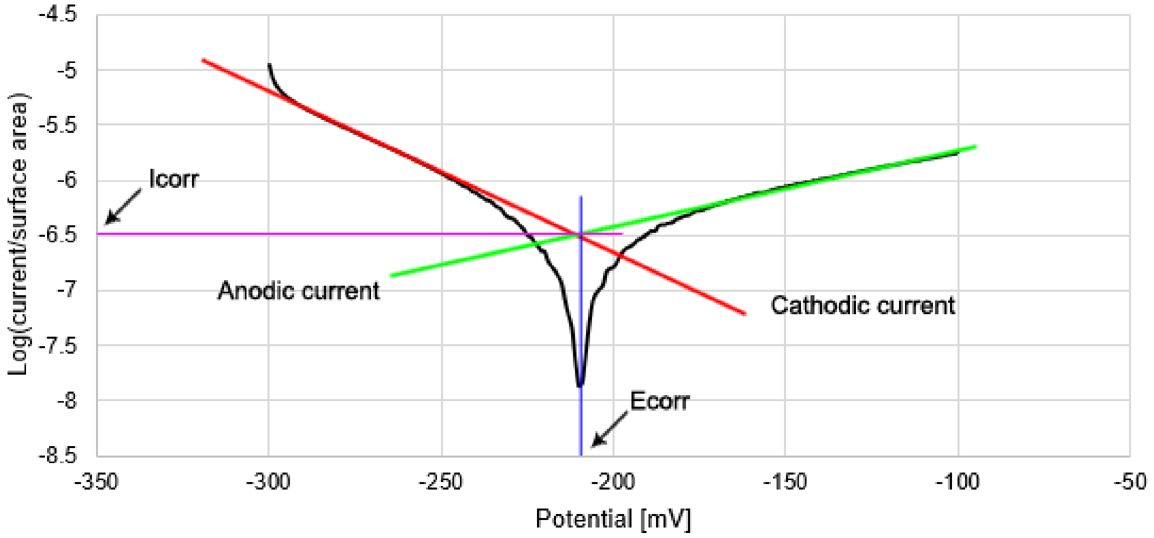

Figure 40 Tafel extrapolation schematic.

As Figure 40 shows, the anodic and cathodic currents are represented by green and red lines, respectively. The corrosion potential (E_{corr}) is found on the X-axis, and the corrosion current density (I_{corr}) on the Y-axis, relative to the intersection of the current lines.

8.10 Hardness tests

Hardness tests were conducted to an as-manufactured sample and four heat-treated samples. The Vickers method was used with a 0.5-kilogram force and a 10 second dwell time. A visualisation of the scan tracks is shown in Figure 41.

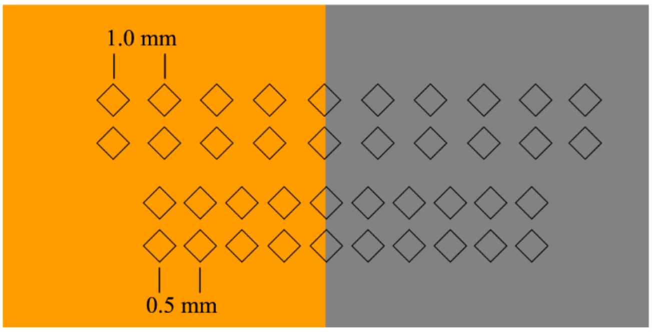

Figure 41 Hardness test measurement point track visualisation.

As Figure 41 shows, four separate tracks were scanned on each sample. A 1.0 mm and a 0.5 mm distance between measurement points was used for two scan tracks, respectively. Each scan track consisted of 10 measurement points. The distance of each point was measured from the interface.

9 Results and discussion

9.1 Porosity analysis of optimisation batch

The optimisation batch samples were analysed for porosity and other defects in the CuCrZr and interface zones. Figure 42 shows optical micrographs of the samples.

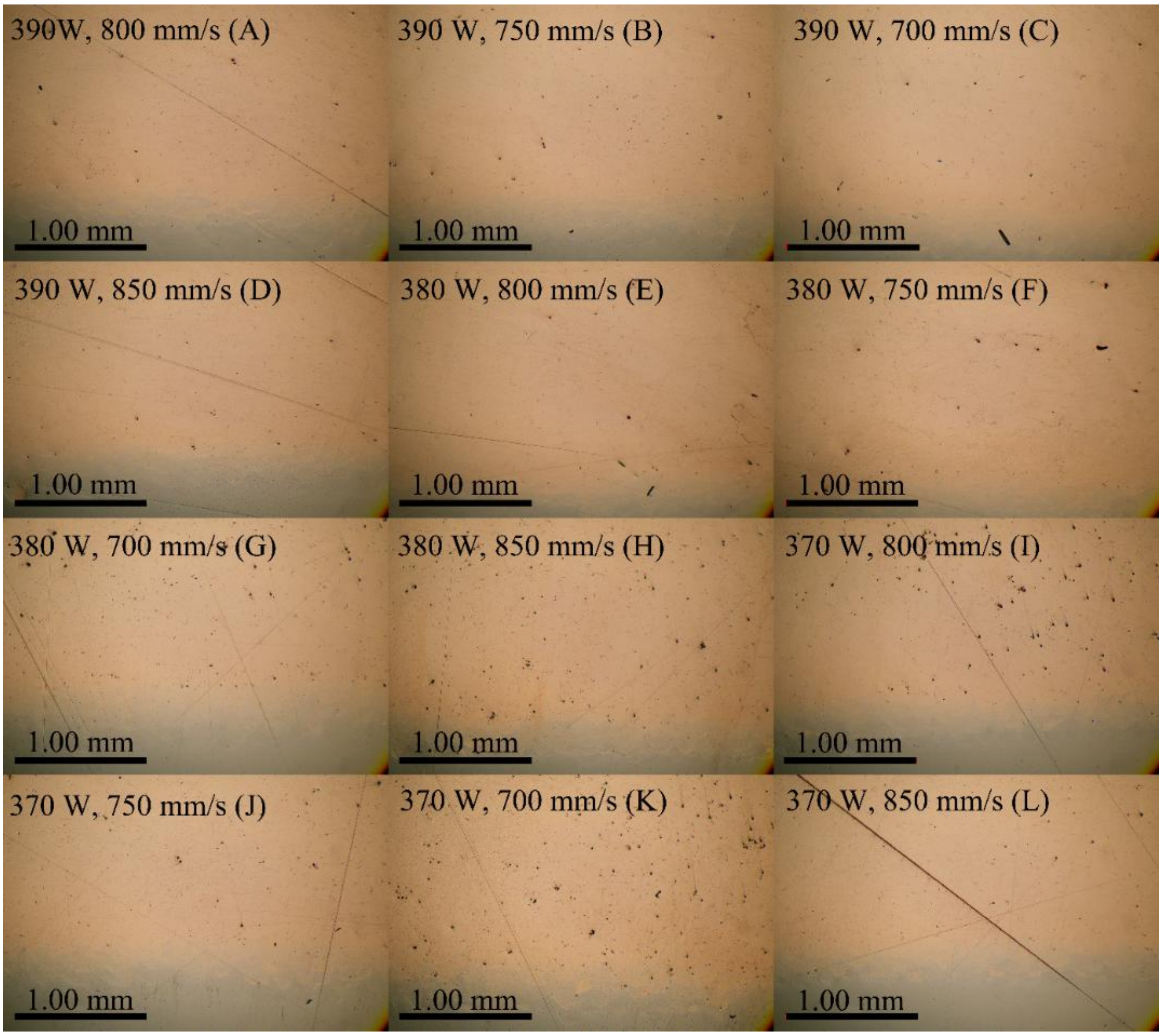

Figure 42 Micrographs of porosity in optimisation batch samples.

As Figure 42 shows, all samples show porosity.

Samples “A” and “B” showed the least amount of porosity in CuCrZr and the interface zone. This suggests that using process parameters close to the values recommended by the PBF-LB/M machine manufacturer result in the least number of defects in the manufactured materials.

Samples “C”, “D”, and “E” showed more porosity and larger pore size compared to “A” and “B”. In addition, the interface zone was noticed to contain more pores. Samples “F” to “K” showed high levels of porosity. This suggests that deviating the process parameters from the recommended values result in an increased number of defects in the materials.

Sample “L” showed porosity similar samples “A” and “B” but was observed to contain defects in the interface zone, shown in Figure 43.

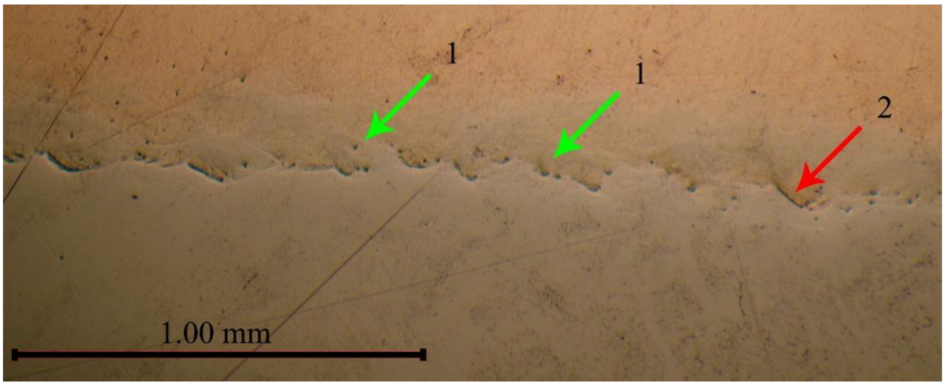

Figure 43 Interface defects in sample “L”.

As Figure 43 shows, porosity and lack of fusion was present in the interface zone of sample “L”. Porosity is showed by arrows marked with “1”, and lack of fusion with an arrow marked with “2”. The process parameters used in the sample manufacturing were 370 W for laser power and 850 mm/s for scanning speed. This shows that lowering the laser power *P* and increasing the scanning speed *v* from the recommended values of 400 W and 800 mm/s increase the number of defects especially in the interface zone of IN718 and CuCrZr.

It can be concluded from these results that lowering the laser power *P* from the recommended value results in an increased number of defects.

An additional comparison between the “A” and “B” was conducted. Two images from each sample were selected for closer analysis. Figure 44 shows the four overlapped images.

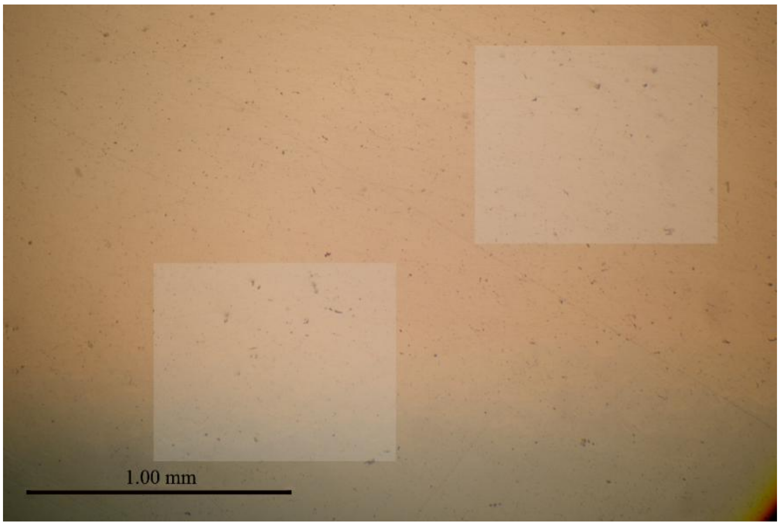

Figure 44 Images from samples "A" and "B" overlapped.

As Figure 44 shows, two smaller areas were selected for comparing the two samples. The areas are marked with white rectangles. The sizes of the rectangles are around 0.9 x 0.7 mm. The first area was selected on the CuCrZr side avoiding any scratches left by the un-optimised grinding process. The second area was chosen with the same criteria but included the interface zone. Figure 45 shows grayscale images of the selected areas.

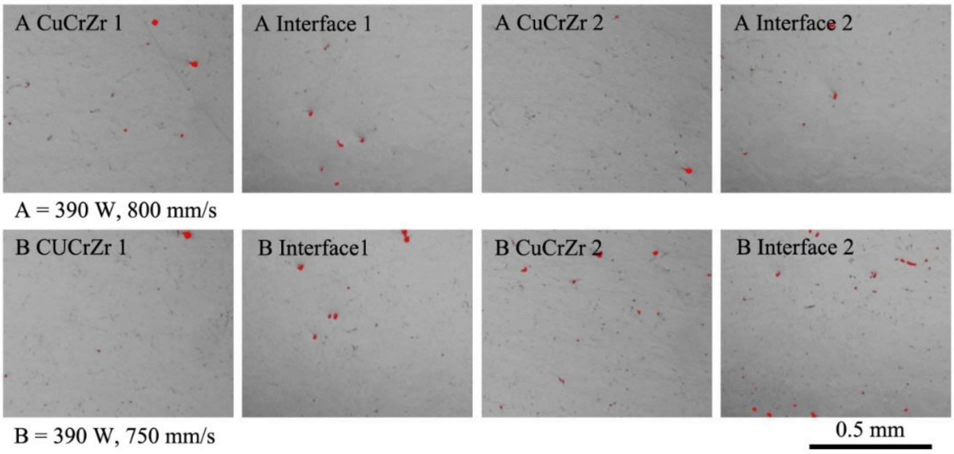

Figure 45 Samples "A" and "B" grayscale images from selected areas.

As Figure 45 shows, the self-made code turned the optical micrographs into grayscale images and marked pores with red. The porosity threshold was adjustable. The porosity levels were 0.05 % and 0.08 % for “A” and “B”, respectively with a threshold of 80. With a threshold of 90 the values were 0.06 % and 0.11 %, respectively. With a threshold of 100 the values were

0.08 % and 0.14 %, respectively. The grayscale images in Figure 45 used a threshold of 100. The process parameters used to manufacture sample “A” were chosen for the testing batch, as it showed the least porosity in the individual materials as well as the interface zone with all thresholds. These results conclude that using process parameters closest to the values recommended by the PBF-LB/M machine manufacturer result in the least number of defects in the manufactured material.

9.2 Visual inspection

9.2.1 Optimisation batch

Figure 46 shows the manufactured optimisation batch samples on the build plate.

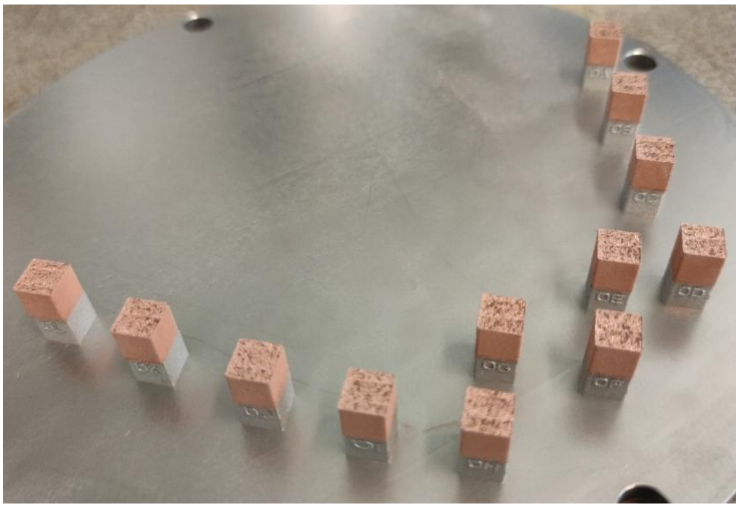

Figure 46 Manufactured optimisation batch samples on the build plate.

As Figure 46 shows, the manufactured samples consist of an IN718 bottom part and a CuCrZr top part. There are no significant visible defects on the samples, and all manufacturing processes have finished without interruptions. This shows that altering the process parameters from the recommended values to a certain point does not result in failures in the manufacturing process. A misalignment can be seen above the sample specific identification codes between the IN718 and CuCrZr in all samples. This was caused by the differences in the centre points between the top and bottom 3D models as the identification code extrusion changes the centre point of the bottom part. This was rectified in the testing batch geometries with an extruded square on the top part 3D model.

The main conclusion from the visual inspection of the samples manufactured in the optimisation batch was that the different process parameters can be used in the manufacturing process and that there are no visible differences at this level of inspection.

9.2.2 Testing batch

Figure 47 shows the manufactured testing batch samples on the build plate.

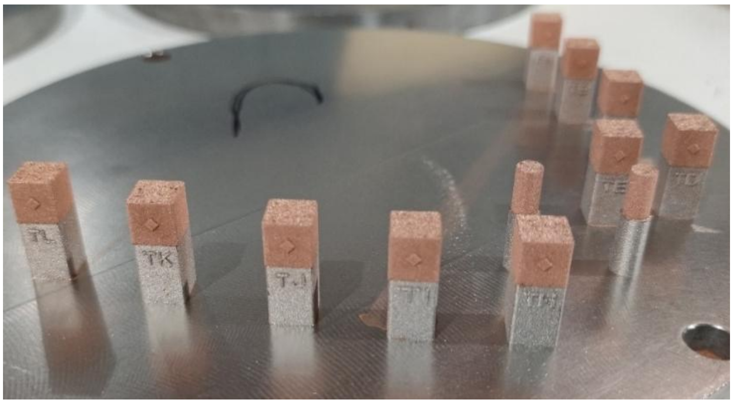

Figure 47 Manufactured testing batch samples on the build plate.

As Figure 47 shows, the manufactured samples consist of an IN718 bottom part and a CuCrZr top part. There are no significant visible defects on the samples, and all build processes have finished without interruptions. The misalignment between the IN718 bottom and CuCrZr top parts was removed with the added square extrusion in the top part 3D model. It can be concluded that the selected process parameters can be used to manufacture bimetallic material of IN718 and CuCrZr.

Figure 48 shows the testing batch samples after removal from the build plate.

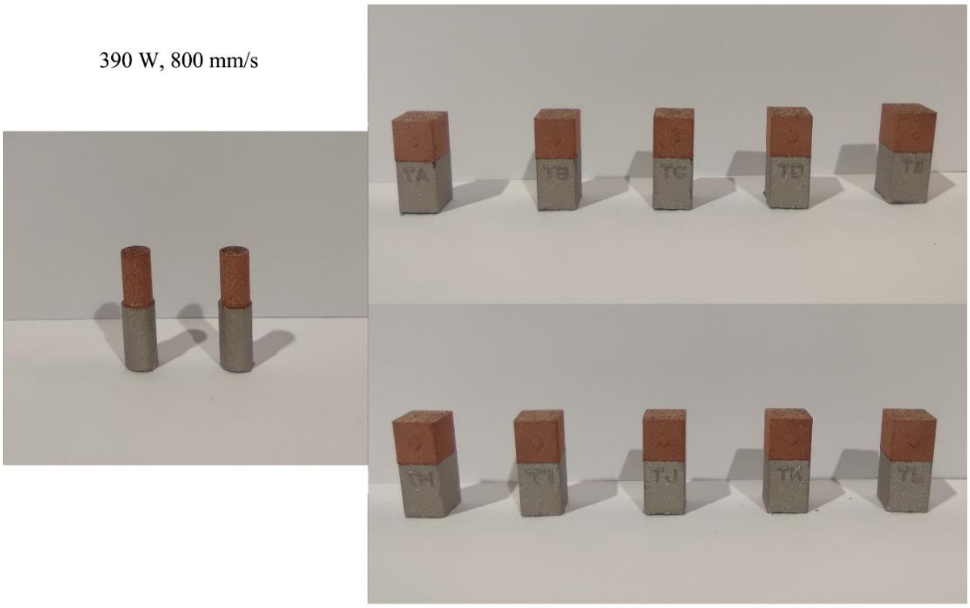

Figure 48 Testing batch samples removed from the build plate.

As Figure 48 shows, all samples were removed from the build plate for conducting different material characterization tests.

A colour difference was observed in the samples after heat treatment, as shown in Figure 49.

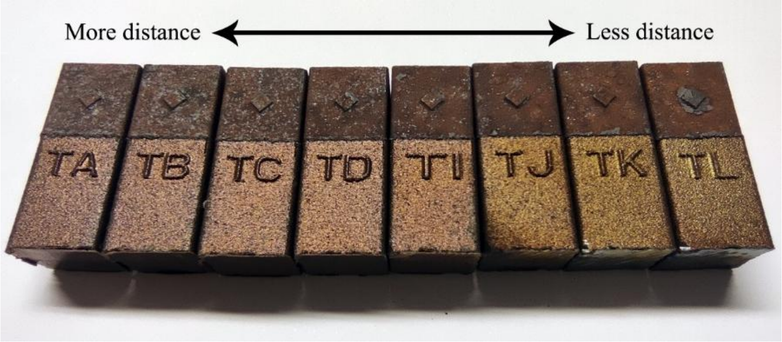

Figure 49 Colour differences in samples after heat treatment.

As Figure 49 shows, a colour difference was observed between the heat-treated samples. The colour was noticed to change depending on the sample location on the build plate. This was suspected to be caused by the cooling effect of the argon shield gas used by the PBF-LB/M machine. Sample on the left had the most distance from the shield gas source and sample on the right was located closest to the source in Figure 49. The heat-treated samples were observed to oxidize during the heat treatment process as the oven did not offer atmosphere controlling.

Scaling was observed on the CuCrZr parts and was mostly removed with a brush. The change in colour was observed on both IN718 and CuCrZr parts. Heat treatment was not observed to cause any visible defects to the samples which suggests that the used heat treatment process is compatible with the bimetallic material combination of IN718 and CuCrZr.

9.3 Porosity

Porosity analysis was conducted to an as-manufactured sample and four heat-treated samples. Samples for the analysis were selected based on their respective locations on the build plate during the manufacturing process. Analysis was conducted individually to IN718, CuCrZr, and the bimetallic interface zone.

Figure 50 shows the micrographs of the as-manufactured and heat-treated IN718.

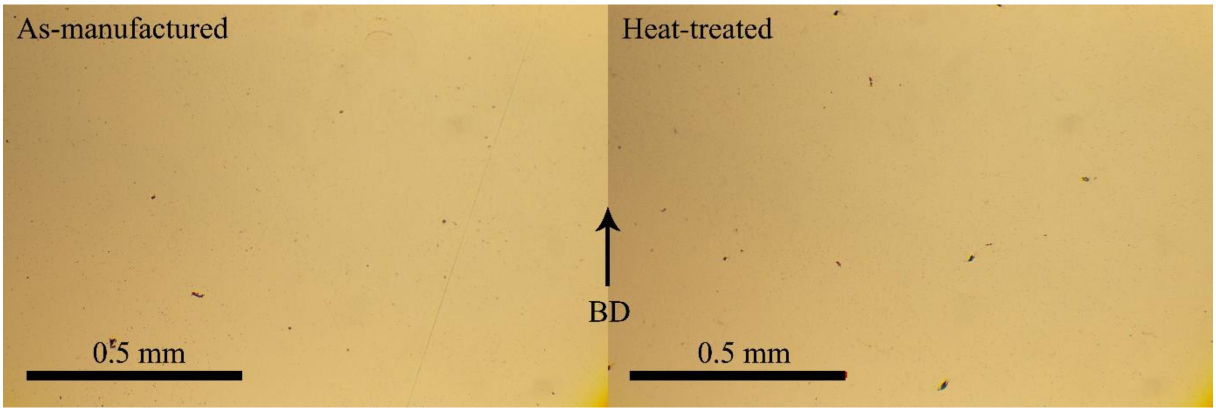

Figure 50 Micrographs of porosity in IN718.

As Figure 50 shows, no visible differences are observed in IN718 before and after heat treatment. “BD” indicates the building direction of the material. The average porosity in the as-manufactured material was 0.37 %. The average porosity in the heat-treated material was 0.16 %. The difference in the porosity values was caused by localized pores in individual micrographs taken from the as-manufactured sample.

Figure 51 shows the micrographs of the as-manufactured and heat-treated CuCrZr.

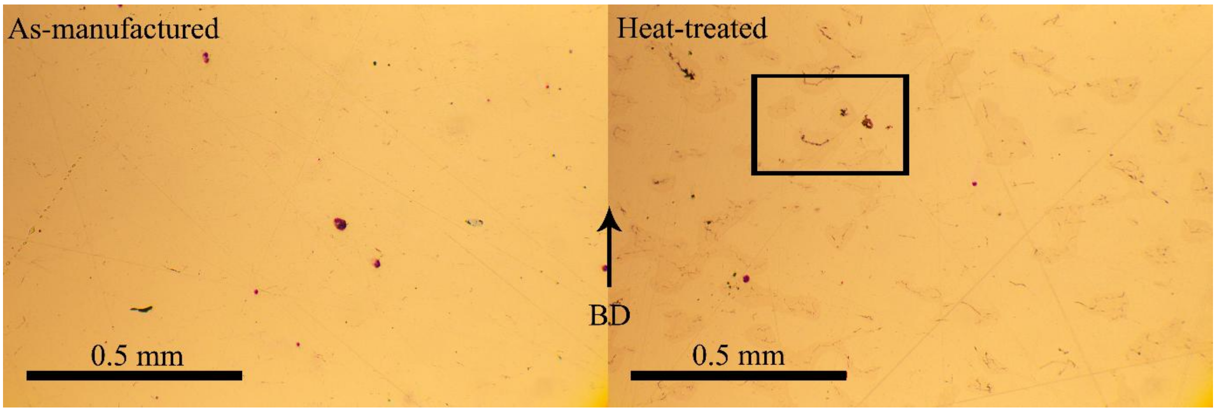

Figure 51 Micrographs of porosity in CuCrZr.

As Figure 51 shows, the heat treatment caused visible differences in CuCrZr. “BD” indicates the building direction of the material. Microcracks were observed, surrounded by darker areas. The average porosity in the as-manufactured material was 0.67 %. The average porosity in the heat-treated material was 0.85 %. The increase in the porosity values after heat treatment were suspected to be caused by the formation of microcracks in the material. The area inside the black rectangle is presented as in close in Figure 52.

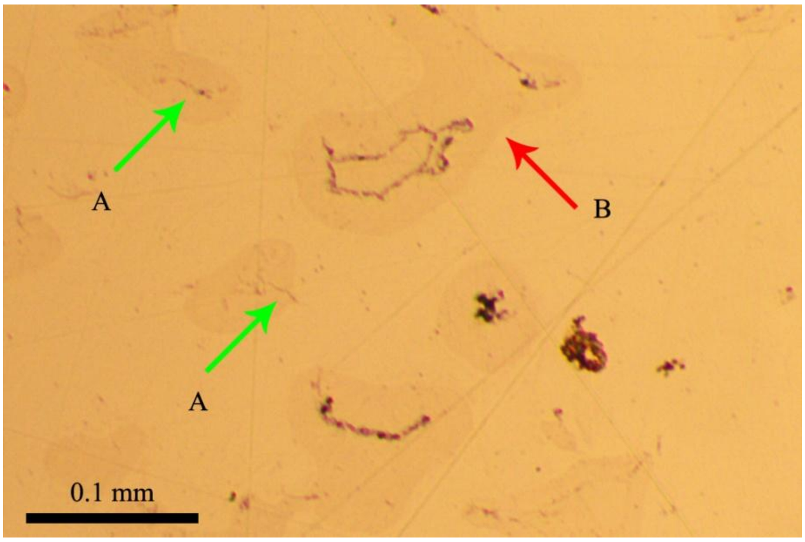

Figure 52 Microcracks and darker areas in CuCrZr.

As Figure 52 shows, microcracks are visible after heat-treatment, represented by arrows marked by “A”. The microcracks are surrounded by darker areas in the material, represented by the arrow marked with “B”. The defects are suspected to have been caused by the rapid heating rate during the heat treatment process which was based on the heat treatment process of IN718.

Figure 53 shows the micrographs of as-manufactured and heat-treated bimetallic interface zones of IN718 and CuCrZr.

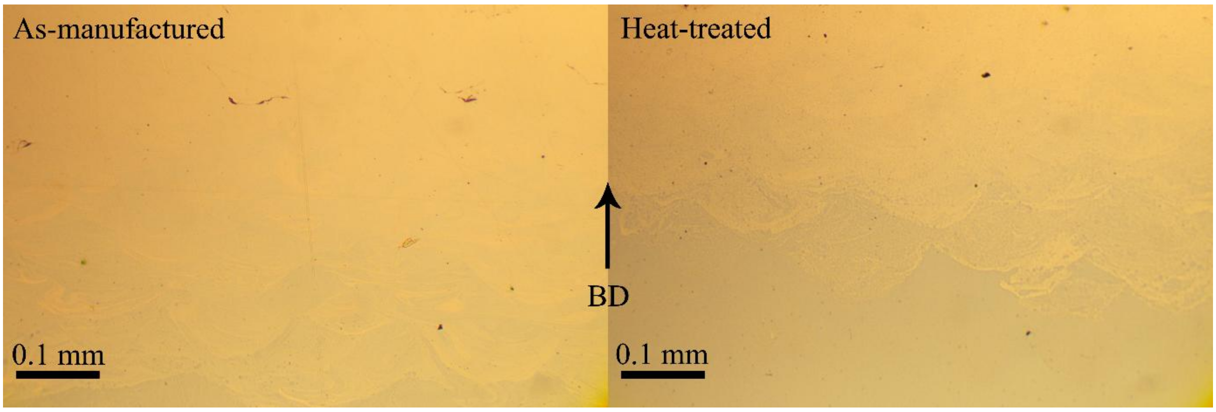

Figure 53 Micrographs of porosity in the bimetallic interface zone.

As Figure 53 shows, no significant differences were observed in the interface zone before and after heat treatment. “BD” indicates the building direction of the material. The average porosity in the as-manufactured material was 0.77 %. The average porosity in the heat-treated material was 0.24 %. The difference in the porosity values was observed to have been caused by localized pores in individual micrographs taken from the as-manufactured sample.

No significant differences in porosity values in the materials were observed based on the respective build plate locations of the samples.

9.4 Microstructure

The microstructures of the CuCrZr and bimetallic interface zone were analysed with a microscope after etching the as-manufactured and heat-treated materials. IN718 was not analysed, as no noticeable difference in the material surface was observed after the etching process as the etching times for CuCrZr and IN718 are different.

Figure 54 shows the microstructure of as-manufactured and heat-treated CuCrZr.

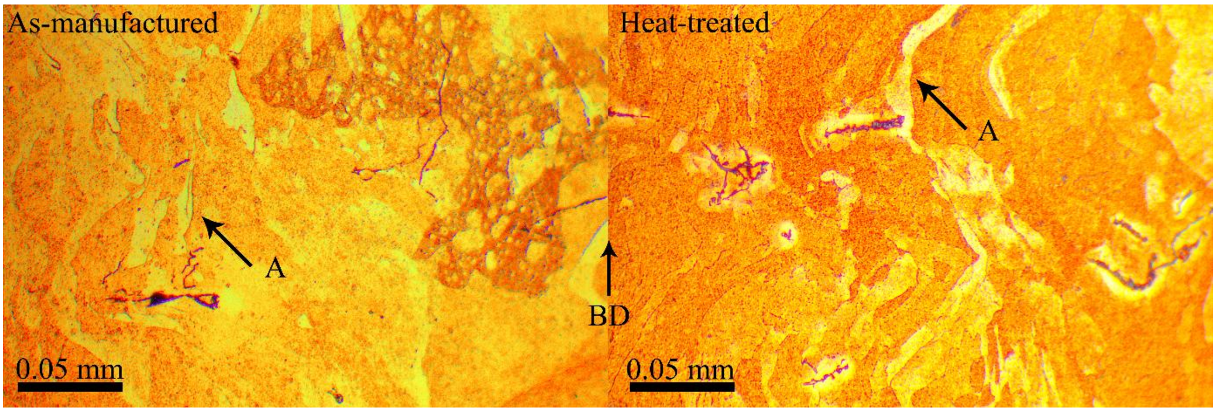

Figure 54 Microstructure of CuCrZr.

As Figure 54 shows, CuCrZr consists of columnar crystals, indicated by arrows marked with "A". "BD" represents the building direction of the material in Figure 54. The formation of the columnar crystals is parallel to the building direction.

Figure 55 shows the microstructure of the as-manufactured and heat-treated bimetallic interface zones.

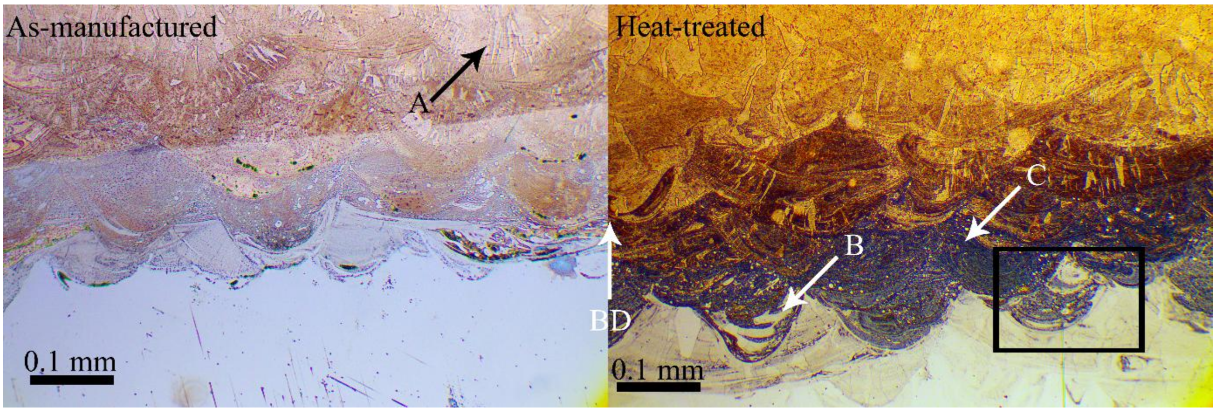

Figure 55 Microstructure of the bimetallic interface zone.

As Figure 55 shows, columnar crystals are visible on the CuCrZr side of the bimetallic interface zone of IN718 and CuCrZr shown by the arrow marked with "A". "BD" represents the building direction. Mixing of IN718 and CuCrZr is observed. The bimetallic interface zone consists of IN718 and CuCrZr rich areas. IN718 has formed localized islands within CuCrZr, indicated by the arrow marked with "B". A CuCrZr rich area is shown by the arrow marked with "C". The black rectangle shows the area presented closer in Figure 56.

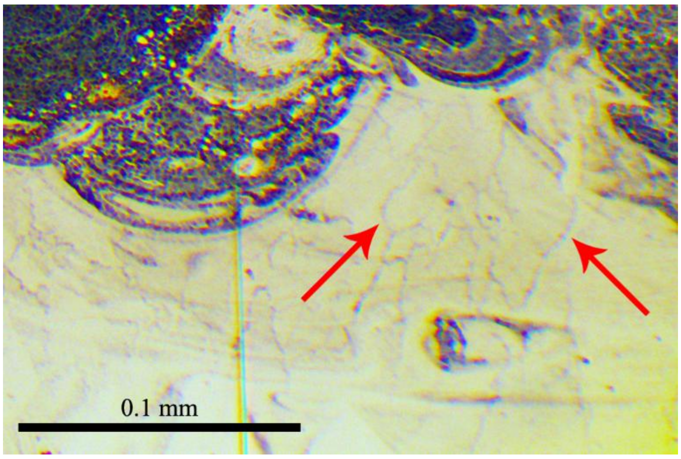

Figure 56 Microcracking in IN718.

As Figure 56 shows, microcracking is visible in IN718 near the interface zone indicated by the arrows. This was suspected to have been caused by the differences in thermal gradients of the two materials. In addition, the high thermal energy needed to melt CuCrZr can cause additional thermal stresses in the IN718 near the first CuCrZr layers. A study by Meyer et al., 2025 reported similar observations regarding cracking near the interface zone using a similar material combination of 316L stainless steel and CuCrZr.

The results from microstructural analysis show the compatibility between IN718 and CuCrZr in a bimetallic material combination. However, the heat treatment process, which was based on the heat treatment of IN718, was not the optimal process for the bimetallic material combination of IN718 and CuCrZr and lead to the increase in the number of defects.

9.5 Geometrical accuracy

Geometrical accuracy measurements were conducted to an as-manufactured and a heat-treated sample. Figure 57 shows the measurement scanning tracks used in the as-manufactured sample.

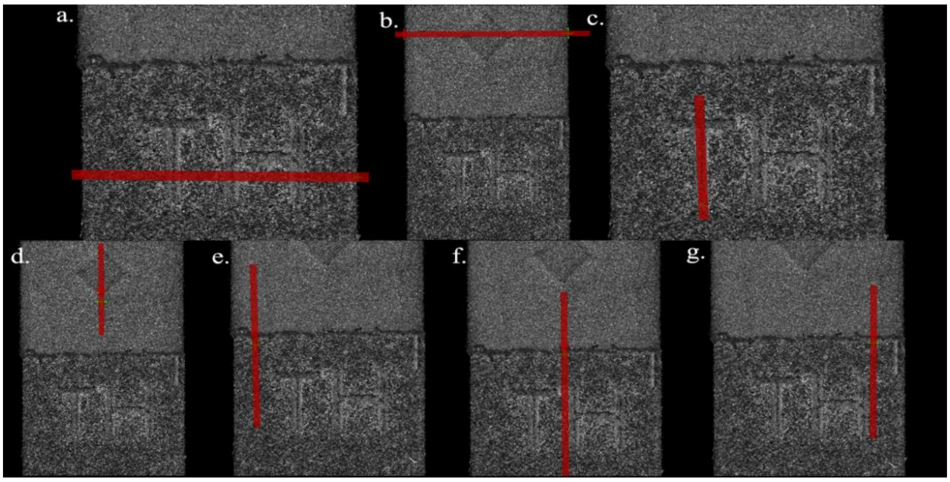

Figure 57 Geometrical accuracy measurement tracks on the as-manufactured sample.

As Figure 57 shows, seven different measurements were taken from the sample, marked with red lines. Figure 57a shows the scan track for measuring the width of the IN718 part of the sample. Figure 57b shows the track for measuring the width of the CuCrZr part. Figure 57c shows the track for scanning the height of the sample identification text located in the IN718 part. Figure 57d shows the track for scanning the square located in the CuCrZr part. Figure 57e-g show the scanning tracks for measuring the offset between the IN718 and CuCrZr parts on the left and right sides, and the centre of the sample.

Figure 58 shows the geometrical surface data from the scan tracks shown in Figure 57.

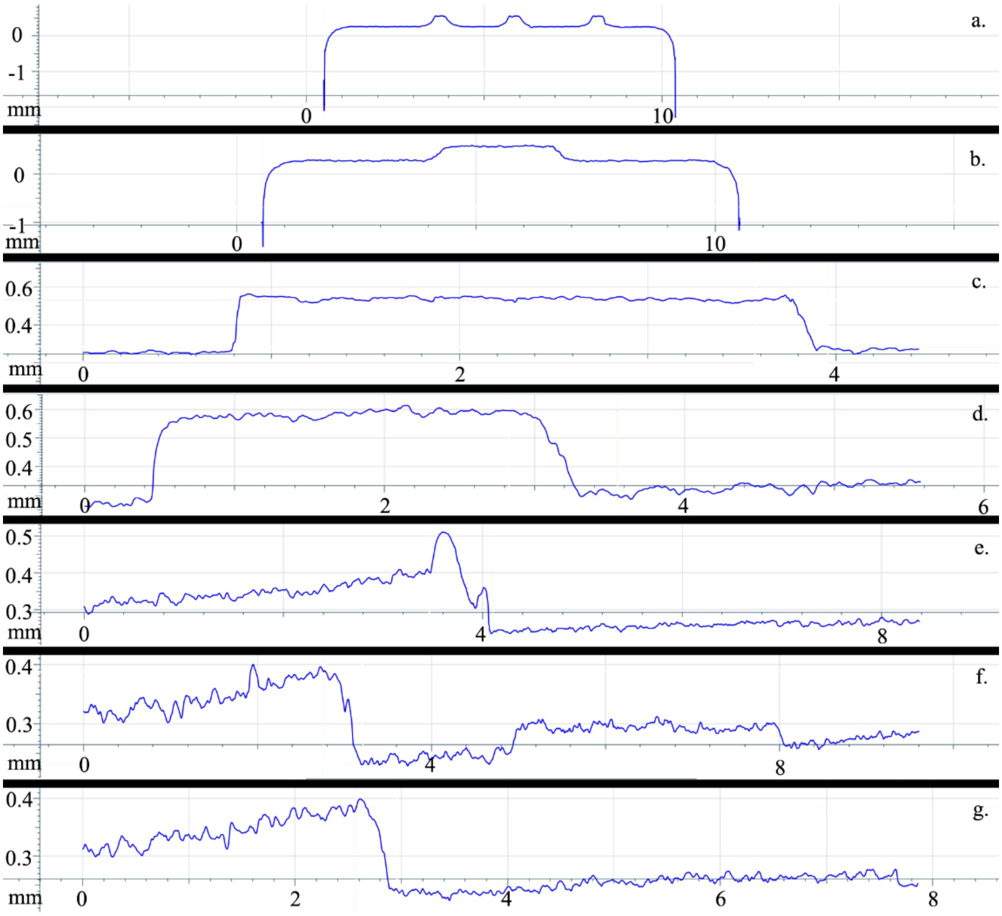

Figure 58 Surface scan curves from the as-manufactured sample.

The scanned widths of the IN718 and CuCrZr parts are represented by Figure 58a and Figure 58b, respectively. Figure 58c and Figure 58d show the sample ID text extrusion and square extrusion heights, respectively. Figure 58e-g show the left, centre, and right offset measurements between the IN718 and CuCrZr parts, respectively.

Figure 59 shows the measurement scanning tracks for the heat-treated sample.

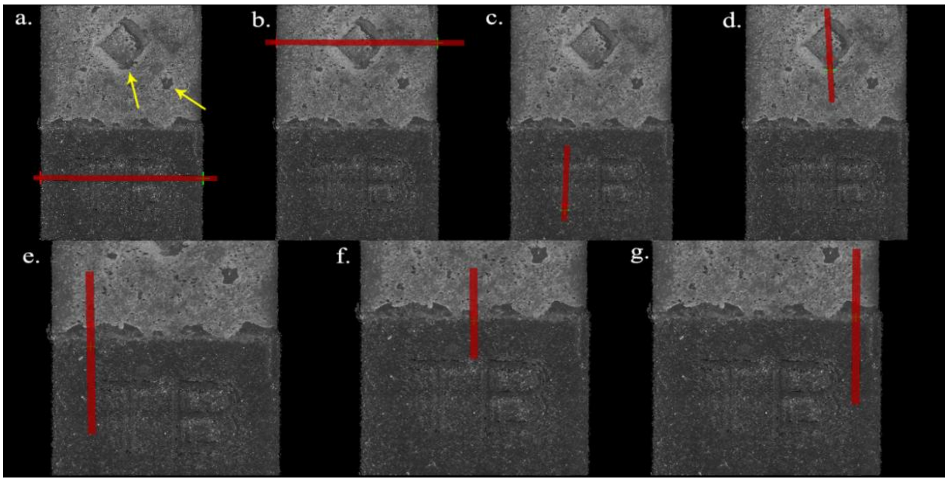

Figure 59 Geometrical accuracy measurement tracks on the heat-treated sample.

As Figure 59 shows, seven different measurements were taken from the sample, marked with red lines. Figure 59a shows the scan track for measuring the width of the IN718 part of the sample. Figure 59b shows the track for measuring the width of the CuCrZr part. Figure 59c shows the track for scanning the height of the sample identification text located in the IN718 part. Figure 59d shows the track for scanning the square located in the CuCrZr part. Figure 59e-g show the scanning tracks for measuring the offset between the IN718 and CuCrZr parts on the left and right sides, and the centre of the sample. The yellow arrows seen in Figure 59a show oxidation scale left on the CuCrZr part by the heat treatment process. The scale was avoided in the measurements as was noted to affect the measurement accuracy.

Figure 60 shows the geometrical surface data from the scan tracks shown in Figure 59.

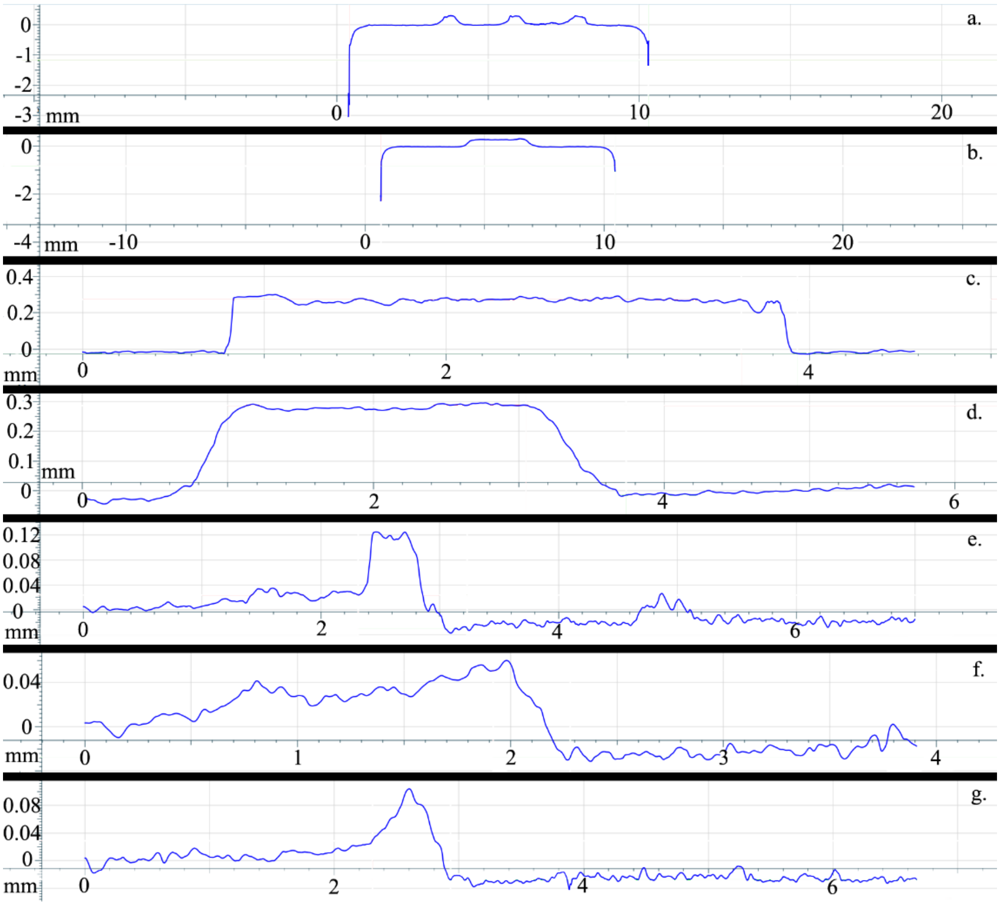

Figure 60 Surface scan curves from the heat-treated sample.

The scanned widths of the IN718 and CuCrZr parts are represented by Figure 60a and Figure 60b, respectively. Figure 60c and Figure 60d show the sample ID text extrusion and square extrusion heights, respectively. Figure 60e-g show the left, centre, and right offset measurements between the IN718 and CuCrZr parts, respectively.

Figure 61 shows the widths of the IN718 and CuCrZr parts measured from the as-manufactured and heat-treated samples.

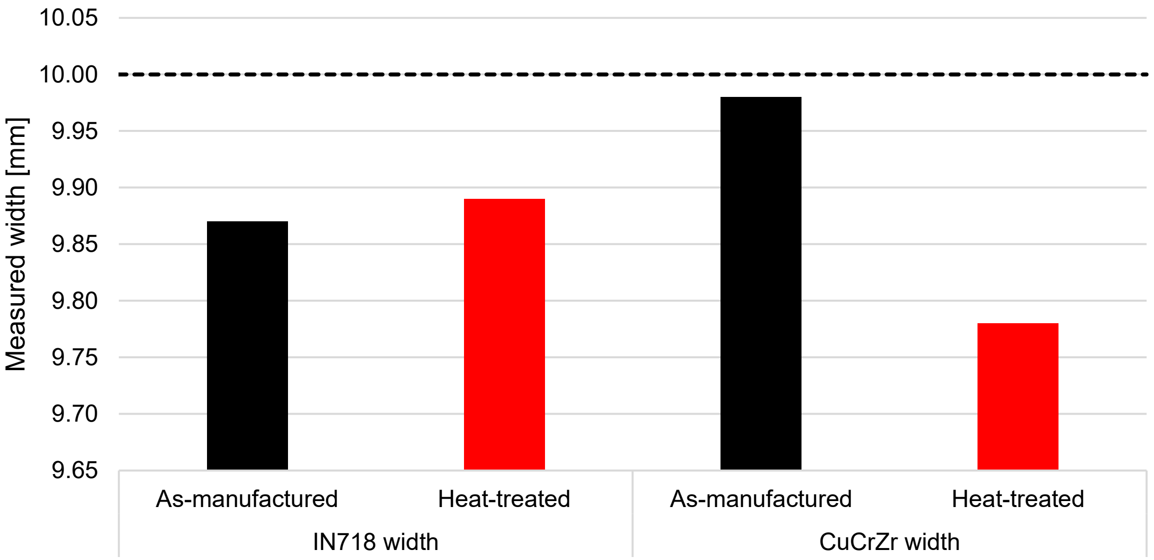

Figure 61 Measured widths of the IN718 and CuCrZr parts.

The dashed horizontal line in black in Figure 61 represents the part width set to 10.0 mm in the CAD file. As Figure 61 shows, the measured width of the as-manufactured IN718 part was 9.87 mm. The width of the heat-treated part was 9.89 mm. The difference to the CAD file value of 10.0 mm was -0.13 mm in the as-manufactured part and -0.11 mm in the heat-treated part. The width of the as-manufactured CuCrZr part was 9.94 mm whereas the width of the heat-treated part was 9.78 mm. The difference to the CAD file value was -0.06 mm in the as-manufactured part and -0.22 mm in the heat-treated part.

Figure 62 shows the heights of the sample ID and square extrusions measured from the as-manufactured and heat-treated samples.

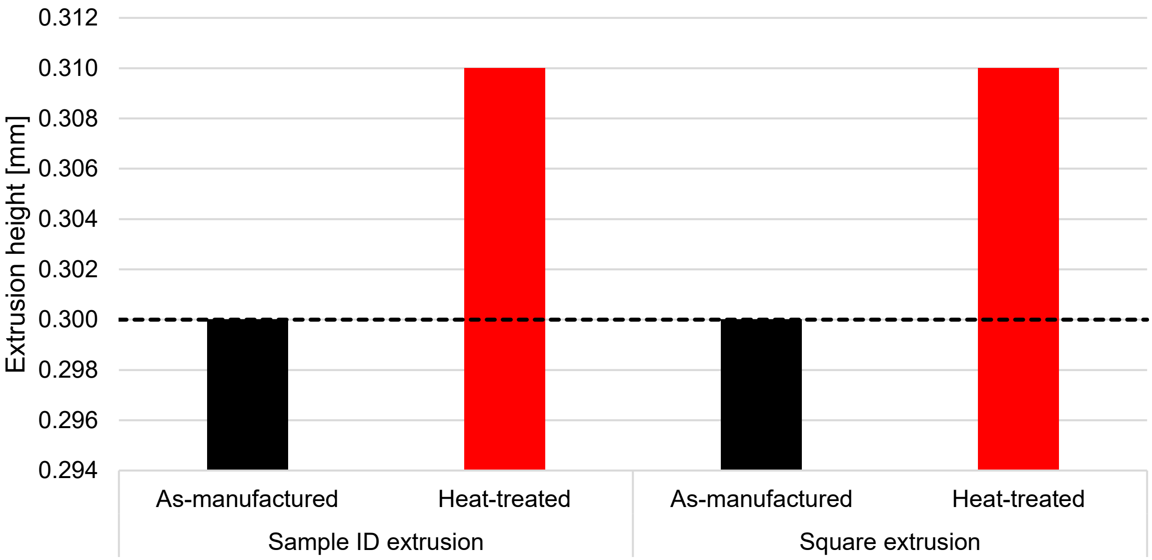

Figure 62 Measured heights of the sample ID and square extrusions.

The dashed horizontal line in black in Figure 62 represents the extrusion height set to 0.30 mm in the CAD file. As Figure 62 shows, the measured height of the as-manufactured sample ID extrusion in the IN718 part was 0.30 mm. The height on the heat-treated part was 0.31 mm. The difference to the CAD file value of 0.30 mm in the heat-treated part was 0.01 mm. The height of the square extrusion in the as-manufactured CuCrZr part was 0.30 mm whereas the width of the heat-treated part was 0.31 mm. The difference to the CAD file value of 0.30 mm in the heat-treated part was 0.01 mm.

Figure 63 shows the offsets between of the IN718 and CuCrZr parts measured from the as-manufactured and heat-treated samples.

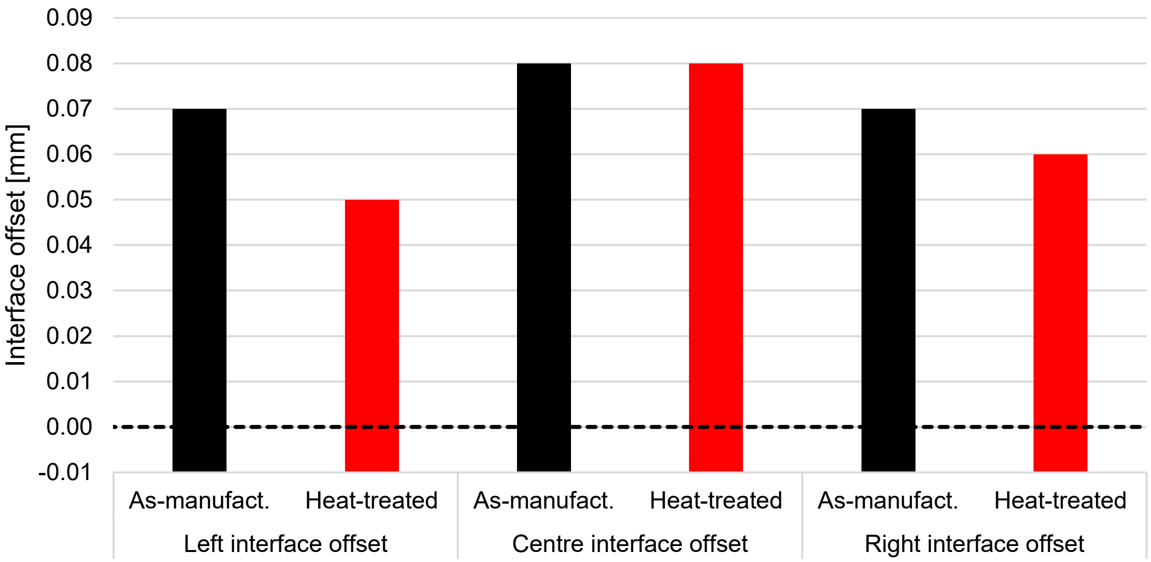

Figure 63 Measured offsets between the IN718 and CuCrZr parts.

The dashed horizontal line in black in Figure 63 represents the offset between the IN718 and CuCrZr parts set to 0.00 mm in the CAD file. The surface in the IN718 part was considered as the zero plane in these measurements. As Figure 63 shows, the measured offsets on the left sides of the interfaces were 0.07 and 0.05 mm in the as-manufactured and heat-treated samples, respectively. On the centre parts of the interfaces the values were 0.08 mm for both as-manufactured and heat-treated samples. On the right sides of the interfaces these values were 0.07 and 0.06 mm in the as-manufactured and heat-treated samples, respectively.

It should be noted that the used Bruker Alicona InfiniteFocus G6 optical 3D measuring instrument can measure the surface to a 0.001 mm accuracy. However, each measuring point is selected manually. The samples have a rough surface due to the nature of the PBF-LB/M process. This roughness appears as noise in the measurement data shown in Figure 64.

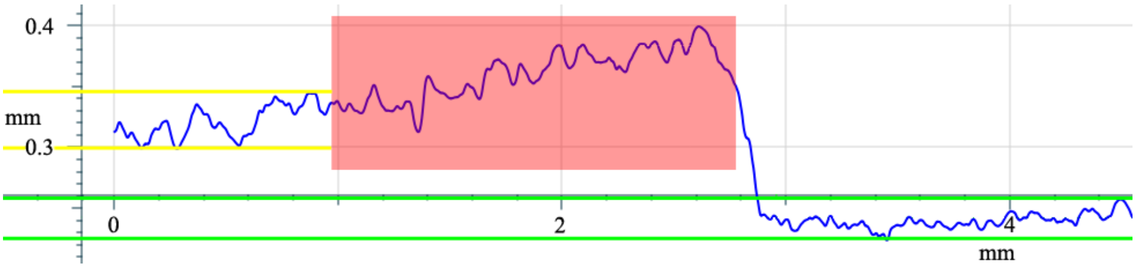

Figure 64 Noise in geometrical accuracy measurement data.

As Figure 64 shows, the noise on the IN718 side is around 0.04 mm, marked with green lines. The noise on the CuCrZr side is around 0.05 mm, marked with yellow lines. A deformity was observed on the CuCrZr side right after the interface, marked with the red rectangle. This deformity was ignored in the interface offset measurements, as the CuCrZr surface levels after around 1.7 mm from the interface. A visual location for the surface zero plane was selected in each measurement to ignore the noise. The deformity was suspected to be caused by the differences in thermal conductivity between IN718 and CuCrZr. The thermal energy introduced by the laser beam could cause the melt pool to spread in the CuCrZr powder as IN718 does not conduct the thermal energy away as effectively. In both samples the width of the IN718 part was observed to be less than the value stated in the CAD file. This was suspected to be caused by shrinking of the material during the PBF-LB/M process. A decrease in the width of the CuCrZr part was observed after heat-treatment. This was suspected to be caused by the oxidation of the surface of the material during heat-treatment. The oxidised scale layer was removed from the CuCrZr part after heat-treatment. The increase in the height on sample ID and square extrusion parts was suspected to be caused by leftover scale present after heat treatment.

9.6 Thermal conductivity

Figure 65 shows the thermal conductivities of the as-manufactured and heat-treated IN718, CuCrZr, and the bimetallic material.

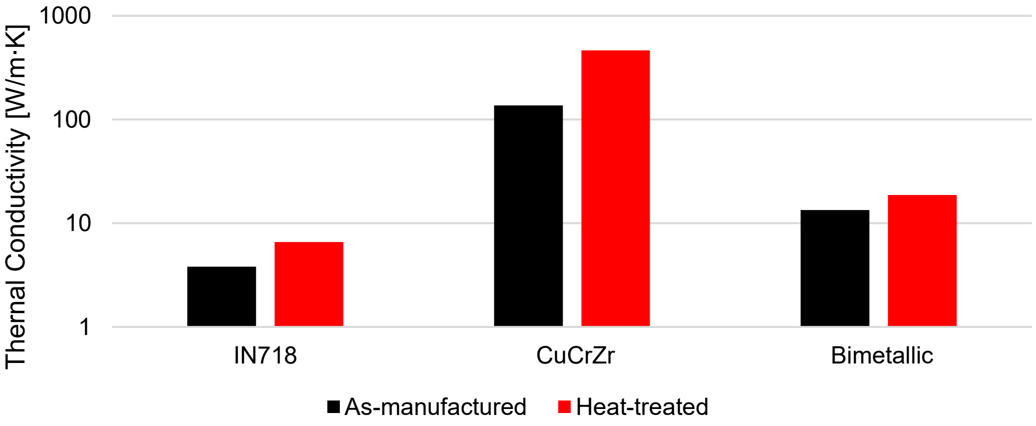

Figure 65 Thermal conductivities of IN718, CuCrZr, and the bimetallic material.

As Figure 65 shows, thermal conductivity increased in all materials after heat-treatment.

The thermal conductivity value of IN718 in the as-manufactured sample was 3.80 W/m·K. On the heat-treated sample the value was 6.59 W/m·K. This is an increase of 73.4 %.

The thermal conductivity of CuCrZr changed from 137 W/m·K in the as-manufactured sample to 464 W/m·K in the heat-treated sample. This is an increase of 238 %.

In the bimetallic material the value changed from 13.4 W/m·K to 18.7 W/m·K. This is an increase of 39.6 %.

The thermal conductivity values of IN718 are low compared to results found in literature. A study by Hakeem et al., 2021 reported thermal conductivity values to be around 10.0 W/m·K and Zhang et al., 2024 reported the value to be 12.3 W/m·K for as-manufactured material. Similarly, after heat treatment the values from the tested IN718 are below prementioned reported values. However, the test methods were different. Hakeem et al., 2021 used a modified transient plane source method for measurements and Zhang et al., 2024 used a laser beam flash method. The setup used in this this thesis is simple and may not give as accurate results compared to these methods.

The thermal conductivity value of the as-manufactured CuCrZr correspond to reported values in a study by Tang, Chen, Sun, Li, et al., 2022. The reported value for as-manufactured CuCrZr was around 125 W/m·K whereas the value for the as-manufactured material in this thesis was 137 W/m·K. Zhang et al., 2024 reported a value of 104 W/m·K. However, the thermal conductivity value of the heat treated material was higher. Tang, Chen, Sun, Li, et al., 2022 reported the highest value of around 350 W/m·K for solution annealed and age hardened material. The value after heat treatment in this thesis was 464 W/m·K. It should be noted that the heat treatments were different. In addition, the test methods were different. Tang, Chen, Sun, Li, et al., 2022 used an eddy-current conductivity meter to measure the electrical conductivity of the samples.

The thermal conductivity values of the bimetallic material were low compared to results found in literature. Zhang et al., 2024 reported a value of 31.9 W/m·K for the as-manufactured material and 75.0 W/m·K for the heat-treated material. The heat treatments and measurement methods were both different compared to this thesis.

The results acquired in this thesis show that heat treatment increases the thermal conductivity of both IN718 and CuCrZr and therefore increases the thermal conductivity of the bimetallic material combination.

9.7 Corrosion

Sample pieces from an as-manufactured sample and a heat-treated sample underwent open circuit potential (OCP) and Tafel extrapolation corrosion parameter tests.

9.7.1 Open circuit potential

Figure 66 shows the open circuit potential curves of both as-manufactured and heat-treated IN718.

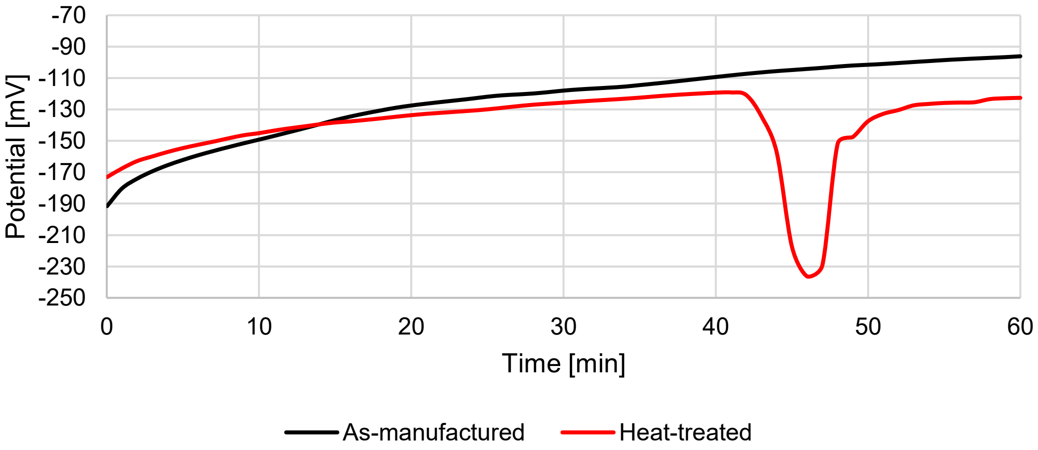

Figure 66 OCP curves of IN718.

As Figure 66 shows, the OCP value of the as-manufactured IN718 at the start of the test is -192 mV and after 60 minutes the value starts to converge at -96.7 mV. The OCP value of the heat-treated material at the start of the test is around -173 mV and after 60 minutes the value starts to converge at -123 mV. A noticeable decrease in the OCP value can be observed in the heat-treated material between 40 and 50 minutes. This was caused by an unknown error during the test. The OCP value was observed to begin stabilizing after the error. However, it was observed that a 60-minute test time may not be sufficient for IN718, as the curves have not completely levelled within this time frame.

Figure 67 shows the open circuit potential curves of both as-manufactured and heat-treated CuCrZr.

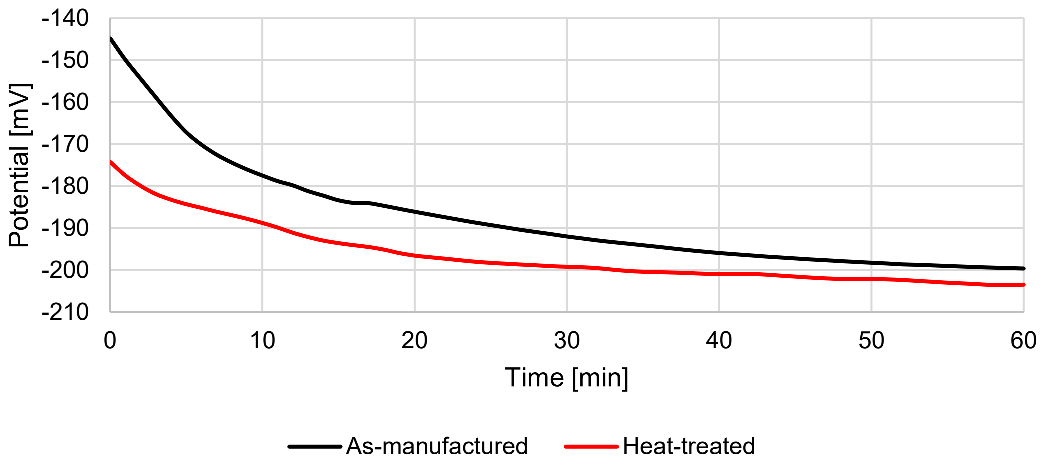

Figure 67 OCP curves of CuCrZr.

As Figure 67 shows, the OCP value of the as-manufactured CuCrZr at the start of the test is -145 mV and after 60 minutes the value converges at -199 mV. The OCP value of the heat-treated material at the start of the test is around -174 mV and after 60 minutes the value converges at -204 mV.

Figure 68 shows the open circuit potential curves of both as-manufactured and heat-treated bimetallic material.

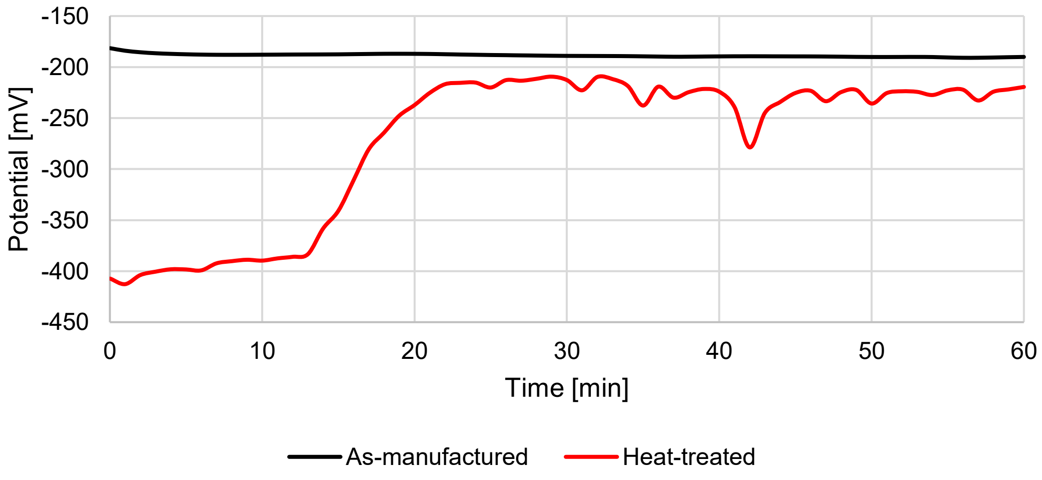

Figure 68 OCP curves of bimetallic material.

As Figure 68 shows, the OCP value of the as-manufactured bimetallic material at the start of the test is -181 mV and after 60 minutes the value converges at -190 mV. The OCP value of the heat-treated material at the start of the test is around -407 mV and after 60 minutes the value converges at -222 mV.

All the heat-treated materials showed a decrease in the OCP value compared to the as-manufactured material. A lower, more negative OCP value can indicate that a material is more prone to corrosion. (Lei et al., 2025) The corrosion resistance of IN718 is affected by, for example, the present phases in the material and the microstructure. (Valle et al., 2019) The corrosion resistance of CuCrZr can be affected by defects such as cracks and pores. (X. Li et al., 2024) Microcracks were observed in CuCrZr after the heat treatment process. Similarly, IN718 showed cracking near the interface zone after heat treatment.

The results acquired from the OCP measurements in this thesis suggest that heat treatment lowered the corrosion resistance of both IN718 and CuCrZr and the bimetallic combination of IN718 and CuCrZr. This is caused by the increase in the number of defects found in CuCrZr and IN718 near the interface zone. However, a longer time could give different results for IN718 as the OCP curves had not completely levelled within the used 60-minute timeframe.

9.7.2 Tafel extrapolation method

Figure 69 shows the Tafel extrapolation curves of both as-manufactured and heat-treated IN718.

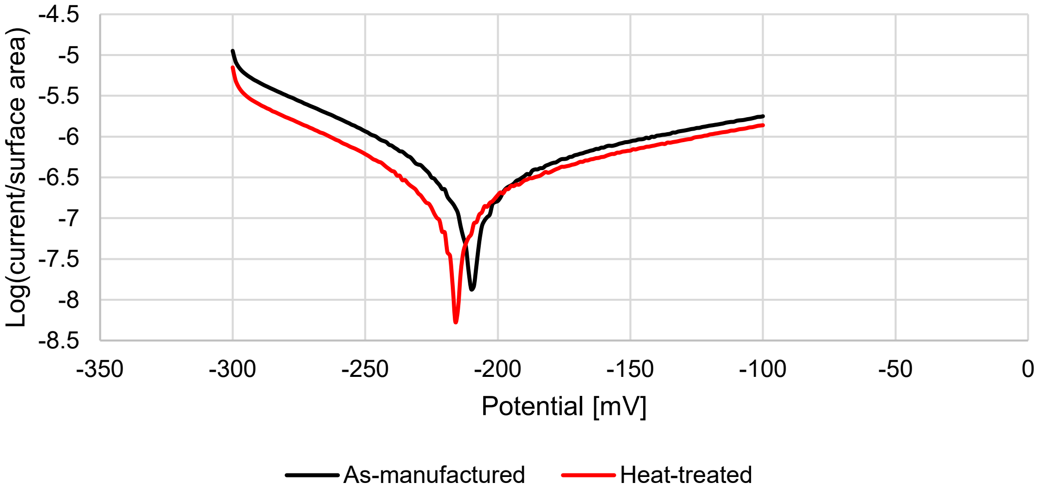

Figure 69 Tafel extrapolation curves of IN718.

As Figure 69 shows the E_{corr} value of the as-manufactured IN718 is higher than of the heat-treated material. The E_{corr} value of the as-manufactured IN718 was -210 mV. In the heat-treated material this value was -215 mV. Periyasamy & Srinivasan, 2025 reported values of -251 mV and -202 mV for as-manufactured and heat-treated materials, respectively.

The I_{corr} value in the as-manufactured material was 0.31 µA/cm^2. In the heat-treated material this value was 0.19 µA/cm^2. Periyasamy & Srinivasan, 2025 reported values of 0.34 µA/cm^2 and 0.13 µA/cm^2 for as-manufactured and heat-treated materials, respectively.

The corrosion rates were 2.56 µm/y and 1.57 µm/y for the as-manufactured and heat-treated materials, respectively. Periyasamy & Srinivasan, 2025 reported values of 3.28 µm/y and 1.24 µm/y for as-manufactured and heat-treated materials, respectively.

Figure 70 shows the Tafel extrapolation curves of both as-manufactured and heat-treated CuCrZr.

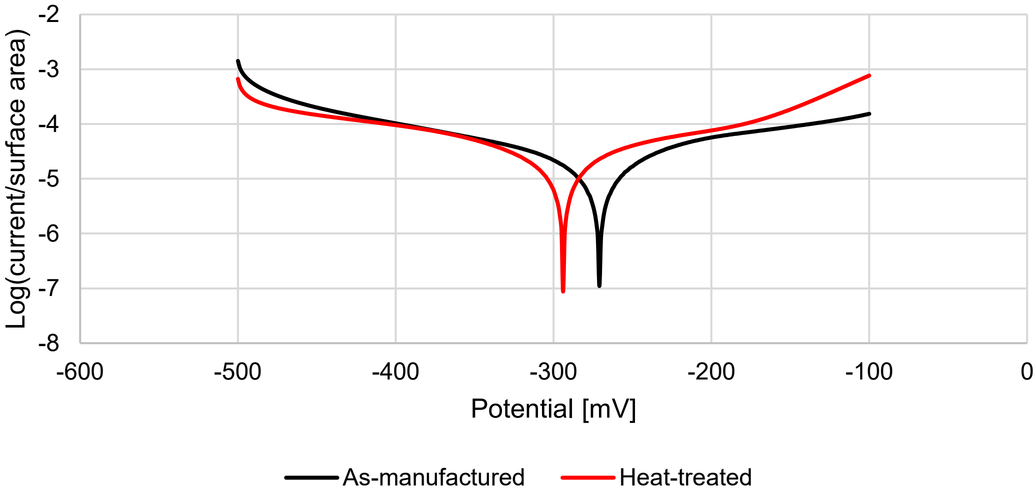

Figure 70 Tafel extrapolation curves of CuCrZr.

As Figure 70 shows the E_{corr} value of the as-manufactured CuCrZr is higher than of the heat-treated material. The E_{corr} value of the as-manufactured CuCrZr was -272 mV. In the heat-treated material this value was -293 mV. Dongfang et al., 2025 reported a value of -429 mV for as-manufactured material.

The I_{corr} value in the as-manufactured material was 21.7 µA/cm^2. In the heat-treated material this value was 26.3 µA/cm^2. Dongfang et al., 2025 reported a value of 23.3 µA/cm^2 for as-manufactured material.

The corrosion rates were 254 µm/y and 307 µm/y for the as-manufactured and heat-treated materials, respectively. The increase in the corrosion rate was suspected to have been caused by the microcracking of the material following heat treatment.

Figure 71 shows the Tafel extrapolation curves of both as-manufactured and heat-treated bimetallic material.

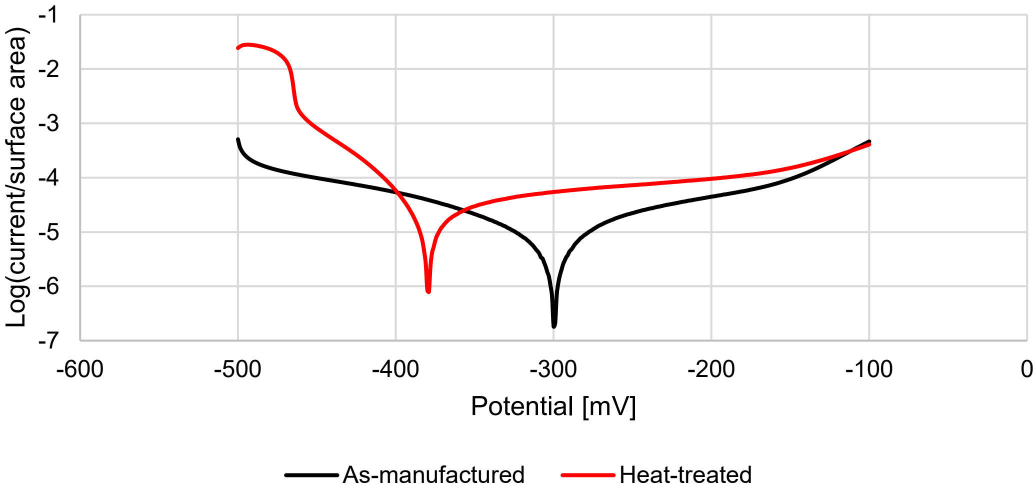

Figure 71 Tafel extrapolation curves of bimetallic material.

As Figure 71 shows the E_{corr} value of the as-manufactured bimetallic material is higher than of the heat-treated material. The E_{corr} value of the as-manufactured bimetallic material was -301 mV. In the heat-treated material this value was -379 mV. The I_{corr} value in the as-manufactured material was 13.8 µA/cm^2. In the heat-treated material this value was 29.9 µA/cm^2. The corrosion rates were 137 µm/y and 293 µm/y for the as-manufactured and heat-treated materials, respectively. The corrosion behaviour before and after heat treatment resembles the behaviour of CuCrZr. The increase in the corrosion rate was suspected to have been caused by the microcracks in CuCrZr and cracking observed in IN718 near the interface zone.

The results from the Tafel extrapolation tests show that the corrosion resistance of IN718 increased after heat-treatment. However, an increase in corrosion rates was observed in CuCrZr and bimetallic material after heat treatment caused by the increase in number of defects found in the materials.

9.8 Hardness

Hardness measurements were taken from an as-manufactured sample and four heat-treated samples. Samples for the analysis were selected based on their respective locations on the build plate during the manufacturing process. Figure 72 shows the hardness measurement results from the as-manufactured bimetallic sample of IN718 and CuCrZr.

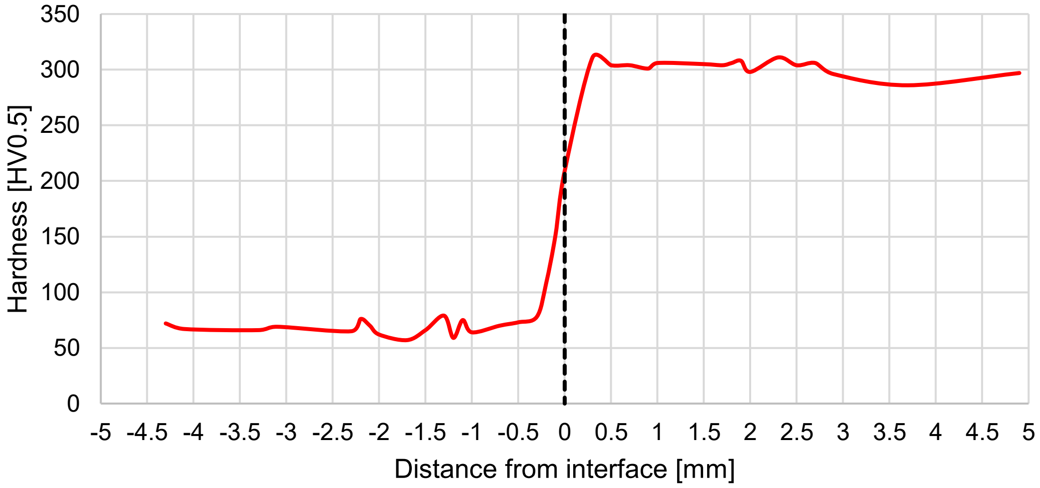

Figure 72 Measured hardness results of as-manufactured material sample.

As Figure 72 shows, measurements were taken from the CuCrZr zone moving over the interface zone to the IN718 zone from left to right. The interface is represented by the dashed vertical line at 0 mm.

The average hardness of the IN718 zone was 303 $HV_{0.5}$. The individual hardness values varied between 286 and 311 $HV_{0.5}$. The distances from the interface were 0.3 mm and 4.9 mm from the interface for the closest and furthest points, respectively.

The average hardness of the interface zone was 156 $HV_{0.5}$. The individual hardness values varied between 108 and 209 $HV_{0.5}$. The distances from the interface were -0.2 mm and 0.0 mm from the interface for the furthest and closest points, respectively.

The average hardness of the CuCrZr zone was 68.7 $HV_{0.5}$. The individual hardness values varied between 57.0 and 78.0 $HV_{0.5}$. The distances from the interface were -4.3 mm and -0.3 mm from the interface for the furthest and closest points, respectively.

Three measurement points were removed from the results as the points were observed to be located on pores or other defects resulting in incorrect hardness values.

Figure 73 shows the hardness measurement results from heat-treated samples.

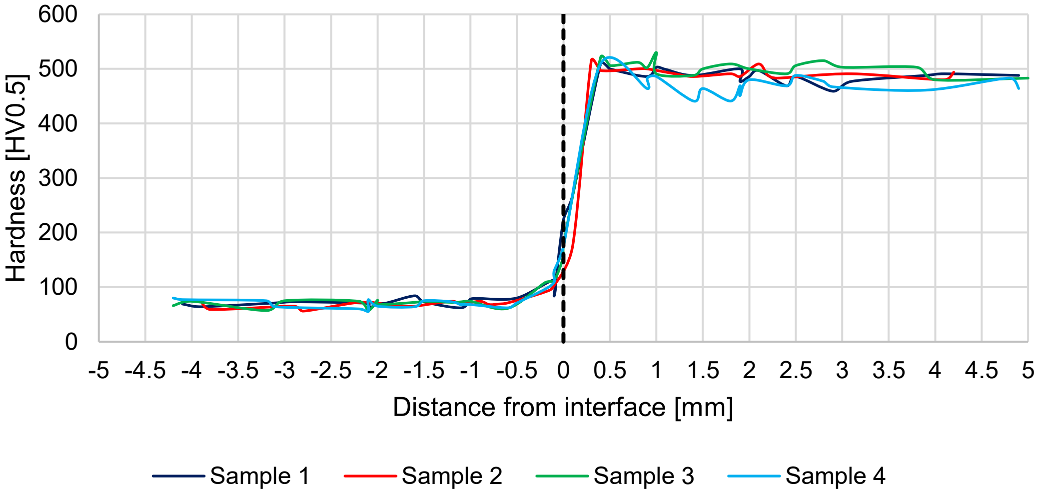

Figure 73 Measured hardness results of heat-treated material samples.

As Figure 73 shows, measurements were taken from the CuCrZr zone moving over the interface zone to the IN718 zone from left to right. The interface is represented by the dashed vertical line at 0 mm.

The average hardness of the IN718 zone was 488 $HV_{0.5}$ in sample 1. The individual hardness values varied between 459 and 509 $HV_{0.5}$. The distances from the interface were 0.4 mm and 4.9 mm from the interface for the closest and furthest points, respectively.

The average hardness of the interface zone was 173 $HV_{0.5}$ in sample 1. The individual hardness values varied between 86 and 269 $HV_{0.5}$. The distances from the interface were -0.1 mm and 0.1 mm from the interface for the furthest and closest points, respectively.

The average hardness of the CuCrZr zone was 71.7 $HV_{0.5}$ in sample 1. The individual hardness values varied between 61.0 and 84.0 $HV_{0.5}$. The distances from the interface were -4.1 mm and -0.5 mm from the interface for the furthest and closest points, respectively.

Four measurement points were removed from the results of sample 1 as the points were observed to be located on pores or other defects resulting in incorrect hardness values.

As Figure 73 shows, the average hardness of the IN718 zone was 494 $HV_{0.5}$ in sample 2. The individual hardness values varied between 480 and 515 $HV_{0.5}$. The distances from the interface were 0.3 mm and 4.2 mm from the interface for the closest and furthest points, respectively.

The average hardness of the interface zone was 123 $HV_{0.5}$ in sample 2. The individual hardness values varied between 91 and 176 $HV_{0.5}$. The distances from the interface were -0.2 mm and 0.1 mm from the interface for the furthest and closest points, respectively.

The average hardness of the CuCrZr zone was 67.7 $HV_{0.5}$ in sample 2. The individual hardness values varied between 56.0 and 74.0 $HV_{0.5}$. The distances from the interface were -3.9 mm and -0.6 mm from the interface for the furthest and closest points, respectively.

Eight measurement points were removed from the results of sample 2 as the points were observed to be located on pores or other defects resulting in incorrect hardness values.

As Figure 73 shows, the average hardness of the IN718 zone was 502 $HV_{0.5}$ in sample 3. The individual hardness values varied between 480 and 530 $HV_{0.5}$. The distances from the interface were 0.4 mm and 5.0 mm from the interface for the closest and furthest points, respectively.

The average hardness of the interface zone was 138 $HV_{0.5}$ in sample 3. The individual hardness values varied between 108 and 177 $HV_{0.5}$. The distances from the interface were -0.2 mm and 0.0 mm from the interface for the furthest and closest points, respectively.

The average hardness of the CuCrZr zone was 69.5 $HV_{0.5}$ in sample 3. The individual hardness values varied between 57.0 and 76.0 $HV_{0.5}$. The distances from the interface were -4.1 mm and -0.6 mm from the interface for the furthest and closest points, respectively.

Six measurement points were removed from the results of sample 3 as the points were observed to be located on pores or other defects resulting in incorrect hardness values.

As Figure 73 shows, the average hardness of the IN718 zone was 470 $HV_{0.5}$ in sample 4. The individual hardness values varied between 441 and 509 $HV_{0.5}$. The distances from the interface were 0.4 mm and 4.9 mm from the interface for the closest and furthest points, respectively.

The average hardness of the interface zone was 138 $HV_{0.5}$ in sample 4. The individual hardness values varied between 96 and 175 $HV_{0.5}$. The distances from the interface were -0.2 mm and 0.0 mm from the interface for the furthest and closest points, respectively.

The average hardness of the CuCrZr zone was 68.8 $HV_{0.5}$ in sample 4. The individual hardness values varied between 55.0 and 80.0 $HV_{0.5}$. The distances from the interface were -4.2 mm and -0.5 mm from the interface for the furthest and closest points, respectively.

Three measurement points were removed from the results of sample 4 as the points were observed to be located on pores or other defects resulting in incorrect hardness values.

The measured average hardness value of 303 $HV_{0.5}$ in the as-manufactured IN718 was observed to be similar to the values by Zhang et al., 2024. The average hardness value measured by Zhang et al., 2024 was 330 ± 5 $HV_{0.5}$. In addition, Naskar et al., 2024a reported a hardness value of 324 ± 4 $HV_{0.5}$ for as-manufactured IN718.

Heat treatment increased the average hardness value of IN718 to 488 $HV_{0.5}$ between the four samples. Similarly, Naskar et al., 2024a reported values ranging from 476 ± 4 to 504 ± 3 $HV_{0.5}$ between different heat treatments.

The measured average hardness value of 156 $HV_{0.5}$ in the as-manufactured interface zone was observed to be similar to the values by Zhang et al., 2024. The average hardness value measured by Zhang et al., 2024 was 169 ± 4 $HV_{0.5}$. Zhang et al., 2024 did not study the effects of heat treatments on the hardness values of the interface zone.

After heat treatment, the measured average hardness value of the interface zones was 141 $HV_{0.5}$ between the four samples. The decrease in the hardness was suspected to be caused by the increased number of measurement points between the as-manufactured and heat-treated samples. The as-manufactured interface zone in the sample contained three measurement points, whereas the number of measurement points in the heat-treated samples was 15. In addition, the interface zone contains IN718 and CuCrZr rich areas, shown in Figure 74.

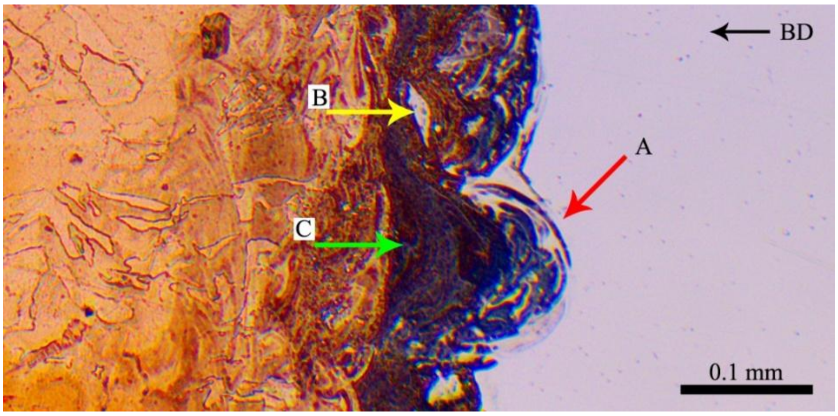

Figure 74 Micrograph of interface zone.

As Figure 74 shows, the circular melt pool tracks left by the laser beam from the PBF-LB/M process are visible, indicated by the arrow marked with “A”. The arrow marked with “B” indicates a IN718 rich area surrounded by CuCrZr. The arrow marked with “C” indicates a CuCrZr rich area. The hardness values can be different, as some of the hardness measurement points have located on either of the rich areas. “BD” shows the build direction.

The measured average hardness value of 68.7 $HV_{0.5}$ in the as-manufactured CuCrZr was observed to be lower compared to the values reported in a study by Zhang et al., 2024. The average hardness value measured by Zhang et al., 2024 was 86 ± 4 $HV_{0.5}$. In addition, hardness values measured by Wallis & Buchmayr, 2019 was reported to be 80 ± 2 $HV_{1.0}$. In addition, Tang, Chen, Sun, Li, et al., 2022 reported a hardness value of 130 ± 15 $HV_{0.2}$ for the as-manufactured material.

The effects of the used heat treatment plan were noticed to cause miniscule changes in the hardness of CuCrZr as the average value changed from 68.7 $HV_{0.5}$ to 69.4 $HV_{0.5}$ between the four heat-treated material samples. This was suspected to have caused by the IN718 based heat treatment plan not being optimal for CuCrZr if increasing hardness is desired. The long heat treatment times lead to over-aging which causes the hardness to decrease. Similar results were reported by Wallis & Buchmayr, 2019. Wallis & Buchmayr, 2019 reported values of 126 ± 2 $HV_{1.0}$ with solution annealing and age hardening, and 185 ± 2 $HV_{1.0}$ with direct age hardening. Similarly, Tang, Chen, Sun, Li, et al., 2022 reported hardness values ranging from 103 ± 10 to 183 ± 20 $HV_{0.2}$ with different solution annealing and age hardening, and direct age hardening plans.

It should be noted that different process parameters, used machines and powders can affect the material properties. No significant differences in hardness were observed based on the sample location on the PBF-LB/M machine build plate.

The results acquired in this thesis show that heat treatment increases the hardness of IN718 and the bimetallic interface zone of IN718 and CuCrZr. However, the hardness of CuCrZr did not increase significantly due to the over-aging caused by the selected heat treatment process. The heat treatment process was based on the process used for IN718.

10 Conclusions

The aim and purpose of this thesis was to study the process for manufacturing bimetallic material consisting of IN718 and CuCrZr using PBF-LB/M and to analyse different material characteristics and properties.

The PBF-LB/M manufacturing process of a bimetallic material combination of IN718 and CuCrZr was successfully presented by the experimental part of this thesis. Successful manufacturing of both materials was achieved through process optimisation.

The material characterisations and testing conducted in this thesis show promise for the defect-free manufacturing of the bimetallic material. Both materials showed material specific properties regarding the manufacturing process and material characteristics corresponding to literature. The interface zone showed mixing of the two materials suggesting material bonding. In addition, the interface zone properties were a combination between the properties of IN718 and CuCrZr.

The microstructures of the materials were analysed using optical microscopy. In addition, geometrical accuracy, hardness, and corrosion parameters of the manufactured materials were analysed with dedicated equipment. Corrosion parameters were determined using OCP and Tafel extrapolation methods. The thermal conductivities of the materials were calculated from electrical resistance values measured from the materials using a resistance meter.

Microstructural analysis revealed some defects, including porosity and microcracking, localised in the different material regions. However, no major defects were present although further manufacturing process optimisation is needed to minimise or remove the remaining imperfections.

The heat-treatment used in this thesis was based on a heat-treatment process designed for IN718. This was observed to increase the thermal conductivity and hardness values of IN718 and improve the corrosion resistance, as was suggested by literature. However, the differences in IN718 and CuCrZr thermal gradients were noted to cause microcracking in IN718 near the interface zone caused by the rapid heating rate during the heat treatment process. The hardness and thermal conductivity of the bimetallic material in the interface zone was observed to increase with heat treatment. However, the corrosion resistance was noted to decrease after heat treatment, mirroring the behaviour of CuCrZr. Heat-treatment increased the thermal conductivity of CuCrZr but led to formation of microcracks in the material. In addition, the corrosion resistance of CuCrZr was observed to decrease, suspected to be caused by the formation of microcracks. The hardness of CuCrZr was observed to only slightly increase by the heat treatment due to over aging. Further development of the heat treatment process is needed to prevent the formation of microcracks in the materials. In addition, a compromise between the heat treatment process of IN718 and CuCrZr needs to be studied if an increase in the hardness of CuCrZr is desirable.

The PBF-LB/M equipment used during the manufacturing phase of this thesis featured a single material feedstock system, forcing to stop the manufacturing sequence between the different materials which can lead to residual stresses in the previously manufactured material. Multi-material feeding systems can rectify this limitation allowing for changing on feedstock materials during the process, in addition to enabling the manufacturing of more complex structures. On the other hand, keeping the manufacturing processes separate for each material allows for recycling the unused powder feedstock material to a certain extent, whereas multi-material feeding systems can lead to mixing of the separate powders, rendering recycling hard or impossible.

Further tensile tests are required to properly test the bonding between the two materials as this was not mechanically analysed within the scope of this thesis. In addition, a more in-depth analysis of the interface zone and mixing of the two materials would require the use of equipment such as a scanning electron microscope which was not plausible within the thesis timeframe.

References

Balbaa, M., Mekhiel, S., Elbestawi, M., & McIsaac, J. (2020). On selective laser melting of Inconel 718: Densification, surface roughness, and residual stresses. *Materials & Design*, *193*, 108818. https://doi.org/10.1016/j.matdes.2020.108818

Chechik, L., & Todd, I. (2023). Inconel 718 two ways: Powder bed fusion vs. directed energy deposition. *Additive Manufacturing Letters*, *6*, 100145. https://doi.org/10.1016/j.addlet.2023.100145

Choi, J.-P., Shin, G.-H., Yang, S., Yang, D.-Y., Lee, J.-S., Brochu, M., & Yu, J.-H. (2017). Densification and microstructural investigation of Inconel 718 parts fabricated by selective laser melting. *Powder Technology*, *310*, 60–66. https://doi.org/10.1016/j.powtec.2017.01.030

Cortis, D., Mancini, E., Orlandi, D., Pilone, D., & Sasso, M. (2023). Additively manufactured CuCrZr alloy: Improvement of mechanical properties by heat treatment. *Procedia Structural Integrity*, *47*, 908–914. https://doi.org/10.1016/j.prostr.2023.07.021

Deng, D. (2018). *Additively manufactured Inconel 718: Microstructures and Mechanical properties*. Department of Management and Engineering, Linköping University.

Diao, Z., Yang, F., Wang, R., Zhang, Y., Chen, L., Xiong, T., Yang, W., & Rong, M. (2023). Effect of heat treatment on the microstructure and properties of CuCrZr alloy manufactured by wire arc additive manufacturing. *Journal of Alloys and Compounds*, *967*, 171786. https://doi.org/10.1016/j.jallcom.2023.171786

Dongfang, K., Fan, H., Sui, S., Li, H., Liu, H., Li, Y., & Liu, P. (2025). Effect of Laser Powder Bed Fusion Process Parameters on the Microstructures, Mechanical Properties, and Conductivity of CuCrZr Alloy. *Journal of Materials Engineering and Performance*, *34*(13), 13304–13317. https://doi.org/10.1007/s11665-024-10026-3

EOS CopperAlloy CuCrZr | Metal Powder | EOS Store. (n.d.). Retrieved March 19, 2025, from https://store.eos.info/products/eos-copperalloy-cucrzr

Gruber, K., Stopyra, W., Kobiela, K., Madejski, B., Malicki, M., & Kurzynowski, T. (2022). Mechanical properties of Inconel 718 additively manufactured by laser powder bed fusion after industrial high-temperature heat treatment. *Journal of Manufacturing Processes*, *73*, 642–659. https://doi.org/10.1016/j.jmapro.2021.11.053

Guo, P., Martin, A., Zhai, C., Li, Z., Lu, X., Yu, J., Lin, X., Odnevall, I., Gibbons, M., & Schubert, A. (2025). Effect of current density on electrochemical machining process of laser powder bed fusion manufactured Inconel 718. *Journal of Materials Processing Technology*, *337*, 118748. https://doi.org/10.1016/j.jmatprotec.2025.118748

Hakeem, A. S., Patel, F., Minhas, N., Malkawi, A., Aleid, Z., Ehsan, M. A., Sharrofna, H., & Al Ghanim, A. (2021). Comparative evaluation of thermal and mechanical properties of nickel alloy 718 prepared using selective laser melting, spark plasma sintering, and casting methods. *Journal of Materials Research and Technology*, *12*, 870–881. https://doi.org/10.1016/j.jmrt.2021.03.043

Hosseini, E., & Popovich, V. A. (2019). A review of mechanical properties of additively manufactured Inconel 718. *Additive Manufacturing*, *30*, 100877. https://doi.org/10.1016/j.addma.2019.100877

Hu, Z., Du, Z., Yang, Z., Yu, L., & Ma, Z. (2022). Preparation of Cu–Cr–Zr alloy by selective laser melting: Role of scanning parameters on densification, microstructure and mechanical properties. *Materials Science and Engineering: A*, *836*, 142740. https://doi.org/10.1016/j.msea.2022.142740

Jeyaprakash, N., Alnaser, I. A., Cheng, Y., & Karuppasamy, S. S. (2024). Effect of heat treatment on microstructure and mechanical characteristics of laser powder bed fusion

(LPBF) produced CuCrZr alloy. *Tribology International*, *197*, 109826. https://doi.org/10.1016/j.triboint.2024.109826

Lei, Z., Mull, K., & Dimitrov, N. (2025). Comparative Analysis of the Corrosion Behavior of Plain and Nanoporous Copper. *Electrochem*, *6*(1), 1. https://doi.org/10.3390/electrochem6010001

Li, X., Saario, T., Ikäläinen, T., & Que, Z. (2024). Corrosion behavior of additively manufactured M300-CuCr1Zr by multi-material laser-based powder bed fusion. *Electrochimica Acta*, *507*, 145199. https://doi.org/10.1016/j.electacta.2024.145199

Li, Z., Chen, Y., Zhang, S., Liu, B., Kuai, Z., Huo, W., Yang, H., Wei, M., & Bai, P. (2023). Microstructure and properties in CuCrZr alloy fabricated by selective laser melting with different heat treatment. *Results in Physics*, *54*, 107125. https://doi.org/10.1016/j.rinp.2023.107125

Li, Z., Kuai, Z., Liu, B., Chen, Y., Li, H., Wang, Y., Huo, W., Wei, M., Yang, H., & Bai, P. (2023). Selective laser melting of 316L–CuCrZr bimetallic structure via IN718 transition layer. *Journal of Materials Research and Technology*, *25*, 3819–3834. https://doi.org/10.1016/j.jmrt.2023.06.196

Lowrie, W., & Fichtner, A. (2020). *Fundamentals of Geophysics* (3rd ed.). Cambridge University Press. https://doi.org/10.1017/9781108685917

Mao, S., Yang, B., Liu, G., Liu, G., & Zhang, Z. (2023). Temperature distribution and residual stress evolution at the interface of CuCrZr/316 L multi-material by laser powder bed fusion. *Optics & Laser Technology*, *163*, 109355. https://doi.org/10.1016/j.optlastec.2023.109355

Meyer, I., Messmann, C. O., Ehlers, T., & Lachmayer, R. (2025). Additive manufacturing of multi-material parts – Effect of heat treatment on thermal, electrical, and mechanical part properties of 316L/CuCrZr. *Materials & Design*, *252*, 113783. https://doi.org/10.1016/j.matdes.2025.113783

Naskar, S., Suryakumar, S., & Panigrahi, B. B. (2024a). Heat treatments effects on Wear performance of Laser based Powder Bed Fusion fabricated Inconel 718 alloy. *Wear*, *556–557*, 205526. https://doi.org/10.1016/j.wear.2024.205526

Naskar, S., Suryakumar, S., & Panigrahi, B. B. (2024b). Heat treatments-induced wear resistance of Inconel 718 superalloy fabricated via Laser based Powder Bed Fusion. *Materials Today Communications*, *41*, 110789. https://doi.org/10.1016/j.mtcomm.2024.110789

Naskar, S., Suryakumar, S., & Panigrahi, B. B. (2025). Post-processing of Inconel 718 superalloy by Laser-based Powder Bed Fusion: Microstructures and properties evaluation. *Materials Science and Engineering: A*, *921*, 147601. https://doi.org/10.1016/j.msea.2024.147601

Nazir, A., Gokcekaya, O., Md Masum Billah, K., Ertugrul, O., Jiang, J., Sun, J., & Hussain, S. (2023). Multi-material additive manufacturing: A systematic review of design, properties, applications, challenges, and 3D printing of materials and cellular metamaterials. *Materials & Design*, *226*, 111661. https://doi.org/10.1016/j.matdes.2023.111661

Nikon SLM Solutions Nickel-based Alloys. (n.d.). Retrieved March 19, 2025, from https://nikon-slm-solutions.com/materials/nickel/

Ostergaard, H. E., Pribe, J. D., Hasib, M. T., Siegmund, T., & Kruzic, J. J. (2025). Crack growth in laser powder bed fusion fabricated alloy 718 at 650 °C under static and cyclic loading. *International Journal of Fatigue*, *193*, 108810. https://doi.org/10.1016/j.ijfatigue.2025.108810

Pavithran, N. R., Harichandran, R., & Kumar, D. V. (2023). Effect of Yttria-stabilized zirconia coating on the corrosion and thermal behaviour of additive manufactured Inconel 718 alloy. *Journal of Alloys and Compounds*, *968*, 171877. https://doi.org/10.1016/j.jallcom.2023.171877

Pei, E., Bernard, A., Gu, D., Klahn, C., Monzón, M., Petersen, M., & Sun, T. (Eds.). (2023). *Springer handbook of additive manufacturing*. Springer.

Periyasamy, M., & Srinivasan, N. (2025). Effect of heat treatment on the microstructures, mechanical, and corrosion performance of laser powder bed fusion manufactured Inconel 718 alloy. *Materials Letters*, *401*, 139243. https://doi.org/10.1016/j.matlet.2025.139243

Salvan, C., Briottet, L., Baffie, T., Guetaz, L., & Flament, C. (2021). CuCrZr alloy produced by laser powder bed fusion: Microstructure, nanoscale strengthening mechanisms, electrical and mechanical properties. *Materials Science and Engineering: A*, *826*, 141915. https://doi.org/10.1016/j.msea.2021.141915

Sarkeeva, E. A., Sitdikov, V. D., Raab, G. I., Wei, W., & Alexandrov, I. V. (2018). The effect of Cr and Zr content on the microstructure and properties of the Cu-Cr-Zr system alloy. *IOP Conference Series: Materials Science and Engineering*, *447*, 012065. https://doi.org/10.1088/1757-899X/447/1/012065

Sheikholeslami, M., & Ganji, D. D. (2018). Effect of Marangoni Convection on Nanofluid Treatment. In *Applications of Semi Analytical Methods for Nanofluid Flow and Heat Transfer* (pp. 491–510). Elsevier. https://doi.org/10.1016/B978-0-12-813675-1.00010-2

Sun, F., Liu, P., Chen, X., Zhou, H., Guan, P., & Zhu, B. (2020). Mechanical Properties of High-Strength Cu–Cr–Zr Alloy Fabricated by Selective Laser Melting. *Materials*, *13*(21), 5028. https://doi.org/10.3390/ma13215028

Tang, X., Chen, X., Sun, F., Li, L., Liu, P., Zhou, H., Fu, S., & Li, A. (2022). A study on the mechanical and electrical properties of high-strength CuCrZr alloy fabricated using laser powder bed fusion. *Journal of Alloys and Compounds*, *924*, 166627. https://doi.org/10.1016/j.jallcom.2022.166627

Tang, X., Chen, X., Sun, F., Liu, P., Zhou, H., & Fu, S. (2022). The current state of CuCrZr and CuCrNb alloys manufactured by additive manufacturing: A review. *Materials & Design*, *224*, 111419. https://doi.org/10.1016/j.matdes.2022.111419

Valle, L. C. M., Santana, A. I. C., Rezende, M. C., Dille, J., Mattos, O. R., & De Almeida, L. H. (2019). The influence of heat treatments on the corrosion behaviour of nickel-based alloy 718. *Journal of Alloys and Compounds*, *809*, 151781. https://doi.org/10.1016/j.jallcom.2019.151781

Volpato, G. M., Tetzlaff, U., & Fredel, M. C. (2022). A comprehensive literature review on laser powder bed fusion of Inconel superalloys. *Additive Manufacturing*, *55*, 102871. https://doi.org/10.1016/j.addma.2022.102871

Wallis, C., & Buchmayr, B. (2019). Effect of heat treatments on microstructure and properties of CuCrZr produced by laser-powder bed fusion. *Materials Science and Engineering: A*, *744*, 215–223. https://doi.org/10.1016/j.msea.2018.12.017

Wang, Q., Shao, H., Zhang, X., Wang, K., Liu, S., Yang, C., & Wang, W. (2023). Study of thermal behavior and microstructure formation mechanism of CuCrZr alloy melted by laser powder bed fusion. *Materials Characterization*, *198*, 112721. https://doi.org/10.1016/j.matchar.2023.112721

Xu, L., Zhang, Y., Zhao, L., Ren, W., & Han, Y. (2024). Performance Improvement for the CuCrZr Alloy Produced by Laser Powder Bed Fusion Using the Remelting Process. *Materials*, *17*(3), 624. https://doi.org/10.3390/ma17030624

Yadroitsev, I., Yadroitsava, I., Plessis, A. du, & MacDonald, E. (Eds.). (2021). *Fundamentals of laser powder bed fusion of metals*. Elsevier.

Zhang, L., Dong, P., Zeng, Y., Yao, H., & Chen, J. (2024). Additive manufacturing of Inconel 718/CuCrZr multi-metallic materials fabricated by laser powder bed fusion. *Additive Manufacturing*, *92*, 104377. https://doi.org/10.1016/j.addma.2024.104377

Zhao, B., Hutt, K., Yamaguchi, H., & Pan, S. (2025). Surface corrosion in laser powder bed fusion-fabricated Inconel 718 with magnetic field-assisted post-processing. *Journal of Manufacturing Processes*, *143*, 277–292. https://doi.org/10.1016/j.jmapro.2025.04.001

Zhong, Q., Wei, K., Lu, Z., Yue, X., Ouyang, T., & Zeng, X. (2023). High power laser powder bed fusion of Inconel 718 alloy: Effect of laser focus shift on formability, microstructure and mechanical properties. *Journal of Materials Processing Technology*, *311*, 117824. https://doi.org/10.1016/j.jmatprotec.2022.117824

Appendices

Appendix 1 PBF-LB and multi-material AM

Laser-based powder bed fusion is a commonly used additive manufacturing technique. As the name suggests, a laser beam is used as the energy source, and the feedstock material is in powder form. The feedstock materials can be for example metals or polymers. PBF-LB machines feature a build chamber in which the manufacturing takes place. (Pei et al., 2023) The atmosphere inside the sealed chamber is regulated by replacing air with an inert gas. (Zhang et al., 2024) In addition, some machines offer for example the controlling temperatures inside the build chamber. Temperature controls can include the chamber ambient, build plate, and powder feedstock temperatures. (Pei et al., 2023)

PBF-LB machines use files from computer-aided design software as component data input. The components or assembly geometries in the files are sliced into layers that are each built separately, one after another. The build process consists of a layer of powder being spread on the build plate using a spreader, or recoater. The laser beam is used to melt and fuse the selected areas of the powder once a powder layer is spread. These areas correspond with the sliced component geometries. As this process is repeated, the melted areas of the powder layers fuse to the preceding layer, resulting in a three-dimensional component. (Pei et al., 2023; Tang, Chen, Sun, Liu, et al., 2022)

Different process parameters in PBF-LB include for example laser power, velocity of laser beam i.e. scanning speed, hatch distance i.e. overlapping of previously scanned areas. (Pei et al., 2023) A parameter for comparing and evaluating the PBF-LB process is the volumetric energy density (VED). (Xu et al., 2024) The formula for calculating the VED [J/mm^3] is presented in Equation (5) below (Xu et al., 2024).

$$VED = \frac{P}{vht} \tag{5}$$

In Equation (5), P is laser power, v is laser beam scanning speed, h is hatch distance, and t is layer thickness.

Another parameter used for process evaluation is the linear energy density (LED). The formula for calculating the LED [J/m] is presented in Equation (6) below. (Hosseini & Popovich, 2019)

$$LED = \frac{P}{v} \tag{6}$$

In Equation (6), P is laser power, and v is scanning speed of laser beam.

The PBF-LB process is sensitive to changes in process parameters. The manufactured components may have defects even with optimised process parameters. These defects include, for example, pores and cracks, residual stresses, and deviations in geometrical accuracy. (Deng, 2018)

PBF-LB can produce ready-to-use parts but in many cases, some form of post-processing is required to modify material properties to suit the application of the manufactured component. Post-processing steps can include heat treatment, surface finishing etc. (Pei et al., 2023)

Multi-material additive manufacturing allows the manufacturing of components with changing materials in the component structure. Traditional manufacturing methods of multi-material parts include welding, vapor deposition, spraying etc. (Mao et al., 2023; Zhang et al., 2024) These traditional methods are limited by design complexity, and other challenges including weak bonding between the different materials, solidification cracking caused by material property differences etc. (Zhang et al., 2024)

In multi-material additive manufacturing the differences in material properties must be considered. Differences in mechanical properties and material characteristics under changing temperatures affect compatibility of the materials. (Zhang et al., 2024)

Multi-material combinations offer multiple advantages compared to single materials. Different regions of the part can be tuned to have desirable properties by using multiple materials in a component structure. (Mao et al., 2023) These properties include, for example, thermal conductivity and hardness. (Nazir et al., 2023)

Multi-material AM faces multiple limitations and concerns even though the technique offers improvements compared to traditional multi-material manufacturing methods. The materials used must have matching physical properties to manufacture a defect-free transition zone between the materials. Defects, e.g. cracks and deformation, can be caused by differences in residual stresses caused by different thermal expansion and heat conduction rates between the materials. (Mao et al., 2023) Multi-material AM is also limited by the AM equipment. Many AM machines only have a single material feeding system. (Nazir et al., 2023) In order to use machines with a single material feeding system to manufacture multi-material components, the manufacturing process must be stopped at the wanted material interface zone, the feedstock material replaced, and the machine thoroughly cleaned to avoid contamination of the new feedstock material. The interrupted manufacturing process can affect the material transition zone and lengthen the manufacturing time significantly.

Appendix 2 Sample coordinates on build plate

The same coordinates were used for sample placement on the build plate for both sets of samples manufactured in the experimental part of this thesis. Figure 75 shows the sample placement from above, or Z-direction.

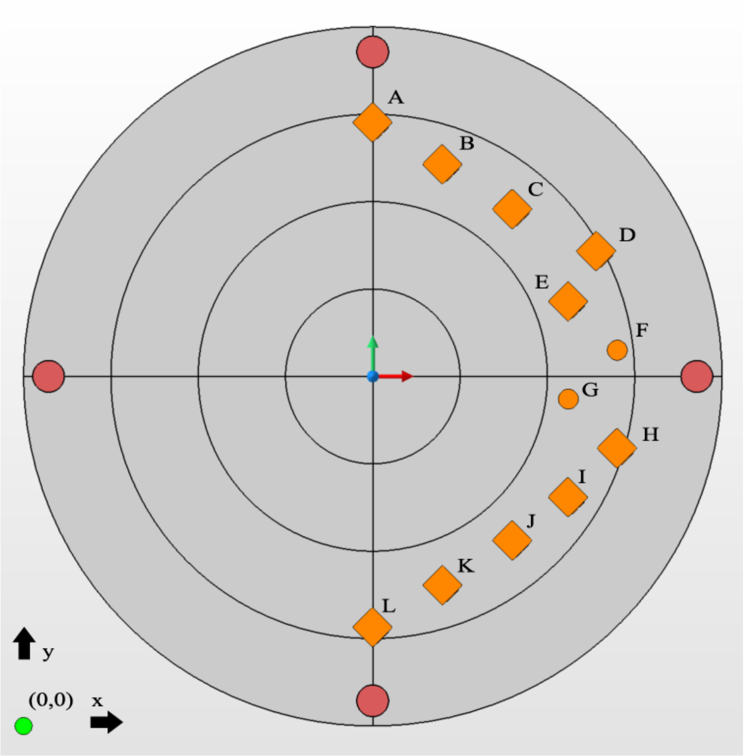

Figure 75 Sample arrangement on build plate.

As Figure 75 shows, the twelve orange silhouettes represent the respective parts. The four red circles on the edges of the round build plate represent the build plate securing bolts. The X and Y directions are marked with arrows on the bottom left corner of the figure. The green circle represents the (0,0) point, where the sample geometries are located when imported to the software. The sample specific coordinates are shown in Table 27.

Table 27 Sample coordinates for build plate placement.

Sample identification	X-coordinate	Y-coordinate
A	125.000	215.875
B	150.000	200.875

C	175.000	184.875
D	205.000	169.375
E	195.000	151.875
F	212.500	134.875
G	195.000	116.875
H	212.500	99.375
I	195.000	81.875
J	175.000	66.375
K	150.000	50.375
L	125.000	35.375

As Table 27 shows, each sample was placed on the build plate using individual coordinates. The coordinates were the same for both manufactured batches of samples.

Appendix 3 Thermal conductivity calculations

Electrical resistance was measured from sample pieces cut from an as-manufactured sample and a heat-treated sample. The measured resistance values were used to calculate the electrical resistivity of the sample pieces. The electrical resistivity was used to determine the thermal conductivity of the materials. The cut sample pieces are shown in Figure 76.

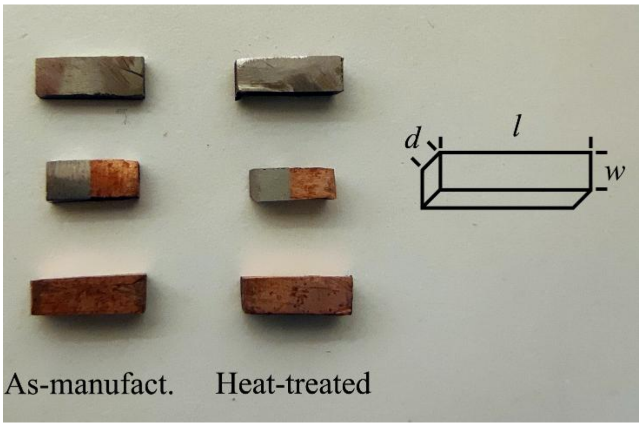

Figure 76 Cut sample pieces for electrical resistance measurements.

As Figure 76 shows, the samples were cut into three pieces consisting of IN718, the bimetallic material, and CuCrZr. In Figure 76, *w* shows the piece width, *d* the depth, and *l* the length.

The specifications of the sample pieces are shown in Table 28.

Table 28 Specifications of sample pieces used for electrical resistance tests.

Sample	Material	Piece width *w* [mm]	Piece depth *d* [mm]	Piece length *l* [mm]	Cross-sect. area *A* [mm^2]
As-manuf.	IN718	2.70	3.60	9.90	9.72
As-manuf.	CuCrZr	3.10	3.30	10.0	10.23
As-manuf.	Bimetallic	2.20	3.60	8.30 (3.80/4.50)	7.92
Heat-treated	IN718	2.80	3.30	9.80	9.24
Heat-treated	CuCrZr	3.20	3.40	9.90	10.88
Heat-treated	Bimetallic	2.90	3.00	7.40 (3.20/4.20)	8.70

As Table 28 shows, six different sample pieces were prepared for electrical resistance measurements. The width of the pieces varied from 2.20 to 3.20 mm. The depth varied from 3.00 to 3.60 mm. The length of the pieces varied from 7.40 to 10.0 mm. The length of the IN718 zone was 3.80 mm and length of CuCrZr zone was 4.50 mm in the as-manufactured bimetallic sample piece. The length of the IN718 zone was 3.20 mm and the length of the CuCrZr zone was 4.20 mm in the heat-treated bimetallic piece. The variations in the sample piece dimensions were caused by the manual cutting of the samples. The measurements were taken with a vernier calliper.

The cross-sectional area *A* of each sample piece was calculated by multiplying the piece width *w* with the piece depth *d*.

Electrical resistance measurement results for the IN718 pieces are shown in Table 29.

Table 29 Electrical resistance measurement results for IN718 sample pieces.

Sample	As-manufactured		Heat-treated	
Measur. No.	*R* [mΩ]	*D* [mm]	*R* [mΩ]	*D* [mm]
1	1.83	9.30	1.07	8.90
2	1.78	9.30	1.03	9.10
3	1.82	9.30	1.04	8.70
4	1.78	9.30	1.01	8.70
5	1.83	9.60	1.04	8.90

As Table 29 shows, each sample piece underwent five measurements with replacing the alligator clamps on each end of the sample piece. The contact point distance *D* between the alligator clamp contact points on the sample pieces was measured each time. The resistance *R* of the IN718 piece cut from sample as-manufactured varied between 1.78 and 1.83 mΩ. The contact point distance *D* between the alligator clamp contact points varied between 9.30 and 9.60 mm. The resistance *R* of the piece cut from the heat-treated sample varied between 1.01 and 1.07 mΩ. The contact point distance *D* between the alligator clamp contact points varied between 8.70 and 9.10 mm.

Electrical resistance measurement results for the CuCrZr pieces are shown in Table 30.

Table 30 Electrical resistance measurement results for CuCrZr sample pieces.

Sample	As-manufactured		Heat-treated	
Measur. No.	*R* [μΩ]	*D* [mm]	*R* [μΩ]	*D* [mm]
1	43.8	8.30	12.1	8.50
2	43.9	8.60	12.2	8.50
3	43.6	8.40	12.1	8.60
4	44.2	8.90	12.2	8.60
5	45.1	9.00	12.0	8.70

As Table 30 shows, each sample piece underwent five measurements with replacing the alligator clamps on each end of the sample piece. The contact point distance *D* between the alligator clamp contact points on the sample pieces was measured each time. The resistance *R* of the CuCrZr piece cut from the as-manufactured sample varied between 43.6 and 45.1 μΩ. The contact point distance *D* between the alligator clamp contact points varied between 8.30 and 9.00 mm. The resistance *R* of the piece cut from the heat-treated sample varied between 12.0 and 12.2 μΩ. The contact point distance *D* between the alligator clamp contact points varied between 8.50 and 8.70 mm.

Electrical resistance measurement results for the bimetallic pieces are shown in Table 31.

Table 31 Electrical resistance measurement results for bimetallic sample pieces.

Sample	As-manufactured		Heat-treated	
Measur. No.	*R* [μΩ]	*D* [mm]	*R* [μΩ]	*D* [mm]
1	510	7.70	297	7.10
2	540	7.70	317	7.10
3	520	7.70	316	7.00
4	512	7.70	301	6.80
5	497	7.50	276	6.30

As Table 31 shows, each sample piece underwent five measurements with replacing the alligator clamps on each end of the sample piece. The contact point distance *D* between the alligator clamp contact points on the sample pieces was measured each time. The resistance *R* of the bimetallic piece cut from the as-manufactured sample varied between 497 and 540 µΩ. The contact point distance *D* between the alligator clamp contact points varied between 7.50 and 7.70 mm. The resistance *R* of the piece cut from the heat-treated sample varied between 276 and 317 µΩ. The contact point distance *D* between the alligator clamp contact points varied between 6.30 and 7.10 mm.

The alligator clamp contact point distance *D* measurements were taken with a vernier calliper.

The formula for calculating the electrical resistivity ρ is shown in Equation (7) below. (Lowrie & Fichtner, 2020)

$$\rho = R\frac{A}{l} \tag{7}$$

In Equation (7), ρ is electrical resistivity, *R* is the sample piece resistance, *A* is the cross-sectional area of the sample piece, and *l* is the length of the sample piece. The length *l* is substituted with the contact point distance *D*, as the resistance values were measured using leads with alligator clamps and the entire length of the sample pieces was not utilized. The modified formula is represented in Equation (8) below.

$$\rho = R\frac{A}{D} \tag{8}$$

An example for calculating the electrical resistivity using an electrical resistance measurement of the as-manufactured IN718 sample piece using Equation (8) is shown below.

$$\rho = R\frac{A}{D} = 1.83 \cdot 10^{-3}\,\Omega * \frac{9.72 \cdot 10^{-6}\ m}{9.30 \cdot 10^{-3}\ m} \approx 191 \cdot 10^{-8}\Omega \cdot m$$

The calculated electrical resistivity *R* values of the sample pieces are shown in Table 32. The shown values are the averages calculated using the five separate resistance measurements.

Table 32 Electrical resistivity values of sample pieces.

Sample	As-manufactured			Heat-treated		
Material	IN718	CuCrZr	Bimetallic	IN718	CuCrZr	Bimetallic

Resistivity [Ω·m]	$188\cdot10^{-8}$	$5.23\cdot10^{-8}$	$53.3\cdot10^{-8}$	$108\cdot10^{-8}$	$1.54\cdot10^{-8}$	$38.2\cdot10^{-8}$

As Table 32 shows, heat-treatment decreased the resistivity ρ of IN718 from $188\cdot10^{-8}$ to $108\cdot10^{-8}$ Ω·m. This is a decrease of 42.6 %. The resistivity of CuCrZr decreased from $5.23\cdot10^{-8}$ to $1.54\cdot10^{-8}$ Ω·m. This is a decrease of 70.6 %. The resistivity of the bimetallic material decreased from $53.3\cdot10^{-8}$ to $38.2\cdot10^{-8}$ Ω·m. This is a decrease of 28.3 %.

The thermal conductivity can be calculated from the electrical resistivity using Equation (9) below.

$$\lambda = \frac{LT}{\rho} \tag{9}$$

In Equation (9), λ is thermal conductivity, L is the Lorenz number, T is temperature, and ρ is electrical resistivity. The Lorenz number is a constant value of $2.41 \cdot 10^{-8}$ Ω·WK^{-2}. (Tang, Chen, Sun, Li, et al., 2022) An example for calculating the thermal conductivity of the as-manufactured IN718 sample piece using Equation (9) is shown below.

$$\lambda = \frac{LT}{\rho} = \frac{2.41\cdot10^{-8}\ \Omega\cdot WK^{-2} * 296.15\ K}{1.88\cdot10^{-6}\ \Omega\cdot m} \approx 3.80\ W \cdot mK$$